Coherence effects in three- and four-level laser-cooled rubidium systems

Thesis

Coherence Effects in Three- and Four-Level Laser-Cooled Rubidium Systems

Sebastián R. de Echaniz

A thesis submitted in partial fulfilment of the requirements for the degree of Doctor of Philosophy.

Department of Physics and Astronomy
The Open University

24th September 2002

DATE OF SUBMISSION: 4 JULY 2002
DATE OF AWARD: 7 OCTOBER 2002

To my wife Minerva

Abstract

This thesis presents developmental work on the existing magneto-optical trap (MOT) system and novel studies of coherence effects.

The developmental work was carried out on the experimental apparatus used previously in this laboratory in order to perform experiments to study coherence effects in three- and four-level rubidium systems in the MOT. This developmental work includes the upgrading and installation of new laser systems, the improvement of the MOT, the installation of data acquisition hardware and software, and the commissioning of a new "second generation" MOT.

As part of our studies of coherence effects, we present a wide-ranging theoretical and experimental study of non-adiabatic transient phenomena in a Λ system which exhibits electromagnetically induced transparency when a strong coupling field is rapidly switched on or off using a Pockels cell. The theoretical treatment uses a Laplace transform approach as well as standard numerical methods to solve the time-dependent density matrix equation. The results show clear Rabi oscillations and transient gain without population inversion of a weak probe in parameter regions not previously

studied, and provide insight into the transition dynamics between bare states and dressed states.

Experimental studies of a doubly driven V system are also reported, together with a theoretical dressed-state analysis of such systems. The expected three-peak spectrum is explored for various coupling field strengths and detunings.

In all this work we have found good agreement between the theory and the experimental spectra once light shifts and uncoupled absorption in the rubidium system are taken into account.

Acknowledgements

First, I would like to thank my supervisor Dr Alan V. Durrant and my post-doctoral colleague Dr Andrew D. Greentree for their help and guidance during my PhD studentship. I have learnt very much from them and they have supported me at all times.

I would also like to thank the collaborators to this project, Dr Jon P. Marangos (Imperial College, London), Dr Daniel M. Segal (Imperial College, London) and Dr John A. Vaccaro (University of Hertfordshire), for their valuable discussions and contributions to my work. Dr Jon Marangos was also the person who presented me to this project and introduced me to Dr Alan Durrant, and I am very grateful for that.

Finally, I would like to thank The Open University Department of Physics and Astronomy for the financial support of my studentship and Dr. T. B. Smith (Open University) for useful discussions. I also thank Roger Bence, Fraser Robertson, and Robert Seaton (The Open University) and Shahid Hanif (Imperial College, London) for technical assistance.

Contents

List of Figures

List of Tables

Chapter 1

Introduction

The work presented in this thesis is part of an EPSRC funded project originally entitled "Giant Kerr Non-Linearities in Laser-Cooled Rubidium". This project was carried out in collaboration with our partners at Imperial College of Science, Technology and Medicine at the University of London, and the University of Hertfordshire. The project arose in response to a theoretical work by Imamoğlu *et al.* [1] that suggested that a cloud of rubidium atoms held in a magneto-optical trap (MOT) located within an optical cavity could form the basis of a "single-photon turnstile" device. The key to the scheme was the coherent preparation of the atomic medium and the exploitation of electromagnetically induced transparency (EIT). EIT occurs when a resonant coupling field coherently prepares an atomic sample to allow dissipation-free propagation of a weak probe field accompanied by strong dispersion.

Later studies [2] showed that the breakdown of the procedure in the high-dispersion limit leads to prohibitive restrictions on the parameter space where photon

blockade could be observed in a multi-atom system. It was however suggested [3] that these restrictions could be overcome by working with a cavity containing a single atom.

Our response was to undertake a theoretical study of the problem to see what could still be achieved experimentally within the context of a cloud of atoms in an MOT and whether the prospects for photon blockade were as bleak as the new theoretical work seemed to suggest. This theoretical work led to the first project publication "Prospects for photon blockade in four-level systems in the N configuration with more than one atom" [4]. In this paper we showed that, although demonstrating photon blockade with a cloud of cold atoms in an MOT would indeed seem to be impossible, it is not strictly necessary to use a *single* atom in a cavity. We showed that for the correct parameters photon blockade should be possible for one-, two- and three-atom systems, which may be realisable using an atomic beam or fountain. This work is outlined in Chapter 2 of this thesis.

In the meantime there has been a great deal of activity in the field of coherent control of prepared atomic systems. Of particular interest is the work on ultra-slow light propagation in these systems [5,6] which has appeared since the beginning of the Author's PhD studies.

1.1 Background to this work

Given the changes in the predictions of what might feasibly be achieved in our system, we decided to concentrate our experimental efforts on understanding some of the fundamental coherence effects in three- and four-level systems. Following earlier work in this laboratory on EIT, especially the preliminary experiments on the transient EIT effects following a fast switch-on of the coupling field [7,8], we decided to

undertake the first comprehensive theoretical and experimental study of EIT transients over a wide parameter range. This is the topic of Chapter 5 of this thesis.

Our other main interest was in coherently driven four-level systems, especially the giant third-order susceptibility that has applications to self- and cross-phase modulation, optical switches [9,10] and single-photon turnstile devices [1-4]. Chapter 6 of this thesis presents a theoretical and experimental study of a rubidium N system, from the point of view of a doubly-driven V system probed to a fourth level.

The background to these two areas are further discussed below.

1.1.1 Transient EIT

The study of transient excitation of three-level systems is a mature field, but there is still a need for experimental verifications of theoretical work. An early theoretical paper by Berman and Salomaa [11] compared the dressed-atom and bare-atom pictures, and considered transients after probe turn-on. Related dressed-atom transients for two-level atoms are presented theoretically by Lu and Berman [12]. Theoretical three-level transient studies considering initial conditions have also appeared in Lu *et al.* [13]. Harris and Luo [14] studied transient EIT in the context of the energy required for the preparation of EIT. Li and Xiao [15] investigated the time required for the onset of EIT and Zhu considered the conditions required for observing inversionless gain in the transient regime for the V [16] and Λ [17] schemes. The latter is especially interesting from the point of view of lasing without inversion.

Experimental work looking at dressed-state transients includes phase shifting measurements in a two-level system [18], fluorescence measurements on a three-level Λ system [19] and pump-probe experiments on a three-level ladder system [20]. Transient gain was first observed experimentally in a sodium sample in a Λ configuration by Fry *et al.* [21]. Their observations included transient gain of a strong field when a weak field

was switched on by a Pockels cell in the presence of incoherent pumping to the upper level, but without population inversion. This is also the only previous experiment we know of which analysed transient dynamics associated with the turn-off of the coupling field. Transient ringing of a three-level system with gain has been observed in the radio-frequency regime in nitrogen-vacancy centres in diamond [22] but not yet in the optical region. Since the ringing occurs at approximately the Rabi frequency of the strong field, experiments in the optical region need to be carried out in a Doppler-free configuration or ideally in a laser-cooled sample to avoid the Doppler effects masking the coherent effects. Earlier work in this laboratory has demonstrated transient EIT [7] in a cold rubidium Λ system after rapidly switching on a resonant coupling field, but no ringing was observed.

1.1.2 Four-level systems

The exploitation of EIT has lead to interest in more complex systems involving multiple electromagnetic fields interacting with either a single transition [23] or with several transitions [24-28]. In particular there is now huge interest in exploiting non-linearities in four-level systems with applications in quantum optics [1-4] and four-wave mixing [27].

Four-level systems of various configurations can be excited with different pumping schemes. Several theoretical studies have considered three-level ladder configurations coherently prepared by two strong cw lasers [24,25]. They predict a three-peak spectrum when the lowest or highest of the three levels is probed via a fourth level or monitored by fluorescence. When the two dressing beams are on resonance this spectrum has the form of a Doppler-free three-photon absorption peak situated centrally within an EIT window [24]. More generally, the positions and intensities of the three peaks are functions of the Rabi frequencies and detunings of the two strong beams. The

trajectories of the peaks as a function of Rabi frequencies and detunings have been described in doubly dressed analyses [25].

None of these three studies was accompanied by experimental verifications. Our work [29] and one other [30,31] have since demonstrated these results.

1.2 Aims of this work

All of the experimental work in this thesis was conducted in an Rb MOT that has been in operation in our laboratory for 5 years before the project began. However, considerable developmental work has been carried out on this MOT and the laser systems during the course of this project, and this work dominated the first 18 months of the Author's studentship. This developmental work is described in Chapter 4.

Continuing the work done on transient EIT previously in this laboratory [7,8], we aim to drive the transient Rabi oscillations into gain and perform further investigations of transient effects. This is one of the reasons behind the developmental work carried out on the lasers to increase the laser power available to the coupling field. In Chapter 5 we present a study of transient EIT with this improved power and for a wide range of parameters never studied before.

In the case of the doubly-driven system, we aim to observe experimentally the spectra predicted by the previous theoretical studies [24,25]. As mentioned before, these studies were not experimentally investigated at the time this work was done, and so there was a need for this investigation. We describe in Chapter 6 the experiments performed in this respect. We were also interested in measuring the dispersion of such systems. This experiment is being carried out at the time of writing this thesis, but no results have been obtained yet.

My major role has been that of the principal hands-on experimenter, responsible for carrying out the developmental work and the day-to-day development and running of the experiments. I have also made significant contributions to the theoretical work. In all of this I have worked closely with my colleagues, especially Dr. A. D. Greentree, and our partners at Imperial College and the University of Hertfordshire.

1.3 Organisation of this thesis

Chapters 2 and 3 are intended to set the scene by describing some of the background work and fundamental ideas behind this project. Chapter 2 starts with a brief description of the theory of electromagnetically induced transparency (EIT), both steady-state and transient, and doubly-driven four-level systems. Following this, Chapter 3 presents a short review of the mechanisms behind optical molasses and the magneto-optical trap relevant to our experimental set-up.

Chapters 4, 5 and 6 of this thesis describe the original work that we have carried out. Chapter 4 describes the development work carried out on the experimental set-up used in previous experiments in this laboratory. This newly developed set-up was then used in the experiments described in Chapter 5 for the study of transient EIT in the turn-on and turn-off regime, both resonant and non-resonant. Further experiments in the developed set-up were performed to study the absorption spectra of a doubly-driven four-level N system, which are described in Chapter 6.

We finish by presenting the summary, conclusions and suggestions for further work in Chapter 7. Further information to complement this thesis appears in the three Appendices.

Chapter 2

Coherently Prepared Systems

Lasers can be used to control and prepare the coherences of an atomic system as well as the populations. Coherently prepared systems in three-level atoms have been studied since 1976, when Arimondo and Orriols [32] proposed the use of two cw lasers to prepare a coherent superposition of two ground states where the population is trapped in a dark state. Coherent population trapping (CPT) was then first observed by Alzetta *et al.* in 1976 [33] with rf fields in a Na vapour. For reviews of CPT refer to [34,35]. These studies paved the way for the later use of CPT as a way of inducing transparency in an absorbing transition, an effect known as *electromagnetically induced transparency* (EIT). In this Chapter we will briefly discuss the main ideas behind EIT in three-level Λ systems, and give a brief introduction to coherence effects in four-level systems. For reviews on EIT refer to [36].

Section 2.1 describes the basics of EIT, both steady-state and transient, paying special attention to the Λ-type system we will study theoretically and experimentally in the transient regime in Chapter 5. This Section includes a discussion of light and dark states as well as the dressed-state approach. The density matrix equations are presented in full and relevant solutions are quoted. Then in Section 2.2 we will briefly discuss coherence effects in 4-level systems and their proposed application to photon blockade [1-4] and the single-photon switch of Harris and Yamamoto [9]. A detailed theoretical and experimental study of a four-level N system is the subject of Chapter 6 of this thesis.

2.1 EIT in lambda systems

EIT was first proposed by Harris *et al.* in 1990 [37] as a means to study resonantly enhanced non-linear optical processes. In fact, EIT allows a probe beam to experience a resonantly enhanced non-linear refractive index and an induced transparency at the same time. EIT was first observed by Boller *et al.* in 1991 [38] in a strontium vapour using high-power pulsed lasers. Since then, EIT optical experiments have been carried out in vapour cells [39-42], atomic beams [43], MOTs [44,45] and BECs [46], and it has been used in many applications in non-linear optics, such as coherent switching [47], enhancement of FWM [37,48], lasing without inversion [43,49-52], and more recently ultra-slow light propagation [5,6] and storage [53,54], and cooling of trapped ions [55-57].

2.1.1 Qualitative discussion of steady-state EIT

EIT can be produced in a three-level system using a strong resonant coupling field C and a weak resonant probe field P in the V, Λ or cascade/ladder configuration, as

shown in Figure 2.1. These configurations are essentially the same except for the different decay and decoherence rates involved [39]. For the moment we ignore level degeneracies and assume there are no decay mechanisms other than the spontaneous decay of the excited states. We will consider the Λ configuration from now on because this is the one that has been chosen for the experiments of Chapters 5 and 6.

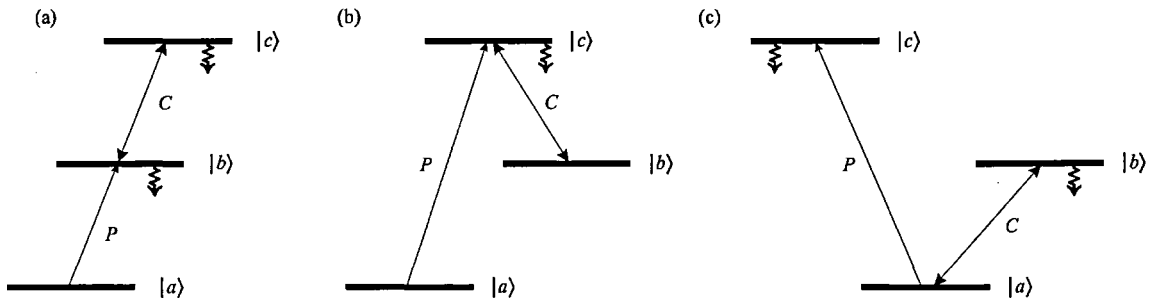

Figure 2.1 - EIT systems. (a) cascade or ladder, (b) Λ and (c) V systems.

From the theory of CPT [34,35,58], it is known that, in the presence of the two laser fields C and P, the population of the two ground states of a Λ system such as the one in Figure 2.1(b) will be optically pumped into a coherent superposition of these states, called a dark state. When both fields are on resonance, the dark (non-absorbing) state $|D\rangle$ and the orthogonal light (absorbing) state $|L\rangle$ have the form [34]

$$|D\rangle = \frac{\Omega_p|b\rangle - \Omega_C|a\rangle}{\sqrt{\Omega_p^2 + \Omega_C^2}},$$
$$|L\rangle = \frac{\Omega_C|b\rangle + \Omega_p|a\rangle}{\sqrt{\Omega_p^2 + \Omega_C^2}}, \tag{2.1}$$

where Ω_α is the Rabi frequency of field α. The two laser fields interact only with the light state, optically pumping all the population into the dark state.

EIT is a special case of CPT where one of the optical fields, the coupling field, is much stronger than the other. This makes the steady-state population of one of the ground states very much higher than that of the other in an EIT experiment. With this condition, $\Omega_p \ll \Omega_C$, (2.1) becomes

$$|D\rangle \approx |a\rangle, \quad |L\rangle \approx |b\rangle. \tag{2.2}$$

This means that C and P optically pump all the population into a dark state that is approximately $|a\rangle$ so that the transition $|a\rangle - |c\rangle$ becomes transparent, giving access to a region of very strong dispersion and a resonantly enhanced non-linear susceptibility [37]. At the practical level, the interest in CPT is mainly in the changes of state populations, while in EIT it is in transition coherences.

Of more interest from the point of view of this thesis is an understanding of EIT by means of dressed states. Dressed states are treated in many textbooks and papers, for example [11,59]. Figure 2.2 shows the resonant Λ system in the bare and dressed-state basis. In the dressed-state basis the atom and the coupling field are treated as a whole to produce two states $|+\rangle$ and $|-\rangle$, of the form

$$|+\rangle = \frac{|b\rangle + |c\rangle}{\sqrt{2}}, \quad |-\rangle = \frac{|b\rangle - |c\rangle}{\sqrt{2}}. \tag{2.3}$$

The energies of these states lie symmetrically about the energy of the bare $|c\rangle$ state,

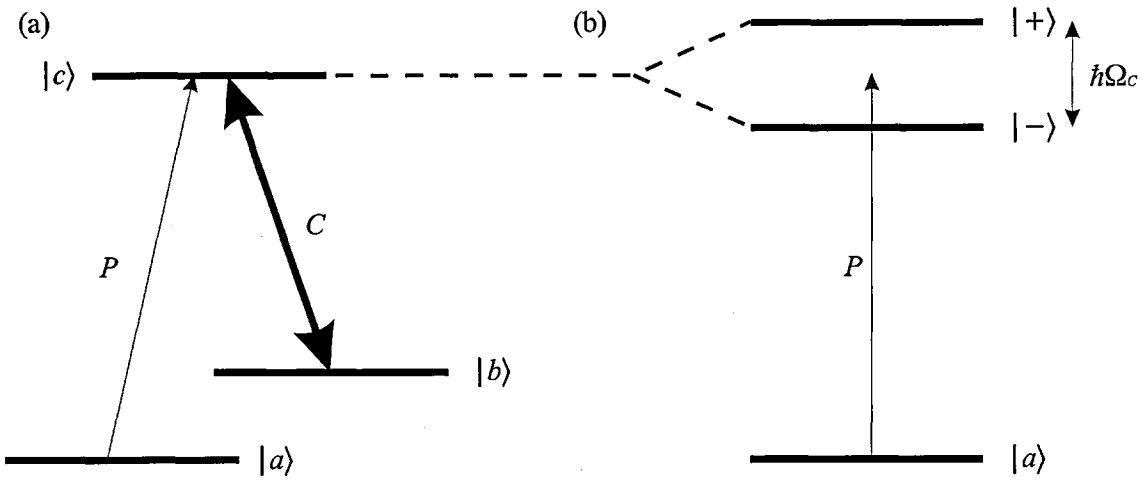

Figure 2.2 - Λ-type EIT system in the (a) bare state and (b) dressed state bases.

with a splitting of $\hbar\Omega_C$ due to the atom-laser interaction. This splitting gives rise to the well-known Autler-Townes doublet [60].

For Rabi frequencies of the coupling field much greater than the natural linewidth Γ of the transition, the separation between the dressed states is big enough to make the probe transition transparent. However, if $\Omega_C \approx \Gamma$ one might expect the two lineshapes of the dressed states to overlap and destroy the transparency, but this is not the case, provided the two-photon coherence between the two ground states $|a\rangle$ and $|b\rangle$ is maintained. In fact, if one computes the transition amplitude of the probe transition, the contributions from $|+\rangle$ and $|-\rangle$ will have opposite signs and will cancel each other out. Hence the transparency arises from the quantum destructive interference of the transition amplitudes to the two dressed states [61].

When the coupling field is detuned from resonance, the dressed states are asymmetrically split as shown in Figure 2.3. Transparency still occurs, although now when the two-photon resonance condition is satisfied, i.e. when both fields are detuned by the same amount Δ. In this case, the splitting between the dressed states is $\hbar\sqrt{\Omega_C^2 + \Delta^2}$, with the energies of $|+\rangle$ and $|-\rangle$, with respect to the energy of $|c\rangle$, being

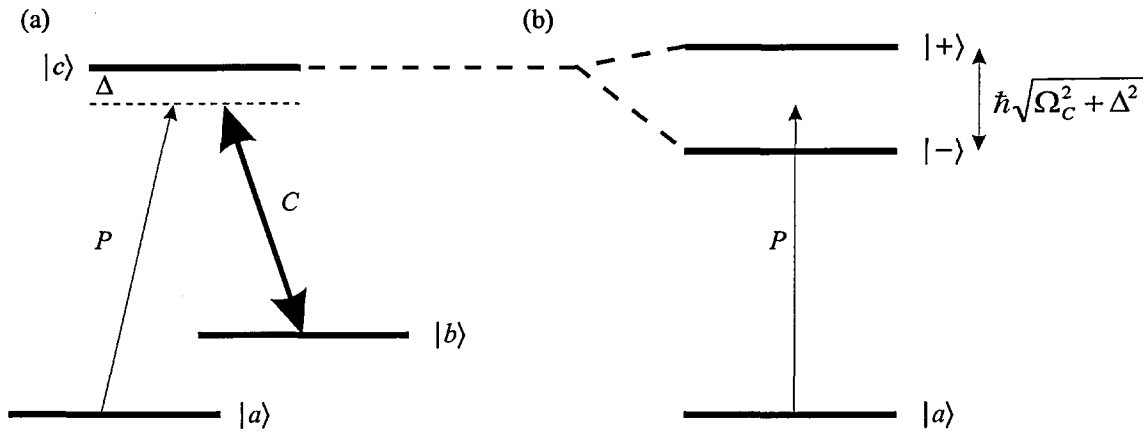

Figure 2.3 – (a) Bare and (b) dressed state picture when the coupling field is non-resonant.

$$\begin{aligned} \mathcal{E}_+ &= \hbar\frac{\Delta+\sqrt{\Omega_C^2+\Delta^2}}{2}, \\ \mathcal{E}_- &= \hbar\frac{\Delta-\sqrt{\Omega_C^2+\Delta^2}}{2}, \end{aligned} \tag{2.4}$$

respectively.

Other pictures have been used to describe the EIT mechanism. For example, EIT can be thought of a destructive interference between the one-photon transition and the three-photon transition between $|a\rangle$ and $|c\rangle$. However, we shall not use these pictures in this thesis.

2.1.2 Density matrix equation for Λ-type EIT

To get a quantitative picture of EIT, we consider the Hamiltonian $\hat{H}$ of the system of Figure 2.1(b) in the electric dipole and rotating wave approximations

$$\hat{H} = -\hbar\omega_{ca}|a\rangle\langle a| - \hbar\omega_{cb}|b\rangle\langle b| - \left(\hbar\frac{\Omega_p}{2}e^{-i\omega_p t}|c\rangle\langle a| + \hbar\frac{\Omega_C}{2}e^{-i\omega_C t}|c\rangle\langle b| + H.c.\right), \tag{2.5}$$

where $\hbar\omega_{ca}$ ($\hbar\omega_{cb}$) is the energy of state $|a\rangle$ ($|b\rangle$) and ω_p (ω_C) is the frequency of the probe (coupling) beam. Transforming to a rotating frame gives the time-independent Hamiltonian

$$\hat{H} = \hbar\Delta_p|a\rangle\langle a| + \hbar\Delta_C|b\rangle\langle b| - \left(\hbar\frac{\Omega_p}{2}|c\rangle\langle a| + \hbar\frac{\Omega_C}{2}|c\rangle\langle b| + H.c.\right), \tag{2.6}$$

where $\Delta_p=\omega_p-\omega_{ca}$ ($\Delta_C=\omega_C-\omega_{cb}$) is the detuning of the probe (coupling) field. The Rabi frequency Ω_α of field α is defined as $\Omega_\alpha=\mathbf{E}_\alpha\cdot\mathbf{d}_{\beta\gamma}/\hbar$, where $\mathbf{d}_{\beta\gamma}$ is the electric dipole moment of the transition $|\beta\rangle-|\gamma\rangle$ and $\mathbf{E}_\alpha$ the electric field of the laser, being $|\mathbf{E}_\alpha|=E_\alpha=\mathcal{E}_\alpha e^{i\omega_\alpha t}+c.c.$

If we consider an ensemble of particles immersed in the radiation fields, the state of these particles is, in general, a statistical mixture of eigenstates $|\psi\rangle$ of $\hat{H}$ with weight w_ψ, described by the density operator

$$\hat{\rho}=\sum_{\psi} w_\psi |\psi\rangle\langle\psi|. \tag{2.7}$$

The master equation describing the system can then be written as [62]

$$\begin{aligned}\frac{d\hat{\rho}}{dt}=\frac{1}{i\hbar}\left[\hat{H},\hat{\rho}\right]&-\Gamma_{ca}\left(|c\rangle\langle c|\hat{\rho}+\hat{\rho}|c\rangle\langle c|-2|a\rangle\langle c|\hat{\rho}|c\rangle\langle a|\right)\\&-\Gamma_{cb}\left(|c\rangle\langle c|\hat{\rho}+\hat{\rho}|c\rangle\langle c|-2|b\rangle\langle c|\hat{\rho}|c\rangle\langle b|\right)\\&-\Gamma_{ba}\left(|b\rangle\langle b|\hat{\rho}|a\rangle\langle a|+|a\rangle\langle a|\hat{\rho}|b\rangle\langle b|\right),\end{aligned} \tag{2.8}$$

where $\Gamma_{c\alpha}$ is the spontaneous decay rate from state $|c\rangle$ to state $|\alpha\rangle$, Γ_{ba} is the non-radiative two-photon dephasing rate between the two ground states. The matrix elements of this equation are [15,63]

$$\begin{aligned}\dot{\rho}_{aa}&=\Gamma_{ca}\rho_{cc}+i\frac{\Omega_p}{2}\left(\rho_{ca}-\rho_{ac}\right),\\ \dot{\rho}_{ab}&=\left(-i\Delta_{pC}-\Gamma_{ba}\right)\rho_{ab}+i\left[-\frac{\Omega_C}{2}\rho_{ac}+\frac{\Omega_p}{2}\rho_{cb}\right],\\ \dot{\rho}_{ac}&=\left(-i\Delta_p-\frac{\Gamma}{2}\right)\rho_{ac}+i\left[-\frac{\Omega_C}{2}\rho_{ab}+\frac{\Omega_p}{2}\left(\rho_{cc}-\rho_{aa}\right)\right],\\ \dot{\rho}_{bb}&=\Gamma_{cb}\rho_{cc}+i\frac{\Omega_C}{2}\left(\rho_{cb}-\rho_{bc}\right),\\ \dot{\rho}_{bc}&=\left(-i\Delta_C-\frac{\Gamma}{2}\right)\rho_{bc}+i\left[\frac{\Omega_C}{2}\left(\rho_{cc}-\rho_{bb}\right)-\frac{\Omega_p}{2}\rho_{ba}\right],\\ \dot{\rho}_{cc}&=-\Gamma\rho_{cc}+i\left[\frac{\Omega_C}{2}\left(\rho_{bc}-\rho_{cb}\right)+\frac{\Omega_p}{2}\left(\rho_{ac}-\rho_{ca}\right)\right],\\ \rho_{\alpha\beta}&=\rho^*_{\beta\alpha},\\ 1&=\rho_{aa}+\rho_{bb}+\rho_{cc}.\end{aligned} \tag{2.9}$$

where $\Gamma=\Gamma_{ca}+\Gamma_{cb}$ is the total decay rate of state $|c\rangle$.

Steady-state EIT solution

Assuming that $\Omega_C \gg \Omega_p$, most of the population will be pumped into state $|a\rangle$ in the steady-state, i.e. $\rho_{aa} \approx 1$, $\rho_{bb} \approx \rho_{cc} \approx 0$. So, keeping only the first order of Ω_p and solving (2.9) we have

$$\rho_{ac} \approx \frac{i\Omega_p/2}{\frac{\Gamma}{2} - i\Delta_p + \frac{\Omega_C^2/4}{\Gamma_{ba} - i(\Delta_p - \Delta_C)}}, \tag{2.10}$$

and the linear susceptibility is given by [41,64]

$$\chi^{(1)} = \frac{2\eta\mu_{ca}^2}{\hbar\Omega_p}\rho_{ac}, \tag{2.11}$$

where η is the atomic density. Figure 2.4 shows the probe absorption and dispersion, which are proportional to $\mathrm{Im}(\rho_{ac})$ and $\mathrm{Re}(\rho_{ac})$ respectively, as a function of Δ_p, assuming $\Gamma_{ba}=0$. The black traces on each plot show the case of a resonant coupling field ($\Delta_C=0$), and the blue traces show the case of a coupling field detuned by an amount $\Delta_C=\Gamma$. In this case, transparency happens when the two-photon resonance condition $\Delta_p=\Delta_C$ occurs.

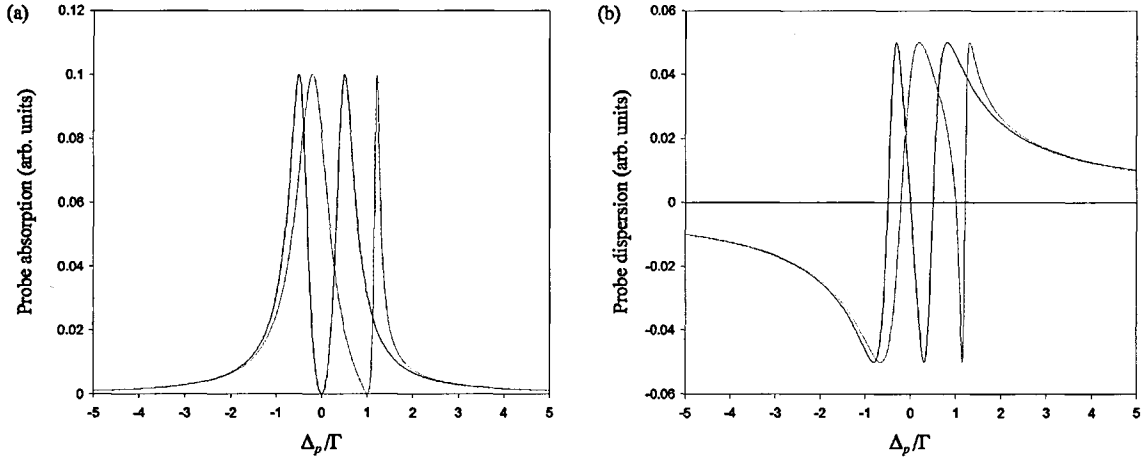

Figure 2.4 – Effect of coupling field detuning on steady-state EIT (a) absorption and (b) dispersion. Black lines correspond to $\Delta_C=0$ and blue lines to $\Delta_C=\Gamma$.

The effect of the two-photon dephasing rate Γ_{ba} on EIT is to diminish the coherence between states $|a\rangle$ and $|b\rangle$, hence reducing the quantum interference that

produces the transparency window. This dephasing rate may arise from incoherent coupling of the two ground states due to experimental causes, such as the finite linewidth of the lasers. Figure 2.5 shows EIT absorption and dispersion traces for two different values of Γ_{ba}.

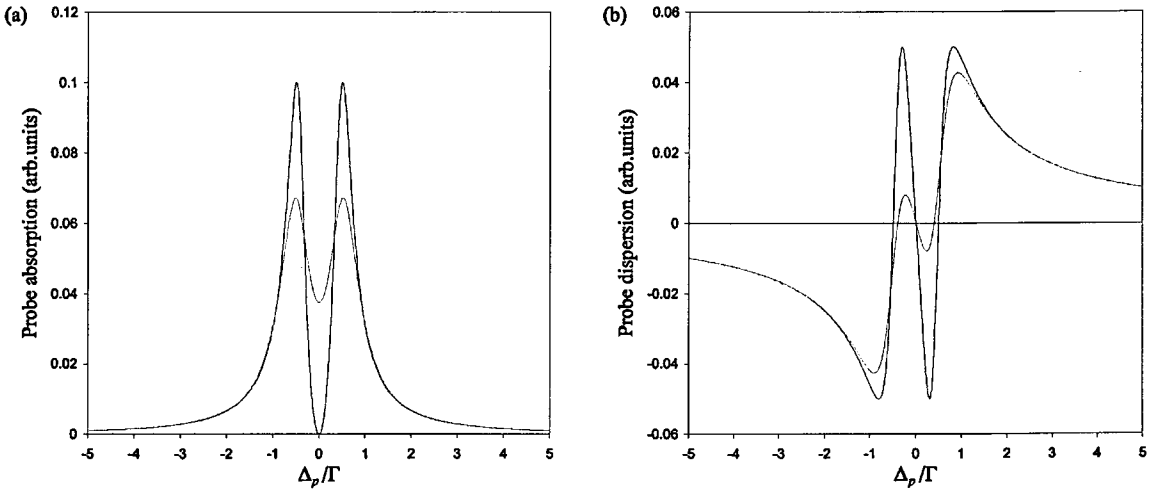

Figure 2.5 – Effect of the two photon dephasing in steady-state EIT (a) absorption and (b) dispersion. Black lines correspond to $\Gamma_{ba}=0$ and blue lines to $\Gamma_{ba}=0.3\Gamma$.

Transient EIT solution

So far, we have looked at the steady-state response of EIT. We now describe the probe transient response when we non-adiabatically switch on the coupling field. The first study of the transient behaviour of EIT was done by Li and Xiao in 1995 [15]. They studied a ladder EIT system (Figure 2.1(a)) theoretically, although the results also apply to Λ-type systems. Here we consider a simple special case where both fields are on resonance and the coupling field is switched on at time $t=0$. This case will serve to illustrate some of the main features of transient EIT, which is a major topic of this thesis (Chapter 5).

We assume that the probe field is on all the time, so that before the coupling field is switched on at time $t=0$, the atoms are coherently excited by the weak probe field, setting the initial conditions for (2.9), i.e. [15]

$$\rho_{cc}(0)-\rho_{aa}(0)\approx -1+\frac{\Omega_p^2}{2\left(\Delta_p^2+\frac{\Gamma^2}{4}\right)},$$
$$\rho_{ac}(0)=\frac{i\Omega_p}{\Gamma-i2\Delta_p}, \tag{2.12}$$
$$\rho_{bc}(0)=0.$$

If we assume that $\Omega_p \ll \Omega_C$, Γ_{ca}, then the second and third equations of (2.9) can be simplified to first order in Ω_p as

$$\dot{\rho}_{ab}=\left(-i\Delta_{pC}-\Gamma_{ba}\right)\rho_{ab}+i\left[-\frac{\Omega_C(t)}{2}\rho_{ac}\right],$$
$$\dot{\rho}_{ac}=\left(-i\Delta_p-\frac{\Gamma}{2}\right)\rho_{ac}+i\left[-\frac{\Omega_C(t)}{2}\rho_{ab}-\frac{\Omega_p}{2}\right]. \tag{2.13}$$

For the resonant case $\Delta_p=\Delta_C=0$ and assuming $\Gamma_{ba}=0$, these equations have a solution

$$\rho_{ac}(t)=\rho_{ac}(0)e^{-\Gamma t/4}\left[\cos\left(\frac{ft}{2}\right)-\frac{\Gamma}{2f}\sin\left(\frac{ft}{2}\right)\right], \tag{2.14}$$

where $f=\sqrt{\Omega_C^2-(\Gamma/2)^2}$.

Figure 2.6 shows $\mathrm{Im}(\rho_{ac})$, proportional to the probe absorption, as a function of normalised time Γt for different values of Ω_C. The probe absorption exhibits damped oscillations of frequency f, with probe gain for negative values of $\mathrm{Im}(\rho_{ac})$, and settling at $\mathrm{Im}(\rho_{ac})=0$, which corresponds to the steady-state transparency. It can be shown [65] that the gain periods are not accompanied by population inversion in the bare atom basis, but there is inversion in a dressed basis.

The origins of this effect in the absence of decay are easily demonstrated using the 3-D Vector Model of 3-state systems introduced recently [66,67]. This model is based on the representation of the state of the atom $|\psi(t)\rangle=v_a|a\rangle+v_b|b\rangle+iv_c|c\rangle$ by the real 3-dimensional vector $\mathbf{v}(t)=(v_a, v_b, v_c)$, where here the states $|a\rangle$, $|b\rangle$ and $|c\rangle$ represent the bare energy eigenstates of the atom, and the phase i in the level $|c\rangle$ amplitude allows the

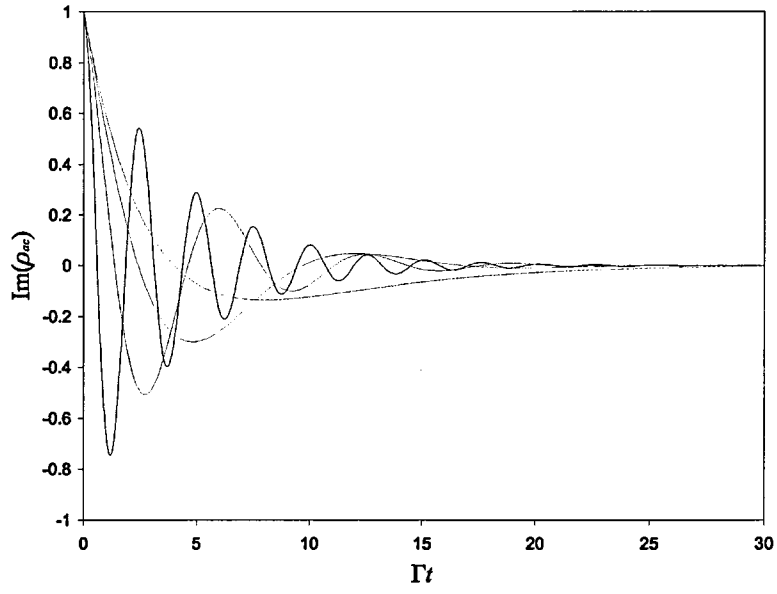

Figure 2.6 - Transient probe absorption as a function of time. (black) Ω_C=5Γ, (blue) Ω_C=3Γ, (red) Ω_C=Γ, and (green) Ω_C=Γ/2.

v_a to be real for all time when both lasers are resonant. The components of **v** are given with respect to three orthogonal axes which we shall call the *a*, *b* and *c* axes, as shown on Figure 2.7. These axes represent the three energy eigenstates of the atom.

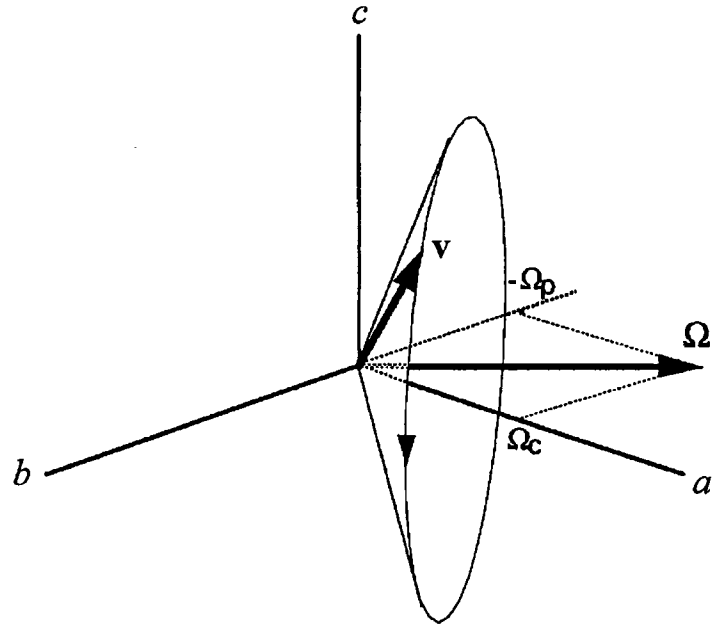

Figure 2.7 - 3-D vector model of transient EIT ringing.

The action of the (resonant) probe and coupling fields on $|\psi\rangle$ is represented simply as a rotation about a *Rabi vector* $\Omega=(\frac{1}{2}\Omega_C, -\frac{1}{2}\Omega_p, 0)$ as follows:

$$\frac{d\mathbf{v}}{dt}=\Omega\times\mathbf{v}. \tag{2.15}$$

The rotation of $\mathbf{v}$ about Ω occurs at the frequency $\Omega\equiv|\Omega|=\frac{1}{2}\left(\Omega_1^2+\Omega_2^2\right)^{1/2}$, which is approximately $\Omega_C/2$ for $\Omega_p\ll\Omega_C$. The Rabi vector lies in the *a-b* plane at an angle of $\theta=\tan^{-1}(\Omega_p/\Omega_C)\approx\Omega_p/\Omega_C$ to the *b* axis. The value of ρ_{ac} is the product of the amplitude of the state $|a\rangle$ and the complex conjugate of the amplitude of state $|c\rangle$ in $|\psi\rangle$, which corresponds to the product $-iv_av_c$, and so $\mathrm{Im}(\rho_{ac})=-v_av_c$. Absorption of the probe occurs when $v_av_c<0$ and gain when $v_av_c>0$.

With the addition of decay rates, these are the transient Rabi oscillations seen in Figure 2.6. The full 3-D Vector-Model treatment, including decay rates and detunings, can be found in [67].

2.1.3 Some recent applications of EIT

Recently, EIT has been used in several applications. Here, we briefly describe two of them: ultra-slow and super-luminal light propagation, and EIT cooling of trapped ions.

Ultra-slow and super-luminal light propagation

Ultra-slow light propagation was first observed by Hau *et al.* in 1999 [5] in an experiment with an ultra-cold gas sample of Na atoms. This phenomenon is based on the steep dispersion curve obtained near resonance in an EIT system (see Figure 2.4(b)). This steep dispersion curve results in very low group velocities v_g for optical pulses, which can be written as [5]

$$v_g = \frac{c}{n(\omega_p) + \omega_p \dfrac{dn}{d\omega_p}} \approx \frac{\hbar c \epsilon_0}{2\omega_p} \frac{\Omega_C^2}{\mu_{ac}^2 \eta}, \tag{2.16}$$

where n is the refractive index of the sample, c is the speed of light, ϵ_0 is the permitivity of free space and η is the atomic density. The annulment of absorption and the fact that $d^2n/d\omega_p^2 = 0$ when the fields are on resonance, makes it possible for a pulse to propagate through the sample without being absorbed nor reshaped, while at the same time experience an ultra-low group velocity (see Figure 2.8).

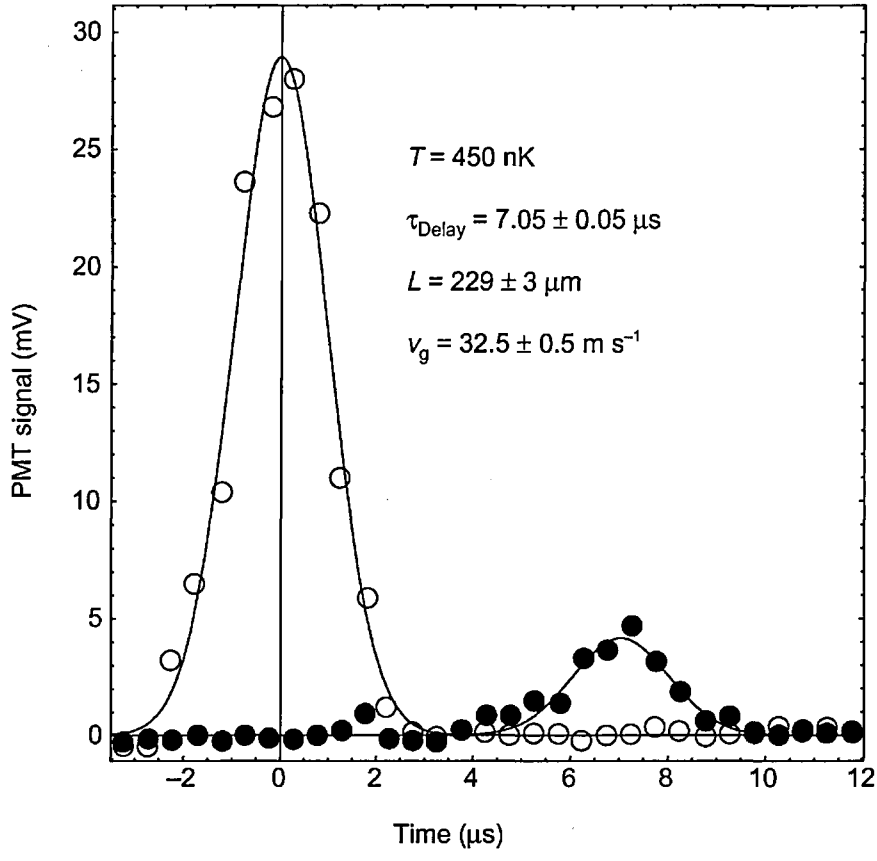

Figure 2.8 - Figure 3 of Hau *et al.* [5], showing the low group velocity experienced by a pulse. The open circles are a reference pulse which does not experience delay, while the filled circles are the delayed pulse.

Hau *et al.* observed group velocities as low as 17 m/s when working with a sodium BEC at 50 nK and coupling field intensities of 12 mW/cm^2 (Ω_C=0.56Γ). They also observed larger values of v_g for higher temperatures and coupling field intensities.

Subsequent experimental studies in rubidium cells [6] have achieved group velocities as low as 8 m/s.

Liu *et al.* [53] used the same principle to store coherent optical information in a cloud of Na atoms. They adiabatically turned off the coupling field before the probe pulse was able to propagate through the medium, storing in this way the dark coherent superposition of states $|a\rangle$ and $|b\rangle$ (state $|D\rangle$ of (2.1)). They were then able to retrieve

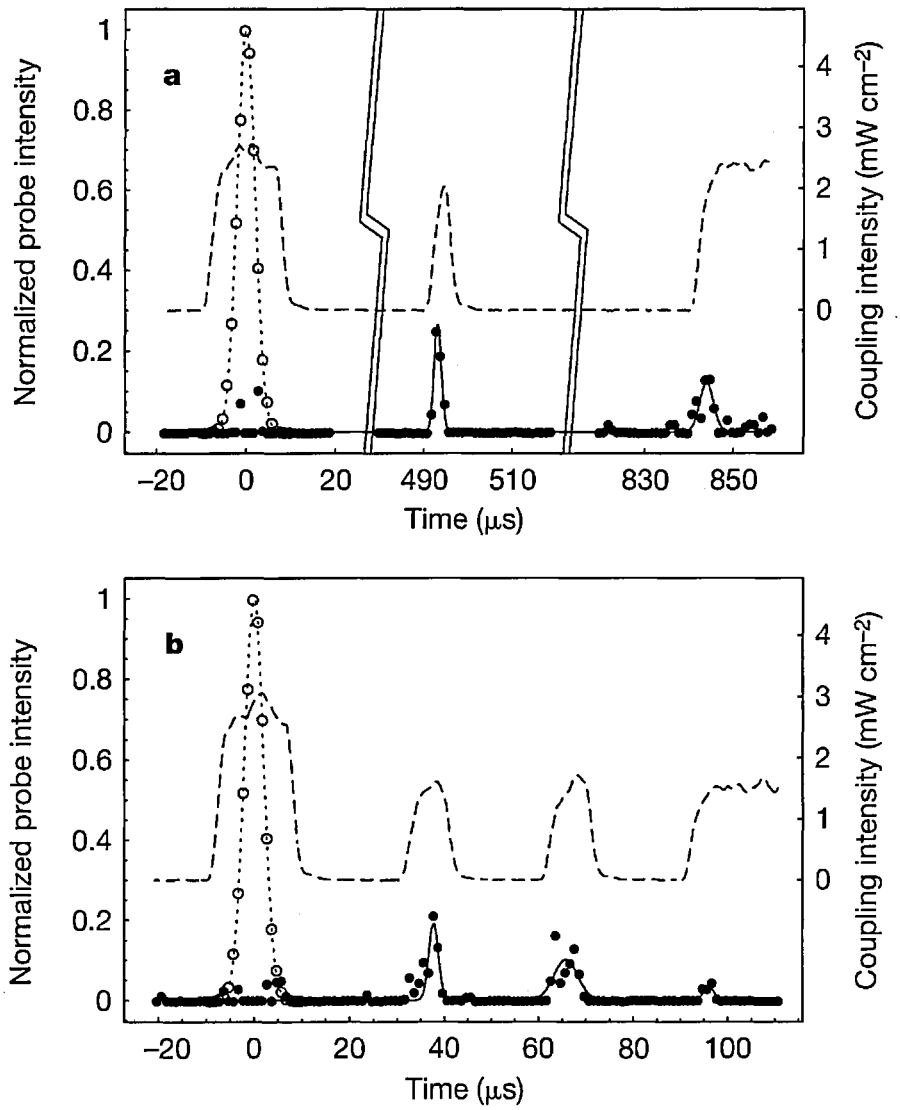

Figure 2.9 - Figure 4 of Liu *et al.* [53], showing the storage and retrieval of light pulses. Two pulses are retrieved in (a) and three in (b). Open circles represent reference pulses, filled circles represent the retrieved pulses, and the dashed lines represent the coupling beam intensity.

up to three copies of the initial probe pulse, spaced by up to hundreds of microseconds, by pulsing the coupling field back on (see Figure 2.9). The same effect was reported at the same time by Phillips *et al.* [54] working with a Rb vapour cell.

Conversely to EIT dispersion, between two closely spaced gain lines, an anomalous dispersion region appears where $dn/d\omega_p$ is negative. Thus, the group velocity of a light pulse can become greater than c or even negative [68]. Wang *et al.* [69] observed this effect in a caesium vapour cell, and obtained group velocities as low as $v_g = -c/310$. In practice, this means that a light pulse propagating through the cell appears at the exit side so much earlier than if it had propagated the same distance in a vacuum, that the peak of the pulse appears to leave the cell before entering it. Dogariu *et al.* presented a more detailed study of their previous experiments [69] in [70].

EIT cooling of trapped ions

This application of EIT was first proposed by Morigi *et al.* in 2000 [55], and then realised by Roos *et al.* and Schmidt-Kaler *et al.* [56]. Here, EIT is used to couple vibrational transitions of the trapped ions that lower their vibrational energy, while at the same time inhibiting or reducing those transitions that do not change or increase their vibrational energy. Figure 2.10(a) shows the three-level system used for EIT cooling, where a coupling beam of Rabi frequency Ω_r drives the $|r\rangle - |e\rangle$ transition off-resonantly with a detuning Δ_r. A cooling (probe) beam with Rabi frequency Ω_g probes the $|g\rangle - |e\rangle$ transition. The profile observed with this field is shown in the inset of Figure 2.10(a), and corresponds to a typical detuned EIT profile (see Figure 2.4).

When the harmonic motion of the ions is taken into account, the mutual detuning resonance corresponds to the $|g, m\rangle \rightarrow |e, m\rangle$ transition (carrier), where m represents the vibrational state, which is therefore cancelled, as shown in Figure 2.10(b). The spectrum can be adjusted so that there is strong absorption on the $|g, m\rangle \rightarrow |e, m-1\rangle$ transition

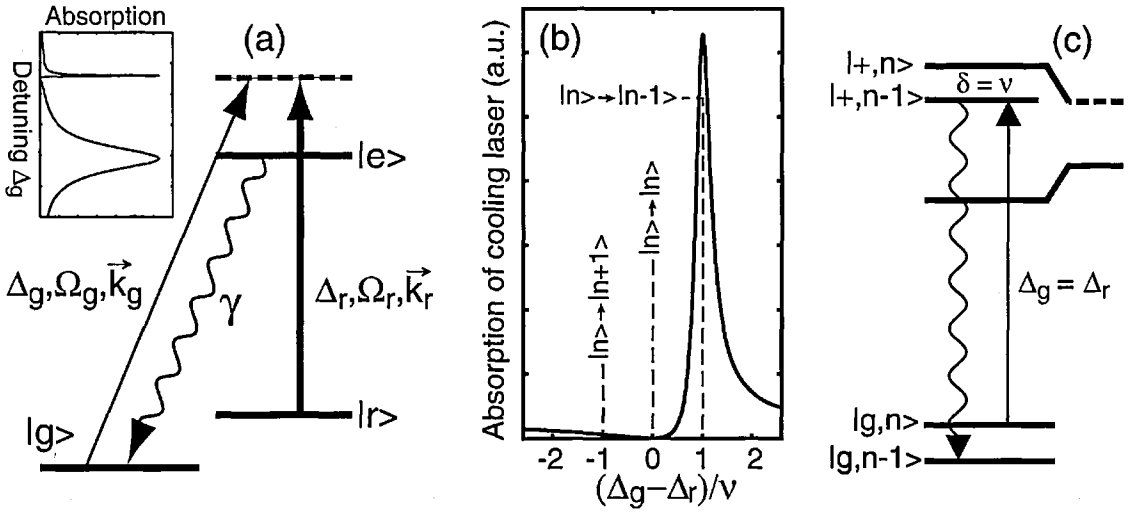

Figure 2.10 - Figure 1 of Morigi *et al.* [55] showing (a) levels and transitions of the cooling scheme, (b) absorption of cooling laser and probabilities of carrier and sideband transitions, and (c) dressed-state picture of the scheme. In this Figure *n* refers to the vibrational state *m*.

(red sideband) by setting the Rabi frequency Ω_r and detuning Δ_r for this condition. At the same time, the $|g, m\rangle \rightarrow |e, m+1\rangle$ transition (blue sideband) experiences a very small excitation probability. This way, atoms will be almost purely excited on the red sideband to then decay to the $|g, m-1\rangle$ ground state, losing vibrational energy, as shown in the dressed-state picture of Figure 2.10(c).

Experimental realisations of this technique [56] with Ca^+ in a 3D-quadrupole Paul trap [57], have achieved mean vibrational numbers as low as $\overline{m} = 0.1$, which correspond to a ground-state occupation probability of 90%.

2.2 Coherence effects in 4-level systems

Recently, there has been much interest in the study of 4-level atoms, especially the interaction of them with light beams at the few-photon level. There has however been very little study of the basic coherence properties of such systems. Some previous work in four-level coherences has been from the point of view of a doubly-driven three-level

system probed to a fourth level, analysed in terms of doubly dressed states. This is a major topic of this thesis. In Chapter 6 we present a theoretical study of a four-level N system and the first experimental study of the spectra of such a system in the optical domain.

The first theoretical studies of doubly-driven systems were in 1997, when Sandhya and Sharma [24] and Sadeghi *et al.* [25] presented studies of the probe spectra in this kind of system. Sandhya and Sharma predicted the appearance of a third peak between the two Autler-Townes peaks of a ladder system when a second coupling field is applied between $|c\rangle$ and a fourth, higher energy state $|d\rangle$ (Figure 2.11(a)). They also predict the growth of this third peak as the Rabi frequency of the second coupling field C_2 is increased. Sadeghi *et al.* studied the three-peak absorption spectra of a so-called Π system: a Λ system with a second coupling field applied between $|b\rangle$ and a fourth level whose energy lies between the energies of $|a\rangle$ and $|b\rangle$ (Figure 2.11(b)). They predicted the appearance of transparency windows with tunable central frequencies equal to the Rabi frequency of the second coupling field and widths proportional to that of the first coupling field.

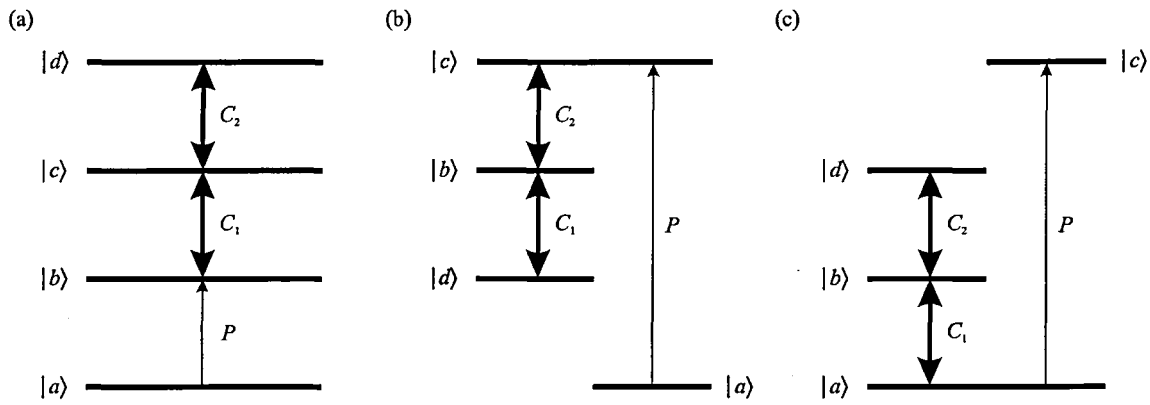

Figure 2.11 - Doubly-driven 4-level systems: (a) ladder-like, (b) Λ-like or Π, and (c) V-like system.

2.2.1 Dressed state studies of 4-level schemes

The two theoretical studies described above based their results on the numerical integration of the master equation of the system in question. However, a more natural approach is the dressed-atom formalism introduced by Wei *et al.* in 1998 [26] and used later by Lukin *et al.* [27] and by us [29].

Wei *et al.* studied theoretically the system of Figure 2.11(c), which is driven by two coupling fields C_1 and C_2 of Rabi frequencies Ω_1 and Ω_2, and probed by a weak probe field P. The three-level ladder system formed by the two coupling fields is described by a Hamiltonian that can be written as

$$\hat{H} = -\hbar\Delta_1|b\rangle\langle b| - \hbar(\Delta_1+\Delta_2)|d\rangle\langle d| + \left(\hbar\frac{\Omega_1}{2}|b\rangle\langle a| + \hbar\frac{\Omega_2}{2}|d\rangle\langle b| + H.c.\right), \qquad (2.17)$$

in the rotating frame, where Δ_1 and Δ_2 are the detunings of fields C_1 and C_2, respectively. In the basis of states $|a\rangle$, $|b\rangle$ and $|d\rangle$, the matrix representation of (2.17) can be written as

$$\hat{H} = \begin{pmatrix} 0 & \frac{\hbar\Omega_1}{2} & 0 \\ \frac{\hbar\Omega_1}{2} & -\hbar\Delta_1 & \frac{\hbar\Omega_1}{2} \\ 0 & \frac{\hbar\Omega_1}{2} & -\hbar(\Delta_1+\Delta_2) \end{pmatrix}. \qquad (2.18)$$

When diagonalising (2.18), we obtain three uncoupled dressed states:

$$\begin{aligned} |D_1\rangle &= \frac{1}{\sqrt{2}}\left(\frac{\Omega_1}{\Omega}|a\rangle + |b\rangle + \frac{\Omega_2}{\Omega}|d\rangle\right), \\ |D_2\rangle &= -\frac{\Omega_2}{\Omega}|a\rangle + \frac{\Omega_1}{\Omega}|d\rangle, \\ |D_3\rangle &= \frac{1}{\sqrt{2}}\left(\frac{\Omega_1}{\Omega}|a\rangle - |b\rangle + \frac{\Omega_2}{\Omega}|d\rangle\right), \end{aligned} \qquad (2.19)$$

where $\Omega = \sqrt{\Omega_1^2 + \Omega_2^2}$, and their corresponding energies are given by

$$\begin{aligned} \mathcal{E}_1 &= \frac{\hbar\Omega}{2}, \\ \mathcal{E}_2 &= 0, \\ \mathcal{E}_3 &= -\frac{\hbar\Omega}{2}. \end{aligned} \tag{2.20}$$

When this system is probed to a fourth level as shown in Figure 2.11(c), one can see the appearance of the third peak predicted by Sandhya and Sharma [24] and the transparency windows predicted by Sadeghi *et al.* [25]. Wei *et al.* also predict the separation of $|D_1\rangle$ and $|D_3\rangle$ with increasing Ω_2, as indicated by (2.20) (see Figure 2.12). We obtain similar results for the case of a doubly-driven V system in Chapter 6.

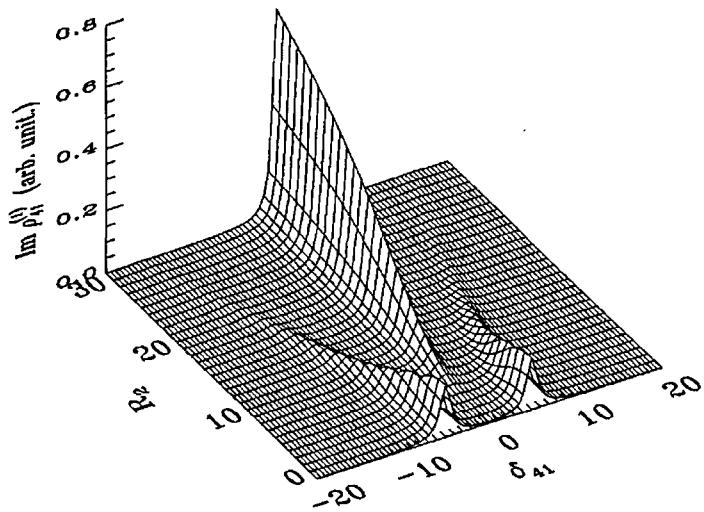

Figure 2.12 - Figure 2(a) of Wei *et al.* [26] showing probe absorption ($\mathrm{Im}\,\rho_{41}^{(1)}$) as a function of the Rabi frequency of C_2 (R_2) and probe field detuning (δ_{41}).

2.2.2 Single-photon switch

One possible application of the four-level systems described above, when taken down to the quantum limit, is the single-photon switch proposed by Harris and Yamamoto [9]. They studied the 4-level N system of Figure 2.13, coupled by two weak pulsed fields (P and C_2) and one strong cw field (C_1). It was demonstrated that it is possible to induce three-photon absorption or transmission of a single-photon P pulse

depending upon the simultaneous arrival or not of a single-photon C_2 pulse, respectively. Therefore, this system could be used as a P switch adiabatically controlled by the C_2 field. Since its action depends on the simultaneous arrival of photons, it may have application to the processing of quantum superposition states in the frame of quantum computing.

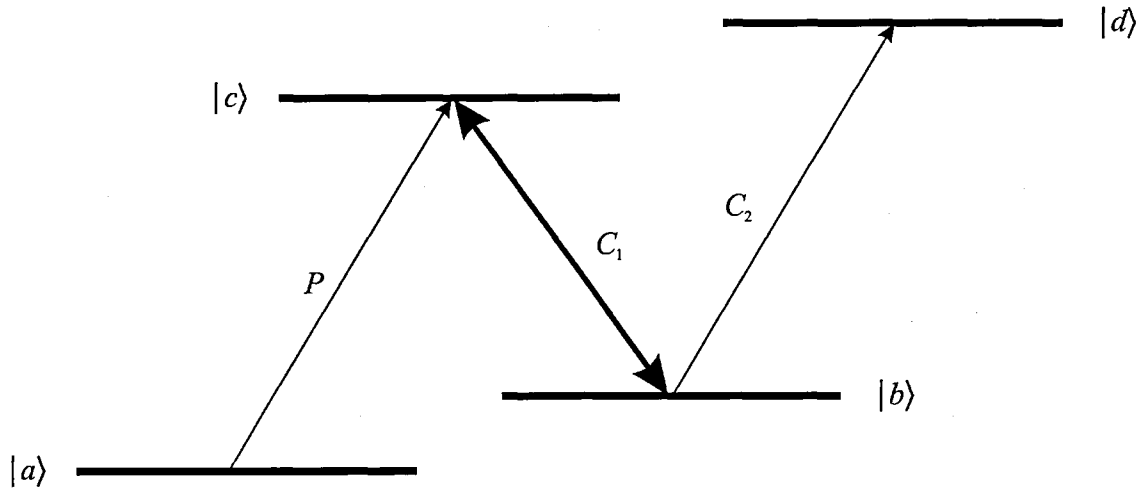

Figure 2.13 - Four-level N system proposed by Harris and Yamamoto [9] to produce a single-photon switch.

2.2.3 Photon blockade

Another possible application of the four-level systems is the photon blockade scheme proposed by Imamoğlu *et al.* in 1997 [1]. They proposed the inclusion of a four-level N system into a high finesse cavity, coupling two of its transitions (see Figure 2.14). The idea behind this scheme is that a coupling field C creates an EIT on the $|a\rangle - |c\rangle$ transition, such that a photon from the external field E can enter the cavity mode M. As a result the cavity doesn't exhibit one-photon atomic loss and, at the same time, an enhanced self-phase modulation is induced by the $|b\rangle - |d\rangle$ transition. This way, the arrival of a photon into the cavity will shift it out of resonance with the external field E and prevent another photon from getting into it, an effect known as photon blockade.

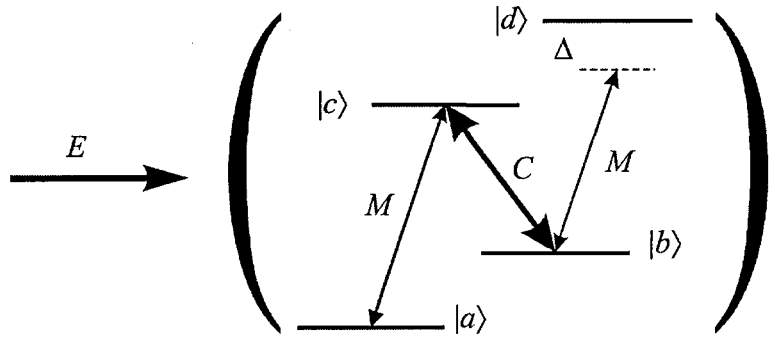

Figure 2.14 - Photon blockade scheme.

The theoretical study by Imamoğlu *et al.* [1] assumed that all atomic degrees of freedom could be adiabatically eliminated, but later studies by Grangier *et al.* [2] showed that the breakdown of this procedure in the high-dispersion limit leads to prohibitive restrictions on the parameters where photon blockade could be observed. However, later on it was suggested [3] that this problem could be overcome by using a single-atom system.

We have carried out a theoretical study of this system [4] in which we demonstrate that photon blockade is possible in multi-atom systems by the introduction of an extra detuning on state $|c\rangle$. By theoretically considering transitions on the ^{87}Rb D_2 line, we pointed out that strong photon blockade should be possible when the cavity resonance is tuned to the $|b\rangle - |d\rangle$ transition, despite a large mutual detuning δ between the cavity field and the strong classical coupling field (see Figure 2.15).

In fact, photon blockade occurs when it is possible to inject one photon in the cavity, but not two. We studied the possibility of injecting one and two photons in the cavity with one, two and three atoms by calculating the maximum populations of the one- and two-quantum atom-cavity dressed states [4], denoted by $\rho_{exc}^{(1)}$ and $\rho_{exc}^{(2)}$ respectively. The values of these populations were obtained by calculating the populations of the excited states of transitions $|L\rangle - |U\rangle$ between the $(j-1)$- and the j-quantum manifold, given by

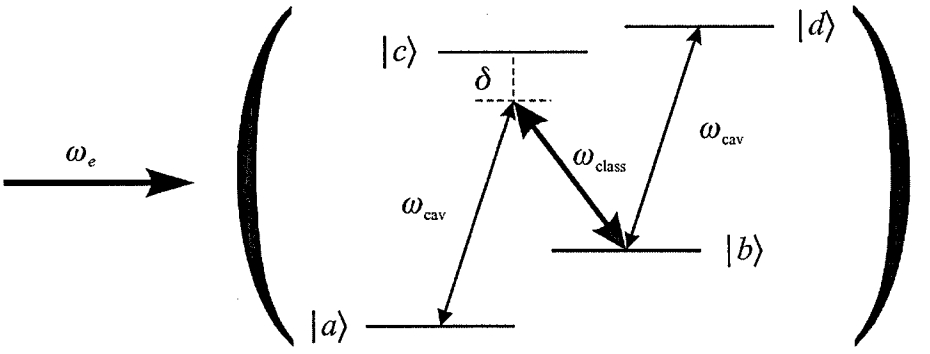

Figure 2.15 - Energy level diagram for the four-level N system. A strong classical coupling field with frequency ω_{class} is applied to the $|b\rangle-|c\rangle$ transition and detuned from it by an amount δ. The atoms are placed in a cavity with resonance frequency ω_{cav} which is detuned from the $|a\rangle-|c\rangle$ transition by δ and resonant with the $|b\rangle-|d\rangle$ transition. The cavity is driven resonantly by an external classical driving field with frequency ω_{cav}.

$$\rho_{exc} = \frac{\Omega_e^2}{2\Omega_e^2 + \Delta_e^2 + \Gamma_U^2}, \tag{2.21}$$

where Ω_e is the Rabi frequency of the external field, Δ_e the detuning of this field from a given transition, and Γ_U is the decay rate of the excited state $|U\rangle$. Then the maximum values $\rho_{exc}^{(j)}$ were drawn to plot the Figures to follow.

Figure 2.16 shows the maximum one-quantum dressed-state population $\rho_{exc}^{(1)}$ for different values of δ and the atom-cavity mode coupling g, when there is one atom in the cavity. The parameters used in this Figure were chosen to simulate an experiment in ^{87}Rb, i.e. $\Gamma_c/\Omega=\Gamma_d/\Omega=1.78$, $\Gamma_{cav}/\Omega=4$, $\delta_\omega/\Omega=660$, where Γ_c and Γ_d are the decay rates of states $|c\rangle$ and $|d\rangle$, Γ_{cav} is the decay rate of the cavity, and δ_ω is the separation between the two ground states $|a\rangle$ and $|b\rangle$. In Figure 2.16, $\rho_{exc}^{(1)}$ increases monotonically with g/Ω and, for the scale used, is independent of δ/Ω. The value of $\rho_{exc}^{(1)}$ is qualitatively very similar for one, two and three atoms, with the values of $\rho_{exc}^{(1)}$ slightly increasing as the number of atoms increases.

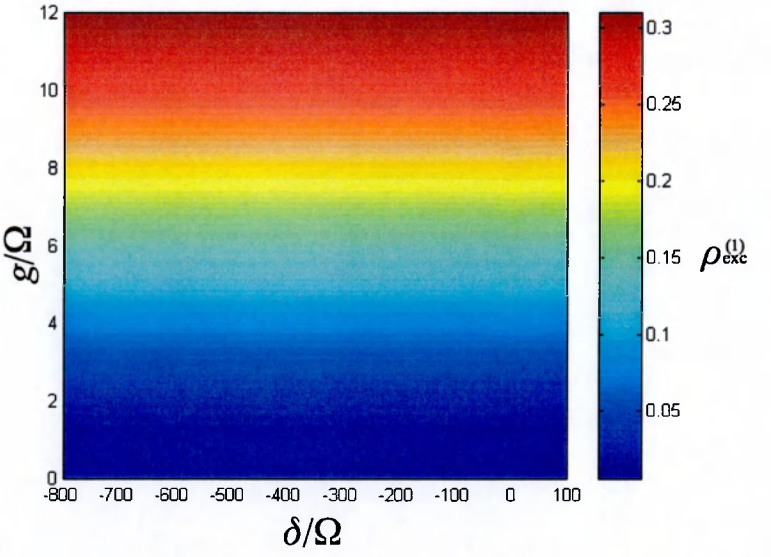

Figure 2.16 - Pseudocolour plot showing $\rho_{exc}^{(1)}$ as a function of detuning δ/Ω and the atom-cavity coupling g/Ω.

Figure 2.17 shows the maximum two-quantum dressed-state population $\rho_{exc}^{(2)}$ for different values of δ and the atom-cavity mode coupling g, when there is (a) one atom, (b) two atoms, and (c) three atoms in the cavity. The parameters used in this Figure were the same as used in Figure 2.16, although in Figure 2.17 we have explored the detuning δ in the vicinity of $\delta_\omega/\Omega=660$. The significance of this region is that when we have $\delta=-\delta_\omega$, the cavity becomes resonant with the $|b\rangle-|d\rangle$ transition. In Figure 2.17(a) we have seen generally small values for $\rho_{exc}^{(2)}$, indicating that photon blockade should be observable. With the exception of the 'shelf' for $g/\Omega\leq 1$, $\rho_{exc}^{(2)}$ decreases monotonically with g/Ω, indicating the effectiveness of photon blockade correspondingly increasing. This is expected, as a large g will give rise to a highly nonlinear system. Also note that $\rho_{exc}^{(2)}$ increases as $|\delta/\Omega|$ increases, indicating that the photon blockade is a resonance phenomenon. In Figure 2.17(b) and (c), we have observed a roughly triangular region of low $\rho_{exc}^{(2)}$, superimposed on the background of $\rho_{exc}^{(2)}$ noted in Figure 2.17(a). Values of $\rho_{exc}^{(2)}<0.01$ are present where $\rho_{exc}^{(1)}>0.35$ for

both the two- and three-atom cases. This suggests that the nonlinearity of the system is very large about this resonance.

We have also suggested that photon blockade should be observable using current state of the art technology, such as that of Hood *et al.* [71].

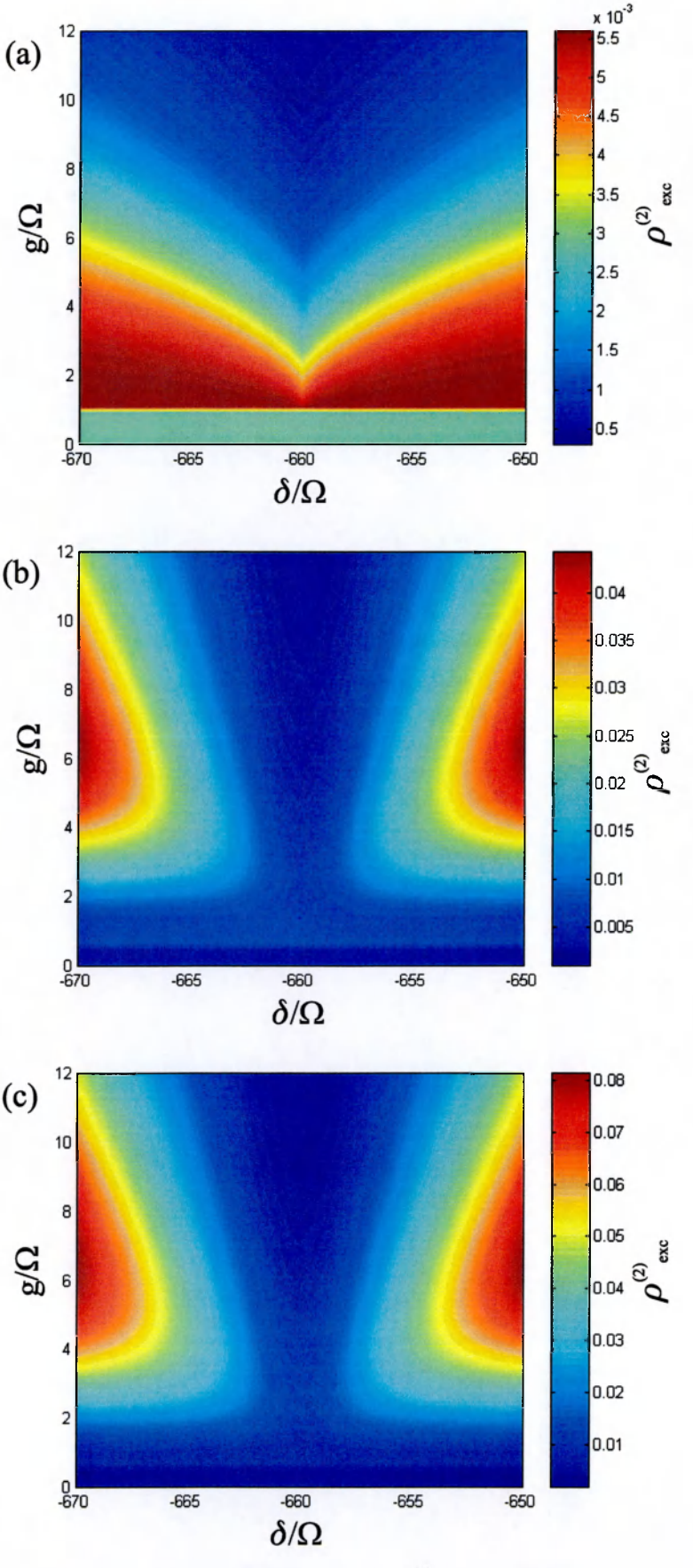

Figure 2.17 - Pseudo-colour plots of $\rho_{exc}^{(2)}$ in the vicinity of the resonance $\delta = -\delta_\omega$ for (a) one, (b) two and (c) three atoms.

Chapter 3

Optical Molasses and the Magneto-Optical Trap

In this Chapter we take a look at the mechanisms of laser cooling and trapping. This is not intended to be an exhaustive review, but an outline of the main points. Reviews on this field can be found in [72-74]. The following Sections give an overview of optical molasses and the MOT detailing aspects pertinent to this thesis. Section 3.1 starts with a historical overview of the field, then Sections 3.2 and 3.3 briefly outline the mechanisms of laser cooling in an optical molasses and laser trapping in an MOT, respectively.

3.1 Historical background

In 1982, the first stopping of a thermal beam by Philips and Metcalf [75] marked the beginning of a new era in the field of atomic spectroscopy. It set the path towards

the creation of the first optical molasses by Chu *et al.* in 1985 [76], and later on in 1987, the first magneto-optical trap (MOT) was constructed by Raab *et al.* [77]. These three experimental achievements permitted the cooling and trapping of neutral atoms below millikelvin temperatures and with densities of nearly 10^{12} atoms/cm^3. All this meant that the atoms could be confined in a relatively perturbation-free environment, where Doppler shifts are much less than spontaneous linewidths and very long atom-laser interaction times are possible.

At that time, the lowest temperature to which it was thought that atoms could be cooled was the equilibrium temperature that results from the balance between the momentum diffusion and cooling processes in the trap, known as the Doppler temperature. However, the first temperature measurements of trapped atoms revealed that this was not the case, but that in fact these temperatures were below the Doppler temperature [78]. One year later, in 1989, Dalibard and Cohen-Tannoudji [79] and Ungar *et al.* [80] attributed this fact to the multi-level character of the atoms and the spatial variations of the polarisation of the light field. These cooling processes, known as sub-Doppler cooling, allowed the temperatures to go down to 10^{-5} K, reaching a new limit: the one corresponding to the energy of a photon recoil. Nevertheless, this recoil limit was breached as well by a process known as sub-recoil cooling [81], which allowed temperatures below 10^{-6} K [82].

In 1997, Chu, Phillips and Cohen-Tannoudji were awarded the Nobel Prize in Physics [83] for their contribution to the cooling and trapping of atoms. Optical molasses and the MOT have now become common laboratory tools and are widely used for various applications. These range from very practical, e.g. caesium atomic clocks for time standards [84], to very fundamental ones, e.g. preparation of Bose-Einstein

condensates [85]. In our case, we use an MOT as a means to prepare a Doppler-free sample to study transient EIT and coherence effects in four-level systems.

3.2 Optical molasses

The concept of optical molasses was first introduced by Hänsch and Schawlow in 1974 [86] and first realised by Chu *et al.* in 1985 [76]. Essentially, it is an arrangement of intersecting beams that produces a region where neutral atoms experience a viscous force that slows them down, and hence lowers their temperature. The term *optical molasses* was adopted by analogy between this viscous region and real molasses.

Figure 3.1 shows an optical molasses arrangement, where six weak ($\Gamma \geq \Omega$) counter-propagating beams in all three dimensions of space intersect to form the viscous region. The intersection occurs inside a vacuum chamber containing a species of neutral atoms, which could come, for example, from an atomic beam, a vapour cell or getters. The beams are red-detuned from a chosen transition in these atoms, so that atoms travelling with velocity components against one of the beams, see the wavelength of the beam blue-shifted towards resonance, but those travelling with velocity components in the same direction, see the wavelength of the beam shifted further towards the red. This way, the atoms preferentially absorb the beams travelling against them, i.e. photons with opposite momentum. This momentum is absorbed by the atoms, which slow down as a result. Although each photon absorbed is re-emitted by the atom, which gains momentum again, the emission occurs in a random direction, and after many photon scatterings the momentum gained by the atom is averaged out. However, this photon emission process limits the lowest temperature the sample can reach by the cooling process.

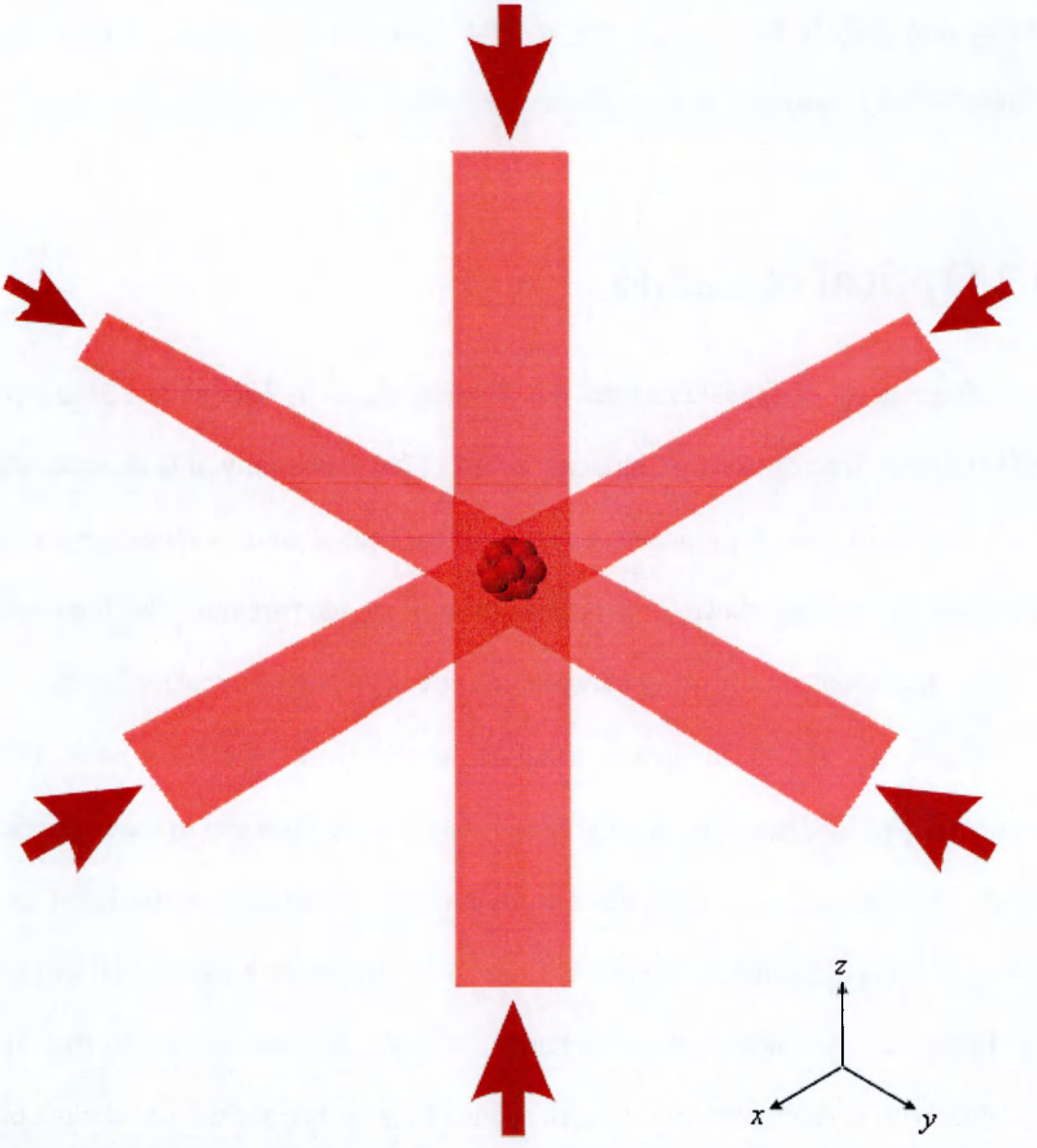

Figure 3.1 - Optical molasses set-up.

To give an idea of the scales involved in optical molasses, Table 3.1 lists some typical values for its parameters.

Table 3.1 - Typical optical molasses parameters for Rb.

Cloud and beam diameter	5 to 10 mm
Temperature	20 to 200 μK
Number of atoms in cloud	10^4 to 10^7
Atom number density	10^6 to 10^{10} cm^{-3}
Capture velocity	~8 m/s
RMS velocity in cloud	6 to 20 cm/s
Absorption cycles to stop atom	$\leq 10^5$
Stopping time	≤ 1 ms

3.2.1 Cooling forces

To further elucidate the mechanisms of laser cooling, we consider a two-level atom moving along the z-axis immersed in a pair of weak counter-propagating beams detuned from the atomic transition by an amount Δ_T, i.e. 1-D molasses. Due to the Doppler effect, the probability of the atom absorbing a photon depends on the atom's velocity, i.e. an atom travelling faster against one of the beams sees the photons shifted further into resonance than one going slower. However if an atom is travelling too fast, the Doppler shift will exceed that required for resonance and the photon will be blue detuned, resulting in a decreasing absorption probability. Similarly, if an atom is travelling in the same direction as one of the beams, the Doppler shift will take the laser field further out of resonance. Quantitatively, an atom moving at a velocity v_z in a 1-D molasses experiences a force [72]

$$F_z = \frac{\hbar k\Gamma}{2}\left[\frac{I/I_{\text{sat}}}{1+4(\Delta_T - kv_z)^2/\Gamma^2 + 2I/I_{\text{sat}}} - \frac{I/I_{\text{sat}}}{1+4(\Delta_T + kv_z)^2/\Gamma^2 + 2I/I_{\text{sat}}}\right], \tag{3.1}$$

where I and k are the intensity and the wave number of the beams, I_{sat} is the saturation intensity and $I_{\text{sat}} \gg I$. Γ is the natural linewidth or spontaneous decay rate.

Now consider a 3-D molasses. At low velocities ($|\mathbf{k}\cdot\mathbf{v}| < |\Delta_T|$, where $\mathbf{k}$ is the wave vector of the beam and $\mathbf{v}$ the atom velocity), the total force due to each of the three beam pairs becomes linear with velocity, resulting in a viscous force of the form

$$\mathbf{F} = -\beta\mathbf{v}, \tag{3.2}$$

where

$$\beta = -4\hbar k^2 \frac{I}{I_{\text{sat}}} \frac{2\Delta_T/\Gamma}{\left[1+4\Delta_T^2/\Gamma^2 + 2I/I_{\text{sat}}\right]^2} \tag{3.3}$$

is the friction coefficient.

3.2.2 Momentum diffusion and the Doppler temperature

So far we have considered the cooling forces acting on the atoms, but as stated before, there is a minimum temperature to which atoms can be cooled by the above process: the Doppler temperature. Hence, there must be an opposing process to the cooling force. This heating process originates from the fact that the scattering of cooling photons occurs in a random fashion, which causes the light force to fluctuate about a mean value. As a result, the momentum distribution of the atoms spreads. This process is known as momentum diffusion.

The process of momentum diffusion in optical molasses is very similar to that of a particle in a viscous fluid, where a particle is slowed down until its kinetic energy is of the order of the thermal energy. This particle then undergoes Brownian motion, where its mean momentum $\langle \mathbf{p} \rangle$ is zero and the variance of its momentum $\langle p^2 \rangle$ increases, or diffuses, with time at a rate

$$\frac{d\langle p^2 \rangle}{dt} = 2D_p, \tag{3.4}$$

where D_p is known as the momentum diffusion coefficient, and for a 3-D Brownian motion [72,73,87]

$$D_p = 3\hbar^2 k^2 \frac{I}{I_{\text{sat}}} \frac{\Gamma}{1+4\Delta_T^2/\Gamma^2 + 2I/I_{\text{sat}}}. \tag{3.5}$$

Although $\langle p^2 \rangle$ tends to increase indefinitely, this tendency is counterbalanced by the friction force, resulting in an equilibrium temperature of

$$k_B T = \frac{D_p}{3\beta} = -\frac{\hbar\Gamma}{4}\left[\frac{2\Delta_T}{\Gamma} + \frac{\Gamma}{2\Delta_T}\left(1+2\frac{I}{I_{\text{sat}}}\right)\right], \tag{3.6}$$

where k_B is the Boltzmann's constant. Therefore, for $I \ll I_{sat}$ the minimum temperature to which an optical molasses can be cooled (the Doppler temperature) is reached when $\Delta_T = -\Gamma/2$ and is

$$T_D = \frac{\hbar\Gamma}{2k_B}. \tag{3.7}$$

For the D_2 line in Rb, $T_D = 142$ μK.

There have been several different more precise analyses of the diffusion coefficient [88], taking into account quantum-mechanical fluctuations of the radiation force. However, these analyses are beyond the scope of this thesis and will not be detailed here.

3.2.3 Sub-Doppler cooling

Although the Doppler theory predicted a limit temperature, an experiment by Lett *et al.* in 1988 [78] reported temperatures in an optical molasses significantly below that limit. Following experiments also reported temperatures lower than the Doppler temperature, which sparked a new theoretical approach to laser cooling [79,80]. This new approach took into account the multi-level nature of the atom and the polarisation of the cooling beams.

There are several sub-Doppler cooling mechanisms, such as Sisyphus cooling, corkscrew cooling, evaporative cooling, etc. The most important in our case are Sisyphus and corkscrew cooling, which are more fully described in [79]. Here, we briefly describe the main ideas.

Sisyphus cooling

A good qualitative analysis of the effect is presented in [89]. Consider the $J=1/2 \rightarrow J'=3/2$ transition of the multi-level atom shown in Figure 3.2(a), immersed in

a 1-D optical molasses formed by two counterpropagating beams of orthogonal linear polarisations ($\pi\sigma$). The beams form a standing wave of spatially varying polarisation, as shown in Figure 3.2(b). This variation of the polarisation produces a spatial variation of the light shifts on the ground states as the Clebsch-Gordan coefficients differ for different polarisations (see Figure 3.2(c)). If an atom starts at $z=\lambda/8$, moving towards positive z and in the ground state $m_J=+1/2$, it will start climbing the energy potential hill at the expense of its kinetic energy. Once it has passed $z=\lambda/4$ the energy of the $m_J=-1/2$ ground state becomes lower and the atom is likely to be optically pumped into that state by the σ^- light, losing the excess energy to the light field. The atom will then start climbing the hill again only to be optically pumped back down into $m_J=+1/2$ by the σ^+ light after it passes $z=\lambda/2$. This process has a cooling effect, as the atoms are slowed down when they climb the hill, and is known as Sisyphus cooling after the Greek myth of Sisyphus, who was forever condemned by the Gods to push a rock up a hill, only to find it slide back down again.

The Sisyphus effect is only effective for atoms moving slowly enough to give enough time for the optical pumping to take effect while the atom is up the potential hill. Hence a critical velocity v_S is defined as a distance of $\sim\lambda/4$ travelled in an optical pumping time τ_p, i.e. $v_S=1/2k\tau_p$. Atoms travelling faster than this velocity will not be affected by Sisyphus cooling, so atoms in an optical molasses will first be slowed down by Doppler cooling and then, when $v\approx v_S$, by Sisyphus cooling.

A quantitative 1-D analysis [79] of this system yields a polarisation gradient cooling force in the z direction, spatially averaged over a wavelength,

$$F_z = -\frac{\beta_S v_z}{1+(v_z/v_S)^2}, \tag{3.8}$$

where the Sisyphus friction coefficient is given by

$$\beta_S = -3\hbar k^2 \frac{\Delta_T}{\Gamma}, \tag{3.9}$$

and the critical velocity by

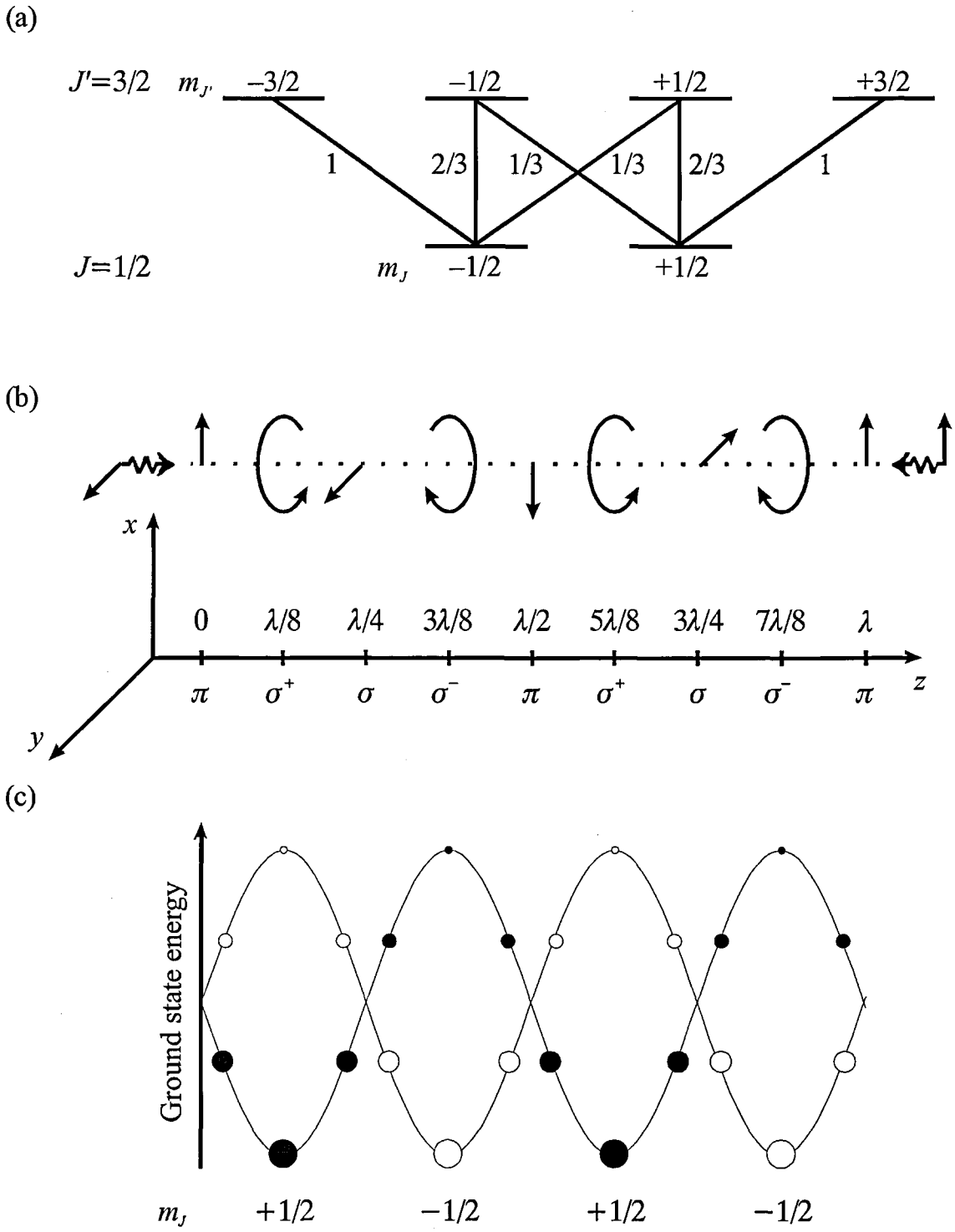

Figure 3.2 - The Sisyphus effect. (a) Multi-level atom. (b) Standing wave pattern. (c) Ground state energy light shifts.

$$kv_S = \frac{1}{2\tau_p} = \frac{\Gamma}{9}\frac{I/I_{sat}}{4(\Delta_T/\Gamma)^2 + 1}. \tag{3.10}$$

Notice that the friction coefficient here is proportional to the detuning, and the capture velocity to the intensity, contrary to Doppler cooling, where β is proportional to the intensity and the capture velocity to the detuning.

The spatially averaged momentum diffusion coefficient for $|\Delta_T| \gg \Gamma$ is given by [79]

$$D_p^S \approx \frac{3\hbar^2 k^2 \Gamma}{4}\frac{I}{I_{sat}}, \tag{3.11}$$

and hence, the equilibrium sub-Doppler temperature is

$$k_B T = \frac{D_p^S}{\beta_S} \approx \frac{\hbar\Gamma^2}{4|\Delta_T|}\frac{I}{I_{sat}}. \tag{3.12}$$

The above equation shows that the minimum kinetic energy is approximately equal to the light shift ($\propto \Omega^2/\Delta$) of the level involved. It also suggests that the temperature can be made as low as desired by lowering the intensity of the cooling beams or increasing their detuning. However, this is not the case, because this analysis breaks down when the atomic momentum becomes comparable to the atomic recoil due to the absorption or emission of a photon. A full quantum treatment of the centre of mass motion is then needed [90].

Corkscrew cooling

In a 1-D molasses with two counterpropagating circularly polarised σ^+ and σ^- beams, the laser fields form a standing wave pattern known as the corkscrew standing wave. The resulting polarisation is linear all along the standing wave, but the orientation of the polarisation vector rotates axially, so that the tip of the vector traces out a helix with pitch λ.

Although the results are qualitatively similar to the Sisyphus $\pi\sigma$ case, the analysis of the configuration is more difficult than the above $\pi\sigma$ configuration, depending on a redistribution of populations of the ground states known as *orientation* [79]. To summarise, corkscrew cooling can be described by the friction coefficient and temperature [79]

$$\begin{aligned} \beta_C &\propto -\frac{\Delta_T}{\Gamma}, \\ k_B T &\propto \frac{I}{|\Delta_T|}. \end{aligned} \tag{3.13}$$

For large detuning, this result is very similar to the one obtained above for $\pi\sigma$ polarisation. Another similarity is the possibility of reducing the temperature arbitrarily, but in the same way, this analysis breaks down when the atomic momentum becomes comparable to the atomic recoil due to the absorption or emission of a photon.

It is interesting to compare Sisyphus cooling and corkscrew cooling. Both the friction and the diffusion coefficients of Sisyphus cooling are a factor $\sim \Delta_T^2/\Gamma^2$ different than their corkscrew counterparts, but because the equilibrium temperature depends on their ratio, this temperature is of the same order for both mechanisms. One fundamental difference however, is the fact that Sisyphus cooling relies on the dipole force, whereas corkscrew cooling relies on the scattering force.

Atoms can be cooled in an optical molasses by the above processes, but this is not always the ideal since atoms cannot be confined by optical molasses. This is because there is only a velocity damping force, and atoms travelling at small but finite velocities can still diffuse out of the molasses. Therefore, reloading is necessary from an atomic beam or background vapour. Attempts to solve this problem led to the invention of different kinds of traps where the atoms can be confined. These can be classified as:

optical dipole traps [91], magnetic traps [92], and magneto-optical traps [77,93]. Because of its importance to our experiments, we describe the last named in the Section below.

3.3 The magneto-optical trap

The first magneto-optical trap (MOT) was realised by Raab *et al.* in 1987 [77], although the original idea is credited to J. Dalibard in this paper. It came after Pritchard *et al.* had demonstrated in 1986 [93] that, despite the optical Earnshaw theorem [94], trapping by scattering forces was possible if some external field was applied.

The idea was to use circularly polarised light for an optical molasses and add an external quadrupole magnetic field produced by a pair of anti-Helmholtz coils centred with the cooling beams (see Figure 3.3), so that an atom moving away from the magnetic field centre would be Zeeman shifted towards resonance with the opposing cooling beam, which slows it down and pushes it back towards the centre (see Figure 3.4).

Table 3.2 below lists some typical MOT parameters, which will be described in the following Sections.

Table 3.2 - Typical MOT parameters for Rb.

Cloud diameter	0.1 to 10 mm
Temperature	10 to 200 μK
Number of atoms in cloud	10^4 to 10^{10}
Atom number density	10^8 to 10^{11} cm^{-3}
Capture velocity	5 to 25 m/s
Potential well depth	~0.5 K
Beam diameter	3 to 20 mm

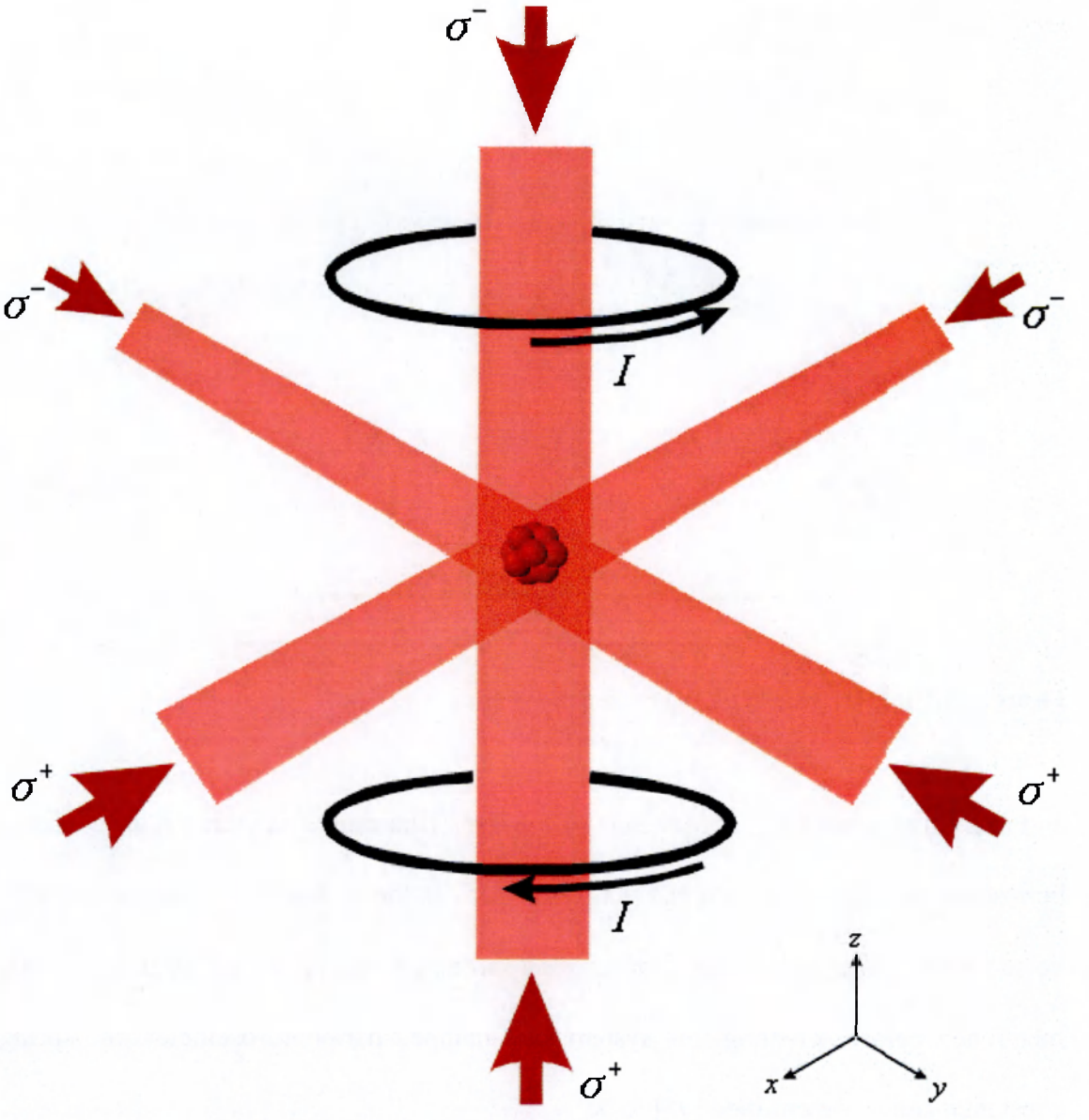

Figure 3.3 - The magneto-optical trap set-up.

3.3.1 Trapping forces in an MOT

Figure 3.4 shows the MOT's trapping mechanism in 1-D for a $J=0 \rightarrow J'=1$ transition in an atom. The cooling lasers are red-detuned from the transition, as in an optical molasses, but here the excited levels are brought into resonance by the quadrupole magnetic field as the distance from the centre increases. In fact, the magnetic field **B** on the z-axis is of the form $B_z(z)=bz$ near the centre of the trap, where b is a positive constant, and hence the Zeeman $m=\pm 1$ sub-levels are shifted towards

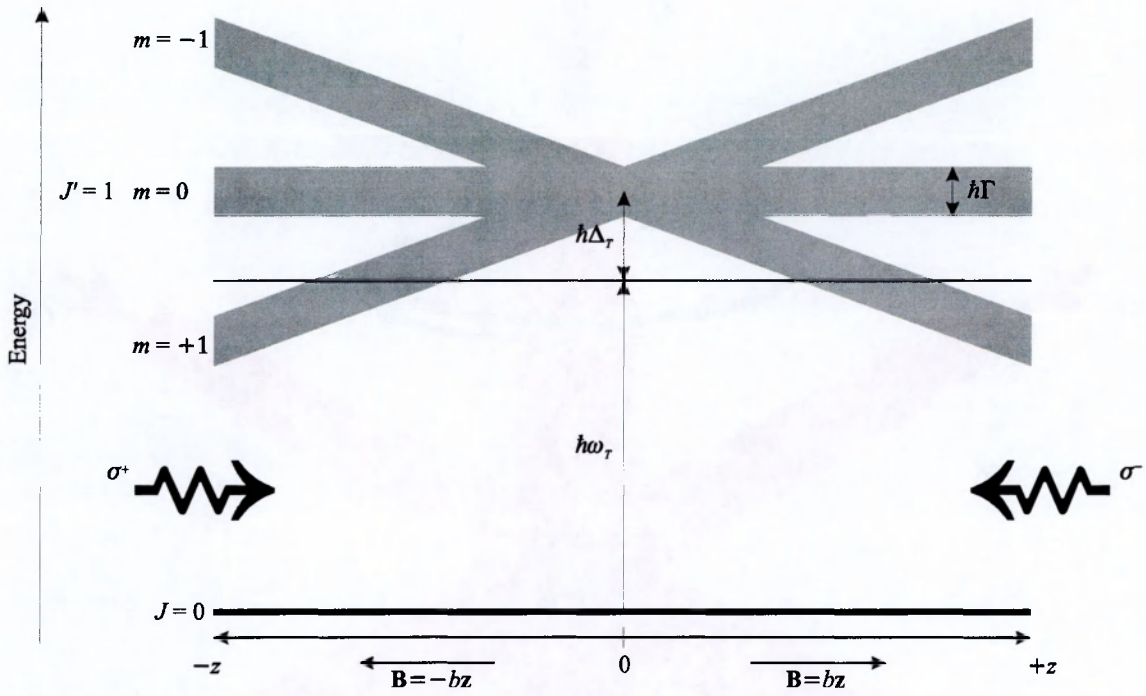

Figure 3.4 - 1-D MOT's trapping and cooling mechanism.

and away from resonance at each side of the trap. This causes an atom on the z-axis to be resonant with the σ^+ beam and non-resonant with the σ^- beam on one side and vice versa on the other, giving rise to a restoring force $F_z = -\kappa z$ on top of the friction force mentioned before. Treating this system as a damped harmonic oscillator, the spring constant κ can be determined [95] to be

$$\kappa = \frac{g_e \mu_B b \beta_C}{\hbar k}, \tag{3.14}$$

where g_e is the g-factor of the excited state and μ_B is the Bohr magneton. The total force acting on an atom on the z-axis is therefore

$$F_z = -\beta_C v_z - \kappa z. \tag{3.15}$$

It is interesting to note that, in practice, the ratio between β_C and κ is such that the motion is overdamped.

The more general 3-D force could be approximated by adding the forces in each of the three orthogonal directions. However, the quadrupole magnetic field is not

spherically symmetric (it is stronger in the axis of the coils) and so the spring constant should be regarded as a tensor for a complete mathematical treatment.

This force can also be generalised to transitions $J \rightarrow J+1$ where $J>0$. The difference is that more ground and excited states have to be taken into account, and κ will depend on their different g-factors and the population distribution among the Zeeman sub-levels due to optical pumping.

3.3.2 Loading and loss rates

The total number N of atoms trapped in an MOT loaded from a background vapour depends on the loading and loss rates experienced by the atoms in the trap and is determined by [95]

$$\frac{dN}{dt} = R - \frac{N}{\tau} - \xi_c N^2, \tag{3.16}$$

where R is the loading rate, τ is the lifetime of the trapped atoms due to background atom collisions, and ξ_c is the parameter characterising the intra-trap collision rate.

The rate R at which atoms are trapped can be calculated from the kinetic theory of gases. Atoms with a velocity slower than the capture velocity v_c enter the trapping volume V at a rate [96]

$$R = \frac{\eta_b V^{2/3} v_c^4}{2 v_p^3}, \tag{3.17}$$

where η_b is the density of the background vapour and $v_p = \sqrt{2k_B T_b / m}$ is the most probable velocity of the atoms in the background vapour at temperature T_b (according to the Maxwell-Boltzmann distribution). The capture velocity is defined as [95] $v_c=(2ar_m)^{1/2}$, where a is the molasses deceleration and r_m its radius.

If we now consider that intra-trap collisions may be ignored ($\xi_c N^2 \ll N/\tau$), the rate at which atoms are lost due to collisions with background atoms is $N/\tau = N\sigma\eta_b\bar{v}$, where σ

is the cross-section of this kind of collisions and $\bar{v}=\sqrt{8k_{\mathrm{B}}T_b/\pi m}$ is the mean velocity of the background atoms. The trap lifetime against these collisions can be expressed as

$$\tau=\frac{\sqrt{2\pi m k_{\mathrm{B}}T_b}}{4\sigma P_b}, \tag{3.18}$$

where $P_b=\eta_b k_{\mathrm{B}}T_b$ is the pressure of the background atoms. Solving (3.16) for the steady state, we find

$$N(t\to\infty)=R\tau=\frac{\pi^{1/2}V^{2/3}}{4\sigma}\left(\frac{v_c}{v_p}\right)^4. \tag{3.19}$$

Given that $v_c\propto r_m^{1/2}$ and $V\propto r_m^3$, we see that $N\propto r_m^4$ and is not dependent on η_b. This means that to trap the largest number of atoms, one has to expand the beams as much as possible, providing there is sufficient power to keep the trapping transition near saturation and the intra-trap loss rate remains negligible.

As the number of atoms in the trap increases the effects of intra-trap collisions start to emerge and (3.19) losses validity. In this case, (3.16) can be solved for the initial condition $N(0)=0$ to give in the steady state

$$N(t\to\infty)=\frac{1}{2\xi_c\tau}\left(\sqrt{1+4\xi_c R\tau^2}-1\right) \tag{3.20}$$

Intra-trap collisions are divided into three main types: fine-structure changing collisions, radiative redistribution collisions, and hyperfine changing collisions. The study of intra-trap collisions is beyond the scope of this thesis and the reader is pointed to the references listed in [97] for information in this field. In the MOTs described in this thesis (see Chapter 4), intra-trap collisions can be neglected due to the relatively low atomic densities, detunings and intensities we worked at.

3.3.3 Sub-Doppler cooling in an MOT

Both Sisyphus and corkscrew cooling take place in an MOT due to the complex 3-D standing wave pattern generated by the circularly polarised beams (see [87,98] for a full description). However, the presence of the magnetic field has a detrimental effect on these cooling mechanisms. Sisyphus cooling can be destroyed if the Zeeman shifts induced by the magnetic field are as large as the light shifts in Figure 3.2(c). In the case of corkscrew cooling, the detrimental effect is due to the competition between Larmor precession and the alignment of the atomic dipole caused by optical pumping.

However, because the atoms are trapped near the zero-field point, it is possible to achieve sub-Doppler cooling in a sufficiently small trap [99]. For large magnetic fields, it can be shown [79,100] that corkscrew cooling is still active in a frame moving with the atoms with velocity $v_s = -g_g \mu_B b/\hbar k$, where g_g is the g-factor of the ground state.

Generally an MOT is a very complex environment. In addition to the various cooling and trapping mechanisms described above, the atoms are subject to light forces due to the multiple scattering of fluorescence photons, which have a strong influence on the size of the sample, the atomic states occupied and the atomic densities [95,101].

Chapter 4

Development of Laser Systems and MOT

We now turn our attention to the work carried out at The Open University during the Author's studentship (1st October 1998 to 31st December 2001), starting with the development of various aspects of the experimental apparatus.

A full description of the state of the experiment in September 1998 can be found in H. Chen's thesis [8] and in S. A. Hopkins' thesis [87], and is outlined briefly in Section 4.1. Much development of the laser systems, the trap optics and the data acquisition and computer control system has been done since then and this is described in Sections 4.2 to 4.4. This developed system is the one used for the experiments described in Chapters 5 and 6. Finally, a new "second-generation" MOT has been built and is described in Section 4.6.

4.1 State of experiment in September 1998

4.1.1 The diode lasers

The lasers used in the previous experiments [7,8,45,87] were Sharp LT024MD and LT025MD, with nominal output powers of 30 mW and 40 mW respectively. Some of them were used in grating-controlled external-cavity diode laser systems (ECDL) working at 780 nm. The external cavity was formed by a grating in the Littrow configuration [102] and controlled by a piezo-electric transducer (PZT). This allows line narrowing and wavelength tuning of the laser. Further, a collimating lens and a beamsplitter were placed between the laser and the grating to produce a collimated beam and two outputs, respectively. One of the outputs was sent through an optical isolator and used for experimental purposes, while the other was used for monitoring and locking the wavelength of the laser. The monitoring was done via saturated absorption [103]. The locking was done via electronic feedback of the processed saturated absorption signal, and allowed the laser to be locked on any of the slopes of the saturated absorption signal. The circuit used for this locking mechanism was based on a design from McAdam *et al.* [104] and built in the O.U. Electronics Workshop. This kind of laser system has a very narrow linewidth (<800 kHz) and a very stable wavelength (when locked), but gives a very low output power (≈2.5 mW) compared to the nominal one for the bare diode because of the losses in the external cavity and the monitoring output.

The other laser used was a slave diode laser injected by an ECDL. This laser consisted only of a 40 mW laser diode and a collimating lens. The injection was done through a double-passed acousto-optic modulator (AOM) (see [87] for more information) and through an isolator placed in front of the laser. The AOM allowed the

wavelength of the laser to be shifted from the locked ECDL's wavelength, hence giving freedom of where to lock and the possibility to scan over a small range of wavelengths. The wavelength of this laser was monitored via saturated absorption using a fraction of light taken from the output. This kind of laser has a high output power (≈40 mW) and very broad linewidth (≈80 MHz) on its own, but exhibits the same characteristics as the ECDL when injected, while maintaining its output power.

All laser systems were temperature controlled for wavelength selection and stability. This was done by a Peltier cell and a thermistor placed near the diode lasers and connected to a temperature controller built by the Electronics Workshop (job No. 1559). The lasers were driven by current drivers, also built by the Electronics Workshop (job No. 1559).

Three ECDL were used during the past EIT experiments [7,8,45]: one as probe, one as coupling and repumping, and another for injecting the slave laser. The slave was used to produce the trapping beams for the MOT.

4.1.2 The first-generation MOT

The "first-generation" MOT was used during the past experiments and during the experiments described in Chapters 5 and 6 (with a few modifications; see Section 4.3), until the development of the "second-generation" MOT (see Section 4.6). It was made of a custom-made blown glass cell (see Figure 4.1) which has two small windows at the top and bottom, two small intruding lateral windows and two large front and back windows. The top and bottom windows are 20 mm in diameter, but only 10-mm beams can be used due to the distortions caused by the blowing of the cell. The two intruding lateral windows are 25 mm in diameter, but they hold the magnetic coils and present the same distortions as the top and bottom windows, hence only 10-mm beams can be used. The large front and back windows are 100 mm wide allowing good access to the centre

of the cell where the atoms are trapped. However, the intruding windows limit this access to a beam of maximum diameter of 20 mm and to a maximum horizontal clear aperture of 38°. The flatness of all the windows was measured by S. A. Hopkins [87] to be better than 2λ per cm in the central regions at the desired wavelength (λ=780 nm).

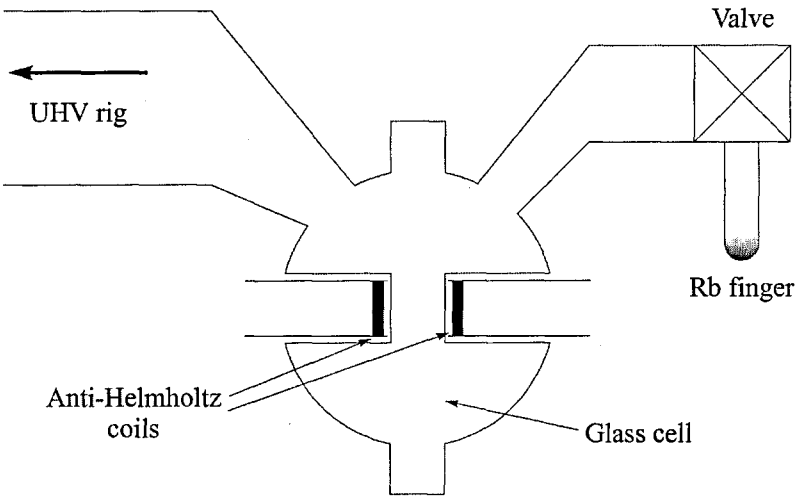

Figure 4.1 – Schematic of the MOT glass cell.

The anti-Helmholtz coils, which provide the magnetic field gradient to trap the atoms, were wound inside the intruding windows using 0.8 mm^2 enamel-coated copper wire (see Figure 4.2). The coils consist of 4 turns of radius 10.5 mm with a minimum separation of 23 mm and a maximum of 31 mm, producing a magnetic field gradient of 1.57 G $cm^{-1}A^{-1}$ (note that the value in [8] and [87] is incorrect). The current is supplied by a computer-controlled current driver made by the O.U. Electronics Workshop (job No. 1606), which can supply a maximum of 10 A, producing a maximum field gradient $\partial B_z/\partial z$=15.7 G/cm. The cell resides inside three orthogonal Helmholtz coil pairs, which nullify the stray magnetic fields caused by magnetised metals and the Earth's magnetic field. The supply for these coils was also built by the Electronics Workshop (job No. 1607).

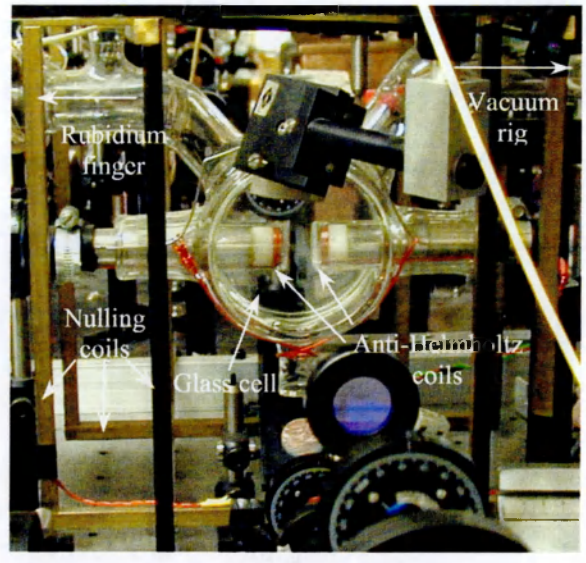

Figure 4.2 - The first-generation MOT.

A CCD camera and a calibrated photodiode are used to monitor the cloud of trapped atoms. The scattered light from the cloud of cold atoms is collected by a lens and focused on the CCD, which can acquire still images and live video of the cloud. A beamsplitter placed in front of the camera splits some of the light towards the calibrated photodiode, which is used to measure the number of atoms from the amount of light scattered. The calibration used is 1 mV$\approx 3\times10^{6}$ atoms trapped, which was obtained by S. A. Hopkins [87].

The cell is fixed on one side to the vacuum rig and held (but not fixed) on the other side by a harness. This is to minimise any mechanical stress on the cell, which may break it. However, this means that any manipulation of the vacuum valves causes the cell to wobble and change its position slightly, misaligning the anti-Helmholtz coils with respect to the trapping laser beams. This has proven to be a minor inconvenience in our experiments and meant that the trap conditions varied slightly from day to day.

4.1.3 The vacuum system

The glass cell is connected on one end to a rubidium finger and on the other end to an ultra-high vacuum (UHV) rig. Both connections are made through UHV valves to

allow access to and isolation of the cell. The UHV rig consists of an ion gauge and a 150 l/s diffusion pump backed by a rotary pump, which achieved a background pressure of 2×10^{-9} torr in our system. The Rb finger UHV valve could be opened to produce working Rb pressures around 5×10^{-8} torr in the cell. The pressure is monitored by an ion gauge connected through a UHV valve to the output port of the diffusion pump.

4.2 Development of the laser systems

During the course of the Author's studentship, the laser systems described in Section 4.1 have been upgraded to more powerful and reliable systems, and new master-slave systems have been built to make the most of the power available. We have also set-up a new laser system at 795 nm, which was built at Imperial College. These new systems were used in the experiments reported in Chapters 5 and 6 of this thesis.

4.2.1 Upgrade of the laser systems

The Sharp LT024MD and LT025MD diode lasers have been replaced by more powerful Sanyo DL-7140-201 diode lasers. These lasers have a nominal output power of 70 mW, which is more than double the power of the old Sharp lasers. Table 4.1 shows a comparison between the characteristics of the Sharp and Sanyo diode lasers. Apart from optical power, another important difference is the lasing wavelength of the diodes, as we require the lasers to be tuned to the rubidium D_2 line at 780 nm. This means that the Sanyo diode lasers have to be cooled a bit further than the Sharp ones. However, the wavelengths quoted in Table 4.1 are typical values, and the diodes are produced with a range of wavelengths, so it is possible to select the ones closer to 780 nm. Another noticeable difference is the beam divergence; i.e. the Sanyo diode

lasers exhibit a less divergent beam than the Sharp lasers, which results in a smaller beam diameter after the collimating lens.

Table 4.1 - Sharp and Sanyo diode lasers typical characteristics.

Parameter		Sharp LT024MD/LT025MD	Sanyo DL-7140-201
Optical output power[1]		30/40 mW	70 mW
Threshold current		55/70 mA	30 mA
Operation current		85/110 mA	100 mA
Lasing wavelength		780 nm	785 nm
Beam[2] divergence	Perpendicular	29°/26°	17°
	Parallel	10°/9.5°	8°

1 Continuous wave.
2 Full width half maximum.

Another modification to the laser systems has been the replacement of the collimating lens and holder by a collimating tube. The holders used for the collimating lenses became loose due to their springs becoming weak. This let the collimating lens move with any vibration with respect to the laser, making the beam change alignment. The use of the collimating tube allowed this problem to be solved because both lens and laser are held inside the same tube and their separation is controlled by a screw thread. The collimating tubes used were Thorlabs LT110P-B and LT230P-B, which produce an elliptical collimated beam of 2×4 mm and 1×2 mm respectively, using the Sanyo diode lasers.

Finally, we have also replaced the housings of the laser systems by more accessible and modular ones. Each of the old systems was fixed inside an aluminium box with a top lid and holes drilled on the sides for the beams to come out. It was difficult to reach the screws to align the grating or replace the laser in this set-up. Another problem was the fact that there were no connectors on the boxes, i.e. the cables were soldered to the different components of the system: the Peltier cell, the thermistor and the piezo. This made it difficult to change any individual component in case of break down and to change the cables connecting them to the instruments. Therefore, we

have replaced the housings by a horizontal aluminium platform with connectors and a box that can be screwed onto it to cover the system, with holes for the output beams to come out (see Figure 4.3). This new set-up makes it easier to change the different parts of the system in case of break down. It is also more modular in the sense that it allows the interchange of cables without having to cut or unsolder them.

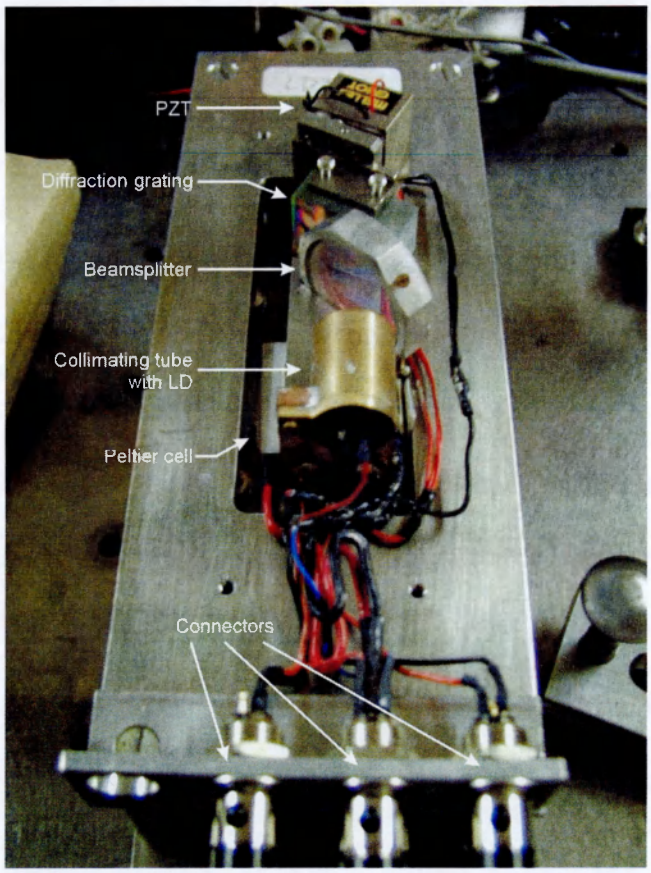

Figure 4.3 - The new laser system. Lid not shown.

4.2.2 New laser systems built

Apart from updating the existing laser systems, two new systems have been built: one slave laser to the ECDL providing the MOT repumping beam and the coupling beam for EIT-type experiments; and one system lasing at 795 nm (the Rb D_1 line).

The new slave system was built with the upgrades described in the previous section. It is injected by the laser that previously [7,8,45] provided the coupling beam

for the EIT experiments and the repumping beam for the MOT, and gives out a peak power of 55 mW. This is the power available to both coupling and repumping beam, but only ≈2 mW are needed for good repumping (see Section 4.4 below).

The second system, for a 795-nm source, was built at Imperial College using the design described in [105]. This design is not as good as the one described in the previous section, but it is cheaper and simpler. Its main disadvantage is the fact that the output laser beam changes direction when the alignment of the grating is changed. This makes it difficult to align for a certain wavelength, but once it is set, the problem disappears. However, it is a robust system and exhibits a large mode-hop-free operation.

This system uses a 100-mW SDL-5311-G1 SDL diode laser as its source to give a 795-nm beam of 25 mW after taking <10% for monitoring. It is mounted on a breadboard on a side bench, from where the beam is carried to the optical table using a single-mode optical fibre. Unfortunately, this caused feedback in the laser because the fibre was cleaved perpendicularly (PC type), but the use of an optical isolator and the slight misalignment of the fibre coupler reduced the feedback to an operational level. The power at the output of the fibre is 8 mW, which means it cannot be used for applications demanding high power. In practice, it was used as a second, weaker coupling field for the doubly driven V system described in Chapter 6, and as a repumper in the transient EIT experiments described in Chapter 5.

4.2.3 The new saturated absorption set-up and locking system

The saturated absorption set-ups used to monitor and lock the wavelength of the lasers were also replaced to allow the subtraction of the Doppler background and a more reliable locking. Figure 4.4 shows the new saturated absorption set-up (for a description of the previously used set-ups see [87]). The monitor beam is split into three beams by a thick Pyrex window. The beams reflected off the front and back faces of the window are

used as probes, while the one transmitted through is used as pump. The probes go through the Rb cell and a 50% beamsplitter towards a mirror, which reflects them onto a photodiode. The pump is reflected off a mirror and then off the beamsplitter, overlapping with one of the incoming probes. This kind of set-up exhibits good overlap between pump and probe beams and provides two output signals: the pump and one of the probes provide a saturated absorption signal, while the other probe alone provides the Doppler background.

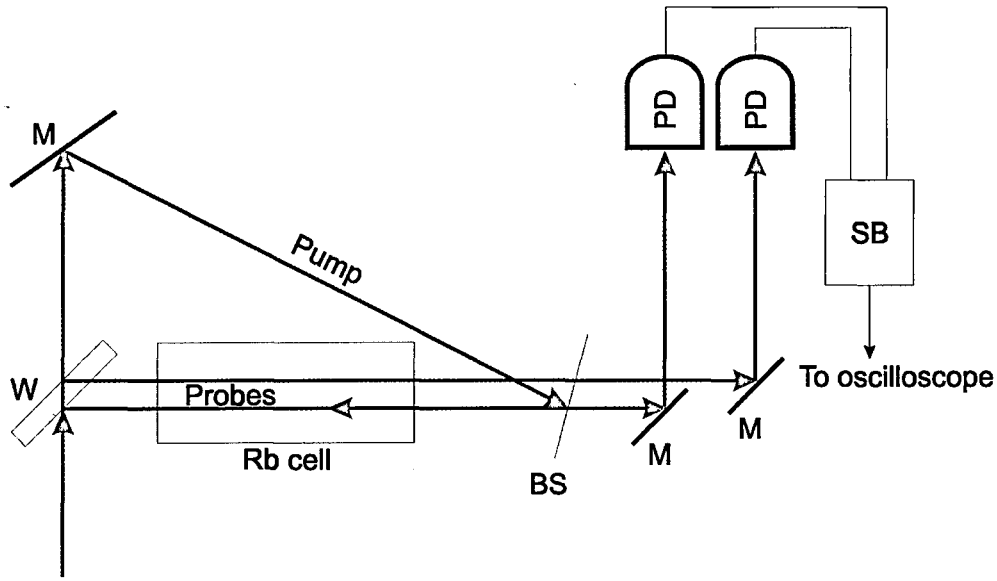

Figure 4.4 - New saturated absorption set-up. W is a thick window, BS is a 50% beamsplitter, M is a mirror, PD is a photodiode and SB is the subtraction box.

If these two signals are subtracted, then it is possible to remove the Doppler background completely. Figure 4.5 shows the saturated absorption profiles of the ^{87}Rb $5S_{1/2}(F=2)$ to $5P_{3/2}$ transitions (a) with the Doppler background and (b) without it (for other profiles, including those for ^{85}Rb, see Appendix A). Although the signal presented in Figure 4.5(b) provides ideally a better locking, in practice there were initially some limitations. The fact that the two probes have different intensities makes it impossible to subtract the Doppler background completely without sacrificing some of the intensity of the saturated absorption signal. Then, a compromise was found for each laser between

intensity loss and Doppler subtraction so that a good locking was achieved, although in practice we don't usually do Doppler subtraction unless necessary. The Electronics Workshop built a circuit to perform the subtraction of the two signals (job No. 2108). This circuit has gain and offset control for one of the inputs to balance the two signals, and also gain and offset control for the output signal.

The locking of the laser wavelength was accomplished by a laser diode stabiliser circuit based on a system used at Clarendon Laboratory (Oxford) and adapted by S. A. Hopkins (Electronics Workshop No. 1985). This circuit has the advantage of locking to the peaks (or dips) of the lines instead of their sides, as in the old set-up, giving a more robust locking. This way it is possible to lock the lasers to the desired line and avoid the use of AOMs. However, in practice, the lasers were locked to a crossover peak and then shifted where necessary, because the crossover peaks are more intense than the actual line peaks and give a better locking.

These locking circuits work by modulating the current of the lasers at a rate of 100 kHz and so required that the photodiodes used for signal detection were changed for faster ones. Fast new photodiode and amplifier systems were built for this purpose by the Electronics Workshop (job No. 2108), which can detect signals up to 175 kHz.

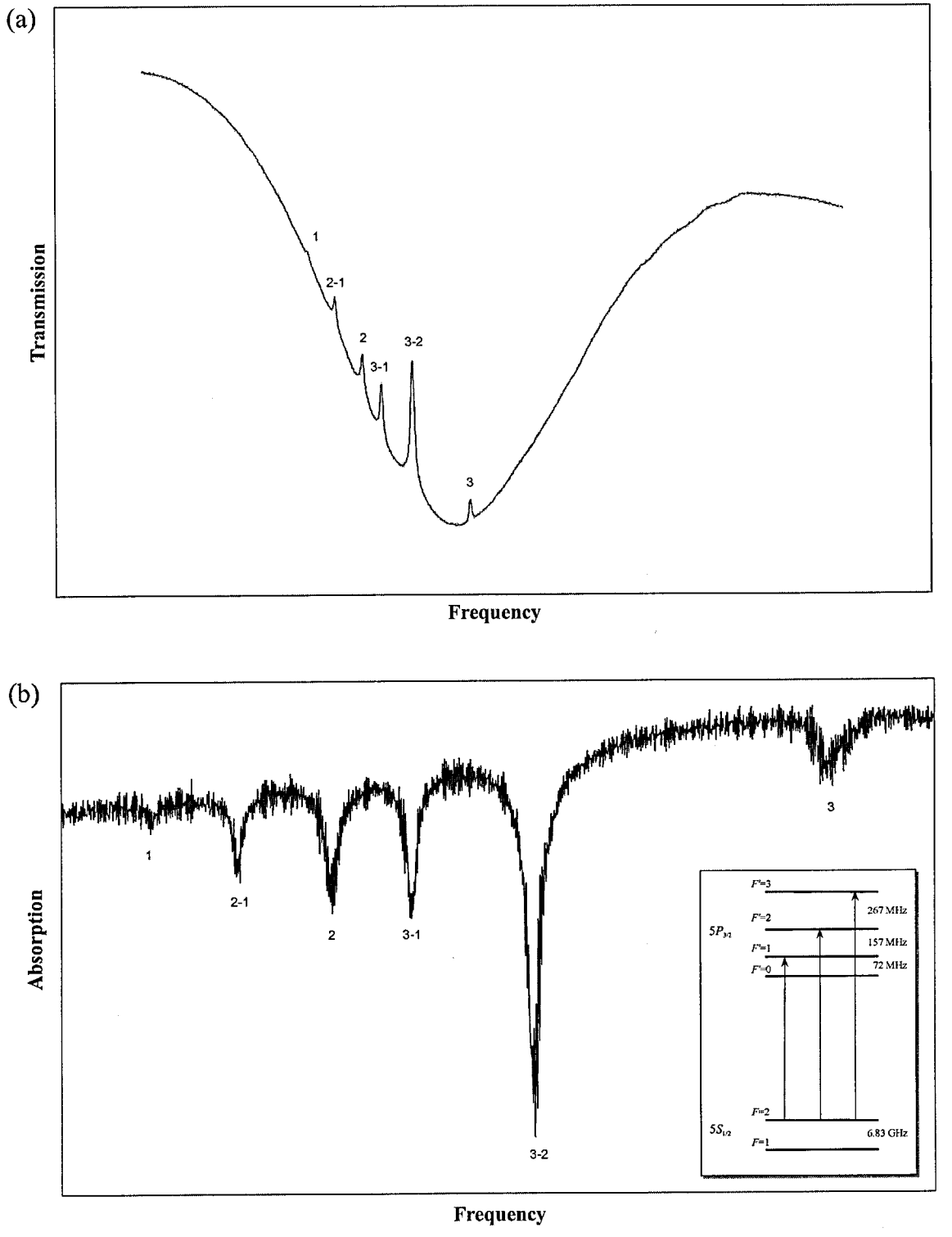

Figure 4.5 - Saturated absorption profiles of the ^{87}Rb $5S_{1/2}(F=2)$ to $5P_{3/2}$ transitions (a) with Doppler background and (b) without. Each line and crossover is labelled according to its F' number.

4.3 Expanded-beam MOT

Figure 4.6 shows the new optical set-up using the upgraded laser systems described in the previous Section. The 795-nm system is shown in a dashed box as it is on a side bench and its beam is brought to the optical table by an optical fiber. This system was used as a repumping (*R*) or coupling (*C*) field in the experiments. A 780-nm master-slave system was also used to produce coupling and repumping light. The trapping beams *T* are generated by another 780-nm master-slave system. The beam used to probe the cold sample is labelled *P* and it is produced by an ECDL.

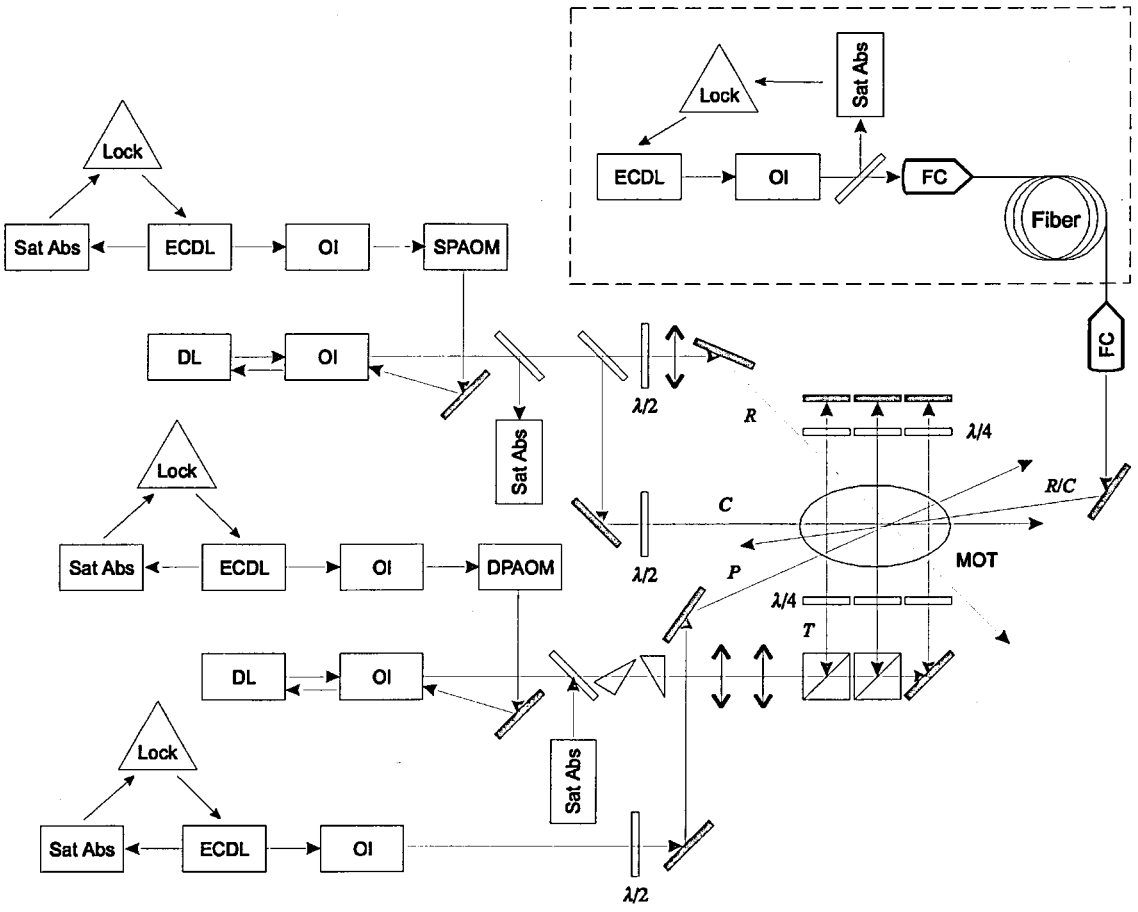

Figure 4.6 – Schematic of the optical set-up. DL: diode laser, ECDL: external-cavity diode laser, Sat Abs: saturated absorption set-up, OI: optical isolator, SPAOM/DPAOM: single/double pass AOM, FC: fiber coupler.

We trapped ^{87}Rb atoms using the D_2 line for all our experiments in this thesis, as shown in Figure 4.7. The trapping field *T* was detuned from the

$5S_{1/2}(F=2)-5P_{3/2}(F=3)$ transition, while the repumping field R was usually tuned to the $5S_{1/2}(F=1)-5P_{3/2}(F=2)$ transition. For some experiments, we used the repumper in the $5S_{1/2}(F=1)-5P_{1/2}(F=2)$ transition of the D_2 line (shown dashed in Figure 4.7).

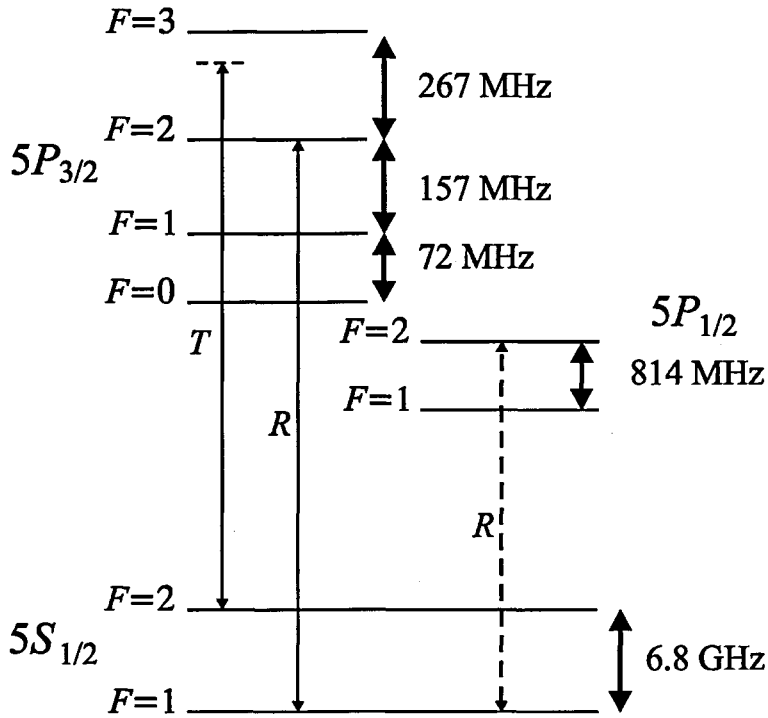

Figure 4.7 - Trapping field configuration used in ^{87}Rb.

With the new diode laser systems in operation, there was more power available to the trapping and repumping beams, namely ≈50 mW and ≈25 mW respectively. Ideally this would allow us to increase the diameter of the trapping beams substantially, while maintaining their intensity (I_T≈12 W/cm^2). However, this was not possible in practice because of the small clear aperture of certain optical elements (like waveplates) and especially the MOT cell windows. We adopted the compromise of increasing the beams' diameter from 10 mm to 15 mm, despite the distortion caused by the windows of the cell. The repumping beam was also expanded to an elliptical profile of 20×6 mm to give a maximum intensity of I_R=26 mW/cm^2.

The expansion of the trapping and repumping beams produced an increase in the number of atoms trapped from ~10^7 to ~10^8 (measured with the calibrated photodiode)

and in the size of the cloud of atoms from 0.5 mm to 3 mm (see Figure 4.8). Figure 4.9 shows the number of atoms trapped N as a function of magnetic field gradient $\partial B_z/\partial z$ and trapping beam detuning Δ_T that were obtained experimentally with the expanded trapping beams. For a power and diameter corresponding to a total average intensity of $I_T \approx 60$ mW/cm^2, the maximum number of atoms $N = 9.3 \times 10^7$ is trapped for a detuning of $\Delta_T = -15$ MHz and a maximum $\partial B_z/\partial z = 15.7$ G/cm. It is not empirically clear whether N will continue to grow with $\partial B_z/\partial z$ or has reached its maximum and will decrease with $\partial B_z/\partial z$, as the maximum is very near the limits of our apparatus. To answer this question it would be necessary to achieve a bigger $\partial B_z/\partial z$ and/or to expand the beams further. This is one of the reasons for developing the second-generation MOT (see Section 4.6).

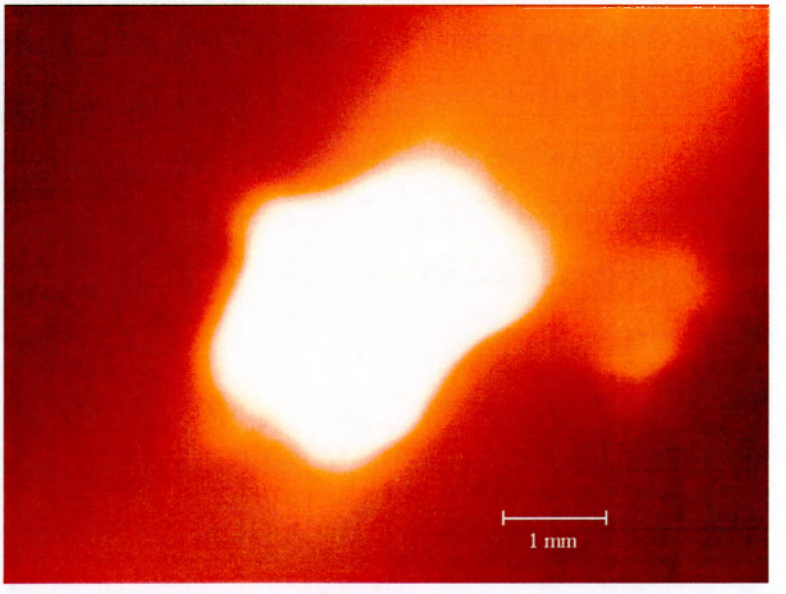

Figure 4.8 - Cloud of cold ^{87}Rb atoms. The cloud contains 10^8 atoms and is 3 mm in diameter. The extra spot to the right of the cloud is a reflected image.

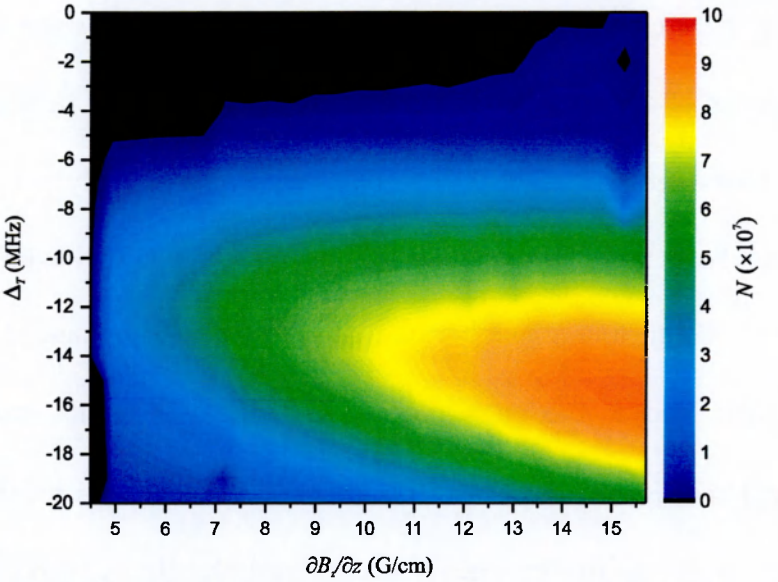

Figure 4.9 – Observed number of trapped atoms as a function of trapping beam detuning and magnetic field gradient. I_T=60 mW/cm^2, I_R=26 mW/cm^2.

We have also studied experimentally the dependence of the fluorescence of the atoms trapped (measured by the photodiode) as a function of the repumper intensity. Figure 4.10 shows such experiment for $\Delta_T = -15$ MHz, $\partial B_z/\partial z = 15.7$ G/cm and a repumping beam profile 20×6 mm of elliptical shape. We note that the photodiode signal rises sharply for low powers, but reaches a point at a power of ≈1.5 mW, corresponding to an intensity of ≈0.2 mW/cm^2, where the rate of change becomes much

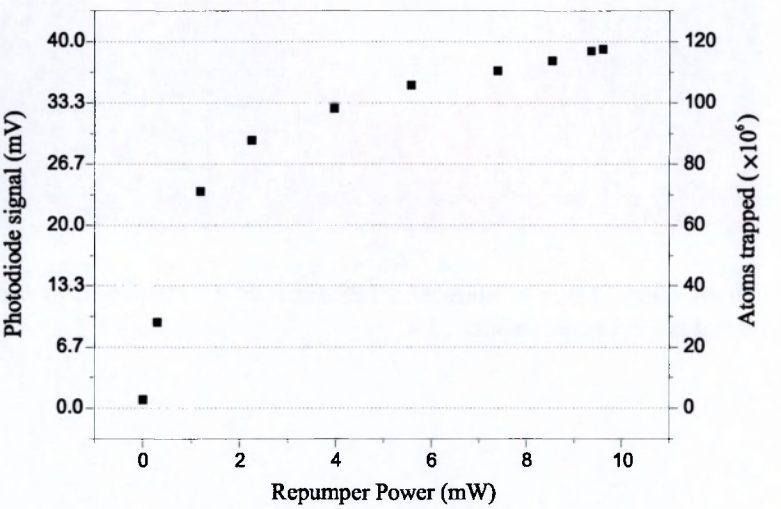

Figure 4.10 – Photodiode signal and inferred number of atoms trapped as a function of the repumper power.

shallower. This power may correspond to the point where the rate of atoms repumped becomes equal to the rate of atoms falling into the lower ground state. After this point, the repumper does not contribute to the trapping any more and the repumping light is scattered, causing the photodiode to record an apparent increase in the number of atoms (inferred from the photodiode signal and shown on the right axis) as the power is increased.

4.4 Preliminary dark SPOT

In a normal MOT, the maximum achievable atomic density is limited to $\approx 10^{10}\,\mathrm{cm}^{-3}$ by light pressure due to the multiple scattering of trapping beam fluorescence, which opposes the confinement forces of the trap [95,101]. This limitation can be overcome by using the so-called dark SPOT configuration, first introduced by W. Ketterle *et al.* in 1993 [106]. A dark region is imprinted in the centre of the repumping beam so that the atoms that fall to the lower ground state in this region are not repumped. These atoms are transparent to the trapping beams and the trap fluorescence that opposes the confining forces of the trap is eliminated, allowing the density of the atoms in the trap to increase. This increase can also be achieved with a doughnut mode MOT [107], although it is a more complicated arrangement.

Working with a sodium MOT, Ketterle *et al.* [106] used trapping beams with diameters of ≈3 cm and intensities of $\approx 10\,\mathrm{mW/cm}^2$. Two repumping beams (diameter 3 cm, intensity $3\,\mathrm{mW/cm}^2$) intersected at an angle of 20° in the trap after passing through a glass plate with a dark dot, which was imaged into the trap with an image size of ≈1 cm. In their normal MOT, without the dark spot, 10^{10} sodium atoms were trapped in a cloud of ≈1 cm diameter, equivalent to a density of $2\times 10^{10}\,\mathrm{cm}^{-3}$. In their dark

SPOT configuration, up to 5×10^{10} atoms were trapped in a cloud 2-4 mm in diameter, which corresponds to a density of $\approx8\times10^{11}$ cm^{-3}, almost 2 orders of magnitude larger than with their normal MOT. Townsend *et al.* [108] have achieved similar densities with caesium atoms, overcoming a few problems associated with the large hyperfine level separation of heavy alkali-metal atoms.

We have carried out preliminary experiments in our MOT with the purpose of implementing this technique in the new second-generation trap described Section 4.6. We used an arrangement for the dark SPOT similar to that of Ketterle *et al.* but using only one repumping beam, tuned to the $5S_{1/2}(F=1)-5P_{3/2}(F=2)$ transition. This does not produce a true dark spot, but a long dark/grey region as the image of the dark dot blurs out of the image plane. We note that this problem could be overcome by using two intersecting truly hollow beams produced by axicon lenses [109] or a diffraction technique [107].

The repumping beam passes through a pair of circularising prisms and then a glass window with a copper disc of diameter 1 mm stuck on it, which is imaged into the trap by a plano-convex lens (see Figure 4.11). This imaging method allows us to vary the size of the imaged dark spot by varying the distance s' between the lens and the trap and the distance s between the lens and the disc. However, due to lack of space on the optical table, time and optical components, we were only able to study two different

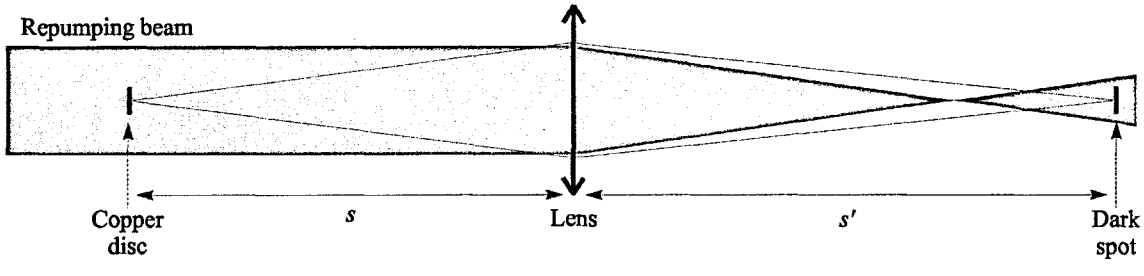

Figure 4.11 - Imaging of a dark spot.

image sizes, namely ≈2.5 mm and ≈2.0 mm. A lens of focal length f=150 mm was used for both cases.

For the 2.5 mm spot we used distances s=210 mm and s'=525 mm, which produced a repumper of diameter ≈7.5 mm in the trap. We studied a range of repumper powers by probing the sample with a 1 mm beam of 2 μW. Figure 4.12 shows the probe absorption spectra of the two ^{87}Rb ground states with and without the dark spot for two selected repumper powers: (a) 0.35 mW and (b) 23 mW (the sample is optically thin). The lower power case is the one that gives the largest probe absorption in the F=1 ground state with the dark spot, while the higher power case is the one of maximum achievable repumping power. According to Figure 4.10, this case is expected to have the maximum number of atoms trapped in the F=2 ground state without the dark spot. However, this maximum power does not give the largest number of atoms in F=1 with the dark spot. This might be due to repumping light scattered from the atoms in the cell and reflected by the cell's windows. The number of trapped atoms quoted in Figure 4.12 was calibrated from the trap fluorescence and corresponds to the atoms in the F=2 ground state. This is the case because the atoms in F=1 do not interact with the trapping beams and hence do not fluoresce.

Note that the F=2−F'=2 transition peak without the dark spot of Figure 4.12(b) exhibits Autler-Townes splitting. This is because the repumper in this case is strong, and forms a Λ-type system with the probe for this transition. This feature is not visible in any of the other cases because the repumper is not sufficiently strong, either because of the presence of the dark spot or the beam power.

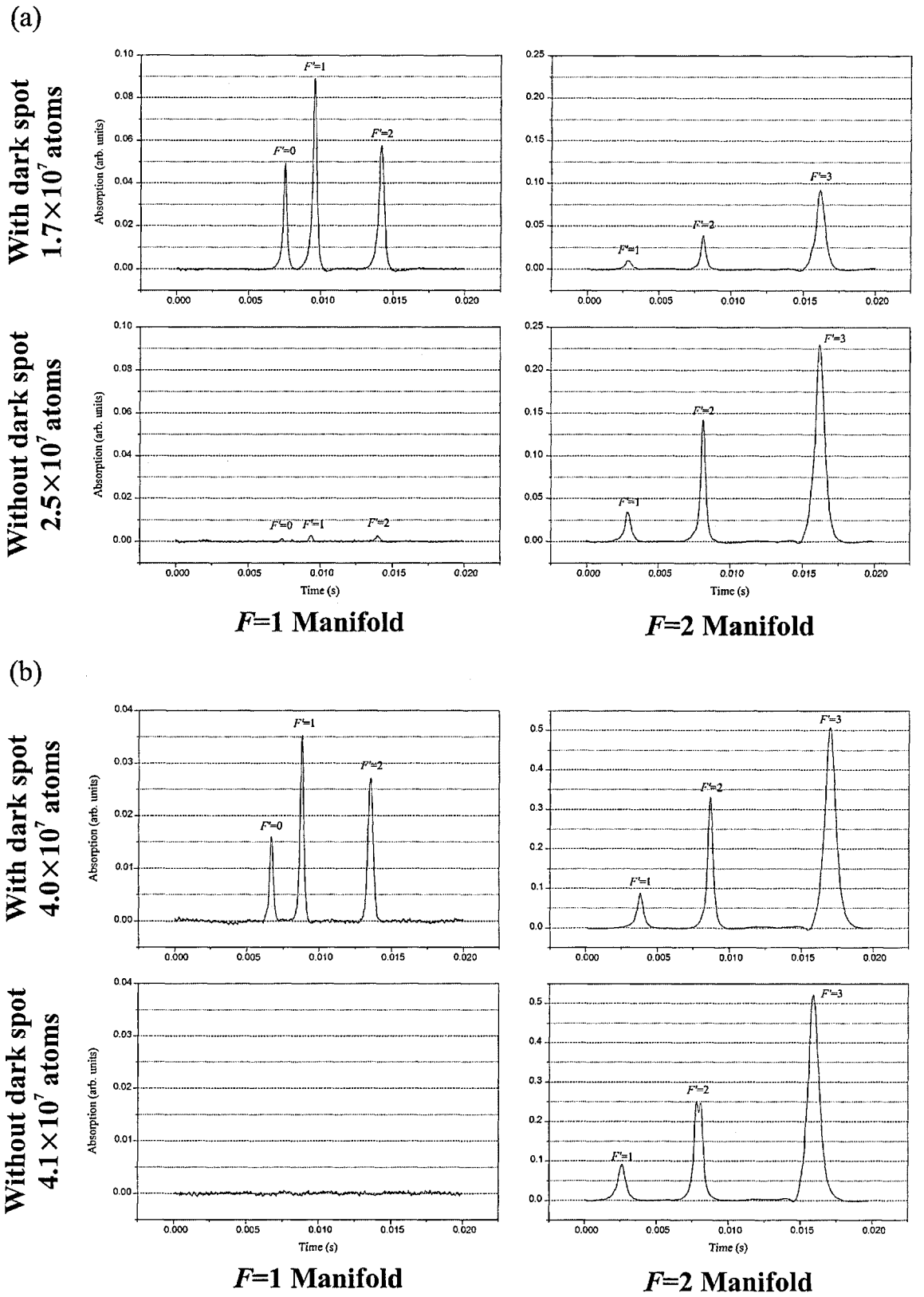

Figure 4.12 - Probe absorption of the two ground states with and without dark spot for a repumper power of (a) 0.35 mW and (b) 22.9 mW, and a dark spot of 2.5 mm. Each trace is an average of 50 scans.

By comparing the absorption depths of atoms trapped in $F=2$ and $F=1$ and knowing the number of atoms trapped in $F=2$, we can deduce the number of atoms trapped in $F=1$. Given the fact that our sample is optically thin, the intensity absorbed A on a transition is given by

$$A \approx az, \tag{4.1}$$

where a is the absorption coefficient of that transition and z the distance travelled through the absorptive medium (i.e. the cloud). The absorption coefficient is proportional to the ground state population density η and the line strength S of the transition. Then, taking the ratio of the absorptions on any two different hyperfine transitions we have

$$\frac{A}{A'} = \frac{\eta S}{\eta' S'}. \tag{4.2}$$

So, taking into account the line strengths for the ^{87}Rb transitions involved and assuming that the population in each ground state is equally distributed within the Zeeman sublevels, we have that the absorption peaks should be in the ratio 2:5:5 for transitions from the $F=1$ ground state and 1:5:14 for transitions from the $F=2$ ground state. However, it is clear that the experimental absorption peaks in Figure 4.12 are not in these proportions. We have therefore studied the possibility that the population is not distributed uniformly among the Zeeman sublevels, but we found that no single distribution of Zeeman population could fit all the absorption peaks of each ground state. All this leads us to believe that the probe optically pumps the population among the Zeeman sublevels as it is scanned across the different transitions, arranging a different population distribution as it scans each one of them. Note that the probe Rabi frequency is $\approx$1.4 MHz and each peak is scanned in $\approx$1 ms, which is long compared to the optical pumping time $\approx$0.5μs. Unfortunately, the absorption peaks in Figure 4.12

were not calibrated and so it is not possible to calculate the population distribution of the Zeeman sublevels for each transition, and hence the population in the $F=1$ ground state. However, we can say that, for the lower repumper power case, it is of the same order of magnitude as the population in the $F=2$ ground state.

In the case of a dark spot of 2 mm, we used the same lens but with distances $s=225$ mm and $s'=450$ mm, which produced a repumping beam of diameter 6 mm in the trap. Only the low power case was studied for this set-up, corresponding to a repumping power of 0.28 mW. Figure 4.13 shows the results obtained for these parameters. Comparing the relative heights of the absorption peaks of the two ground states of Figure 4.12 and Figure 4.13, one can see that they are in approximately the same proportion in both cases, but there is a bit more population in $F=1$ in the latter.

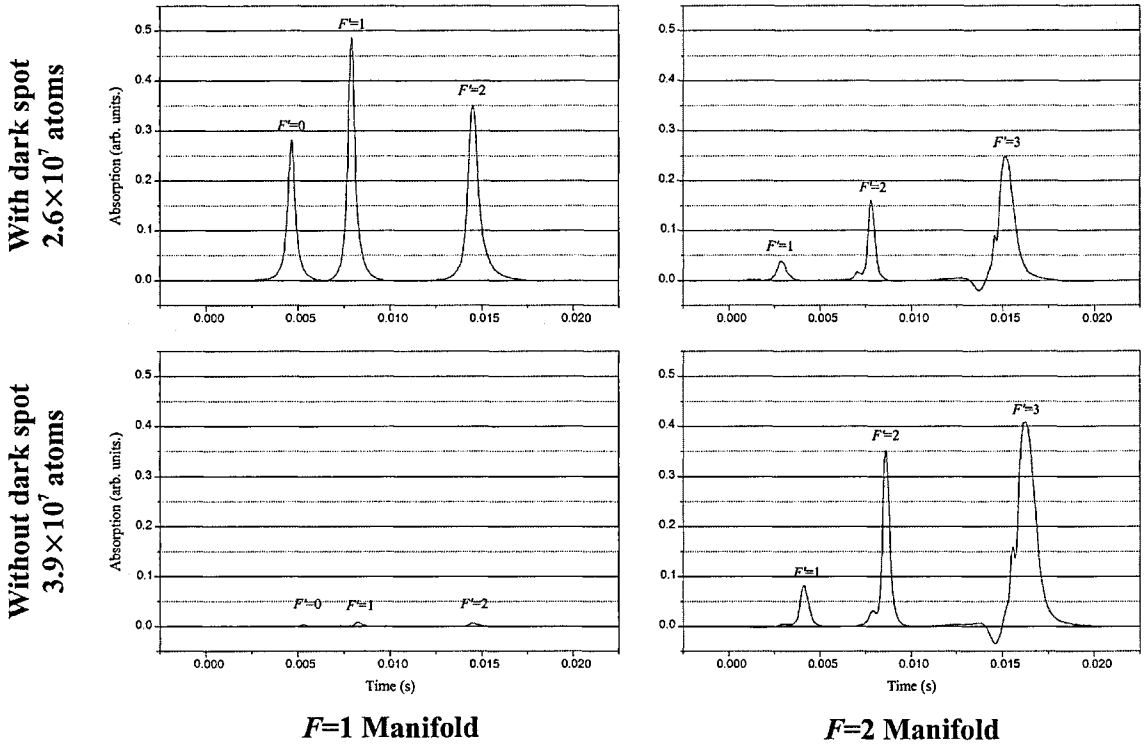

Figure 4.13 - Probe absorption of the two ground states with and without dark spot for a repumper power of 0.28 mW and a dark spot of 2 mm. Each trace is an average of 50 scans.

The $F=2$ manifold peaks in Figure 4.13 exhibit structure due to the trapping fields forming a V-type system with the probe for these transitions. The $F'=1, 2$ peaks are

split in an Autler-Townes fashion, while the feature on the $F'=3$ peak is due to stimulated Raman processes between adjacent Zeeman sublevels [47,110]. We found that these features depend on the alignment of the probe with respect to the trapping beams, and are not always visible, like for example in Figure 4.12.

In these two preliminary experiments the repumper beam diameter in the trap was constrained to approximately half that of the trapping beams by the dark spot imaging system. This is not an ideal case, because the MOT operates best when the repumper is the same size or larger than the trapping beams. Furthermore, we have used only one repumping beam and the dark region is not a true dark spot. However, we have demonstrated that a reasonable number of atoms can be accumulated in the $F=1$ ground state using our very simple arrangement. Following these preliminary experiments, we have now implemented the dark spot in a better way in the new second-generation MOT, described in Section 4.6.

4.5 Computer control and data acquisition

As a result of the migration from an Apple Macintosh to a Windows PC platform, the computer control and data acquisition system has been completely redeveloped for the experiments described in this thesis by the Author.

4.5.1 Hardware

New National Instruments data acquisition boards have been installed in a Windows PC: an AT-AO-10 analogue output board, a Lab-PC-1200AI analogue input board, a PCI-6602 counter/timer board, a PCI-1409 image acquisition board, and a GPIB-PCII GPIB communication board.

The AT-AO-10 is an analogue output board consisting of 10 output channels and 8 TTL digital I/O lines. The output channels can provide up to 10 V unipolar or bipolar with a resolution of 12 bits and a sampling rate of 200 ksamples/s per channel. They are used in the unipolar mode to control the current of the anti-Helmholtz coils and the frequency shift of the trapping, coupling, and probe beams AOMs. The digital lines have not been used.

On the other hand, the Lab-PC-1200AI is an analogue input board with 8 analogue input channels, 24 TTL digital I/O lines and 3 counter/timers. The input channels can read from 0 to 10 V (unipolar mode) or from −5 to 5 V (bipolar mode) at a rate of 100 ksamples/s per channel. Only one analogue input channel has been used in unipolar mode, connecting the photodiode that measures the number of atoms trapped.

All the on/off operations have been performed with the PCI-6602 counter/timer board. This board has 8 high-speed counter/timers and up to 32 TTL digital I/O lines (8 dedicated, up to 24 shared with counter/timers). Five digital I/O lines with a rise/fall time <5 ns have been used to turn on/off the 3 AOMs, the anti-Helmholtz coils and the shutter.

An image of the cloud of atoms trapped can be captured by the PCI-1409 image acquisition board connected to the monitoring camera (see Figure 4.8). This board is able to acquire monochrome images of up to 1024 grey scales from 4 different video sources at a rate of up to 60 frames/s.

Finally, we have the GPIB-PCII GPIB communication board, which can be used to connect the digital oscilloscope and other GPIB-enabled instruments to the computer. In practice, this board has not been used because of conflict between the different pieces of hardware and the distance between the oscilloscope and the computer (GPIB cables can have a maximum length of 1 m).

4.5.2 Software

The data acquisition program consists of a series of small programs built with *Microsoft Visual Basic 6.0* (VB) and the National Instruments drivers supplied with the boards. A program called *DAQ Master* (`DAQ.exe`) was written to call all the other programs (tasks). The task programs are also executable programs compiled with VB, but they have been renamed as `.daq` so that *DAQ Master* can recognise them as tasks.

DAQ Master consists of a series of panels in which the tasks are classified (see Figure 4.14). The panels can be added, removed or renamed by clicking on one of the buttons placed at the bottom of the window. Each panel contains an icon list, listing all the tasks available in that panel.

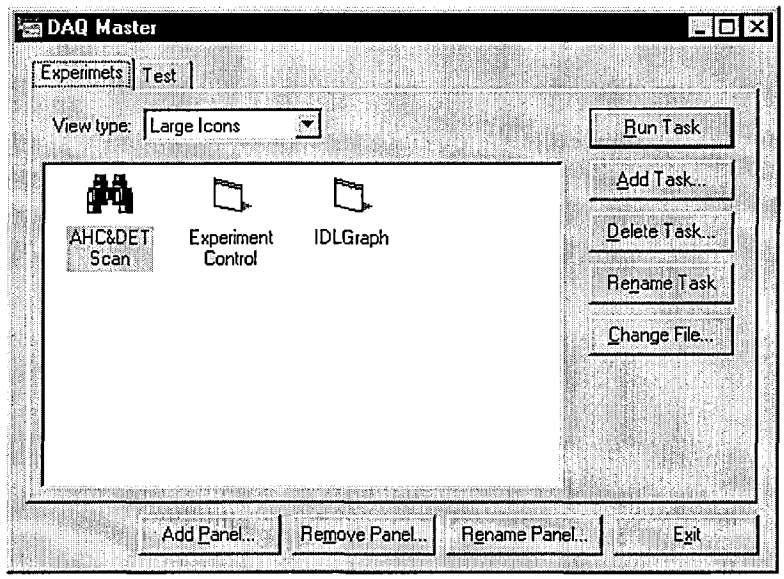

Figure 4.14 - *DAQ Master* window.

Each icon in the list represents a task and is associated with a `.daq` file. Tasks can be executed by clicking the Run Task button or by double clicking on the task icon or text. They can also be renamed, added or deleted by clicking on the corresponding button. The `.daq` file associated with each task can be changed by clicking the Change File... button.

At the moment, there are two panels: Experiments and Test; holding different tasks. For more information on these tasks refer to Appendix B.

4.6 The second-generation MOT

As previously mentioned in Section 4.1.2, the first-generation MOT had several limitations:

- Small windows, allowing only 1-cm trapping beams without distortion, leading to $\sim 10^8$ atoms being trapped in the best circumstances, with densities of $\sim 10^{10}$ cm^{-3}.
- Limited magnetic field gradient, with a maximum of only $\partial B_z/\partial z = 15.7$ G/cm, which also limits the number of trapped atoms and densities.
- Poor window flatness of only 2λ per centimetre, which is insufficient for good quality interferometry.

To overcome these limitations and to obtain a much higher density of trapped atoms, we have designed and built a new, second-generation MOT. We also took the opportunity to improve the beam access to the cell and fix the MOT in a more robust way to the optical table. Although we haven't had enough time to fully characterise this new MOT at the end of the Author's Ph.D., it is now being used for the current experiments to measure cross-phase modulation in a four-level N system (see Section 7.2.2).

4.6.1 MOT design

This new trap is based on a design described by C. Wieman *et al.* in 1994 [111]. It was built around a UHV reducer six-way cross with 4 CF70 ports and two CF114 ports,

using standard Polaron CVT parts. Figure 4.15 shows a schematic drawing of the MOT. One of the CF70 ports is connected to a UHV all-metal valve and an AML AIG17G Bayard-Alpert ion gauge, which is used to monitor the pressure. The port opposite this one is a CF70 port connected to another UHV valve and a blanked up-to-air valve, in case the system needs to be let to air for any reason. Perpendicularly, in the horizontal plane, there are two more CF70 ports. One is connected to an MDC reducer adapter and UHV valve with a Rb finger. The other is connected to a reducer T piece with a two-way 10 A 500 V feedthrough mounted on a CF34 flange, a VAT manual gate valve (part No. 01032-CE01), a 50-cm flexible bellow and a Perkin Elmer 20 l/s ion pump. Finally, perpendicularly to all four CF70 ports, in the vertical direction, there are two CF114 ports. The top one is connected to a bored flange where a Comar optical window (part No. TB/33) is glued with Torr Seal. The other one is connected to a CF150-CF114 reducer flange, which is connected to a bored flange, where a specially made Hellma optical glass cell is glued with Torr Seal and two SAES Rb getters (part No. Rb/NF/7/25/FT10+10) are fixed.

The top window is 8 mm thick and 63 mm in diameter, allowing beams of diameters up to 60 mm. It is flat to $\lambda/4$ over 90% of its diameter. The cell at the bottom is 10×6×6 cm with walls 6 mm thick, which means that up to 48 mm beams can go through. A technician from Imperial College measured the flatness of the cell to be better than $\lambda/2$ over the central 30 mm diameter of each surface. The vertical beam is further restricted by the bore of the CF150 flange, which has a diameter of 50 mm.

The Rb finger and/or getters are the source for the trapped atoms. There are two getters screwed on the bored CF150 flange, isolated from it by evacuated macor standoffs. These are connected in series and to the feedthrough by Caburn MDC KAP2 Kapton wire. The getters release Rb when a current greater than 5.3 A is run through

and the amount released is proportional to the current. This is why the getters are preferred to the finger; they release Rb directly in the cell when it is necessary and only the necessary amount. Although this method of loading the trap has been used before [111,112], we still connected the Rb finger in case the getters failed to work to our expectations.

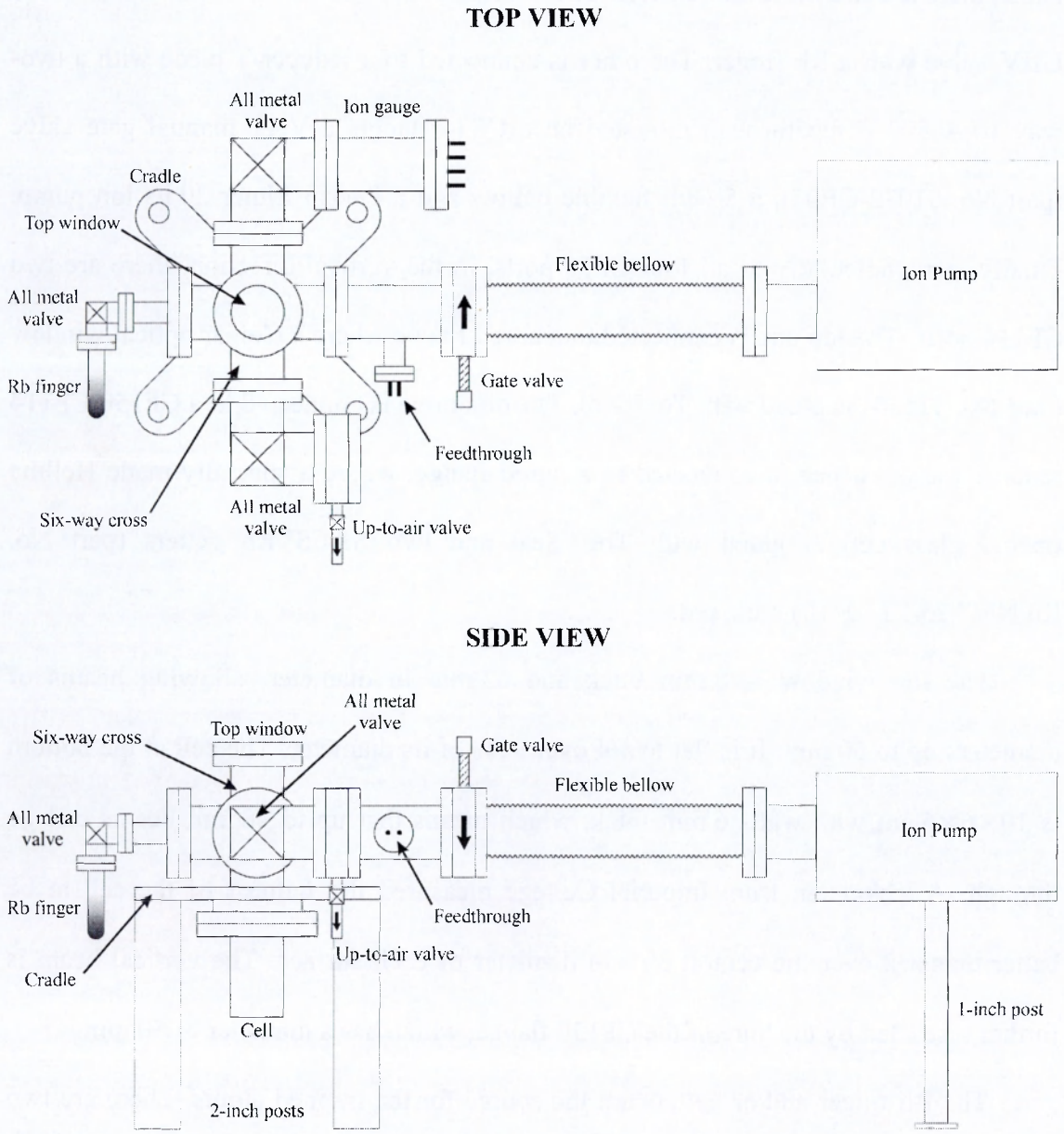

Figure 4.15 - Schematic of the second-generation MOT.

The trap is supported by four stainless steel posts and a cradle, built by Mr Roger Bence of the Physics Department Workshop. The posts are 2 inches in diameter and are

screwed onto the optical table, so that the cell is fixed with respect to the trapping beams. The ion pump is supported by a separate base on a 1.5-in post, also built by the Workshop, to distribute the weight. It is connected through the 50-cm flexible bellow to allow for any height difference between the pump and the six-way cross, and also to separate the pump far enough so that there is minimal influence from its magnets on the magnetic field generated by the anti-Helmholtz coils (described in Section 4.6.3).

4.6.2 The baking process

The MOT requires a background Rb pressure between 10^{-7} and 10^{-9} torr (1 mbar=0.75 torr=10^2 Pascal) for good operation [111]. A lower pressure would result in loading rates too slow, while a higher pressure would result in a background Rb atom density similar to that of the trapped atoms, making it difficult to discriminate between trapped atoms and background Rb atoms. The background pressure due to other, non-rubidium atoms, should be lower than the working background Rb pressure, to avoid foreign atom collision effects. A non-Rb background pressure an order of magnitude less than the background Rb pressure is desirable. The vapour pressure of Rb at room temperature is $\approx 3\times10^{-7}$ torr and so we aim to achieve a vacuum of $\sim10^{-9}$ torr for a good working MOT.

The pressure p achieved in any vacuum system is given by

$$p = QA/S, \tag{4.3}$$

where Q is the outgassing rate of the walls of the system, A is the total area of the walls of the system, and S is the pumping speed of the pump. In our case $A\approx3100\,\mathrm{cm}^2$, S=20 l/s and a typical outgassing rate for clean stainless steel at room temperature is $Q\approx10^{-10}$ torr l $\mathrm{s}^{-1}\mathrm{cm}^{-2}$, which gives a pressure $p\approx2\times10^{-8}$ torr. This pressure is an

order of magnitude larger than the non-Rb background pressure needed, and therefore it has been necessary to bake the system to reduce Q by at least an order of magnitude.

In 1992, D. J. Santeler quoted data on the effect of baking stainless steel to different temperatures [113]. Some of this data is presented in Table 4.2, showing that it is necessary to bake the system at 200°C for 20 hrs at least to achieve the necessary Q. However, in practice it was not possible to bake the whole system at such a temperature because parts of it wouldn't sustain a hot bake, these parts being the feedthrough (150°C), the glass cell (100°C), the Torr Seal (120°C) and the gate valve (250°C open, 200°C closed). It is for this reason that it was decided to make an initial hot bake (300°C) of all the metal parts for 2 days, then open the system to dry nitrogen and connect the other parts for a low temperature bake (90°C).

Table 4.2 - Outgassing rates Q in torr l $s^{-1}cm^{-2}$ for different baking temperatures and times. (From [113].)

Baking Temp.	Baking Time			
	20 hrs	40 hrs	100 hrs	200 hrs
150°C	6.3×10^{-11}	5.3×10^{-11}	2.8×10^{-11}	2.0×10^{-11}
250°C	6.3×10^{-12}	5.3×10^{-12}	2.8×10^{-12}	2.0×10^{-12}
400°C	4.0×10^{-13}	1.7×10^{-13}	1.0×10^{-13}	1.0×10^{-13}
500°C	8.0×10^{-15}	8.0×10^{-16}	4.0×10^{-17}	8.0×10^{-19}

In the end, the cell remained open to air for two days after the hot bake, because of complications at the time of connecting the "temperature sensitive" parts for the low temperature bake. The pollution of the system during this period meant that the vacuum pressure didn't fall significantly in the first week of baking. It was then decided that, in order to accelerate the process, we would bake the outer regions of the trap (i.e. the flexible bellow, ion gauge, etc.) at a temperature of 200°C and the central regions (i.e. six-way cross and flanges with Torr Seal) at a lower temperature of 90°C. The UHV system was baked for 3 weeks under these conditions, reaching a vacuum pressure of 2×10^{-9} torr.

4.6.3 New anti-Helmholtz coils

The anti-Helmholtz coils for the second-generation MOT were wound on two aluminium formers of 70 mm radius and 20 mm wide, separated by a distance of 160 mm. A polyester imide coated cable of diameter 1.25 mm was wound 233 times on each former, starting at a minimum radius of 73 mm and extending to a maximum radius of 95 mm. The inner separation between them was 168 mm and the outer separation was 208 mm.

Although the geometry used for these coils is not the one that gives maximum magnetic field gradient at the centre[1] due to the geometry of the trap, numerical calculations (see Figure 4.16) show that they can produce a gradient of 1.83 G $cm^{-1}A^{-1}$. To achieve much larger magnetic field gradients than the first-generation MOT described in Section 4.1.2, we made it possible to run up to 20 A through the coils by the use of thick wires to connect the power supply and the coils, a more powerful (3 kW) power supply and water cooling of the coils. This way we can generate magnetic field gradients of up to $\partial B_z/\partial z$=36.6 G/cm.

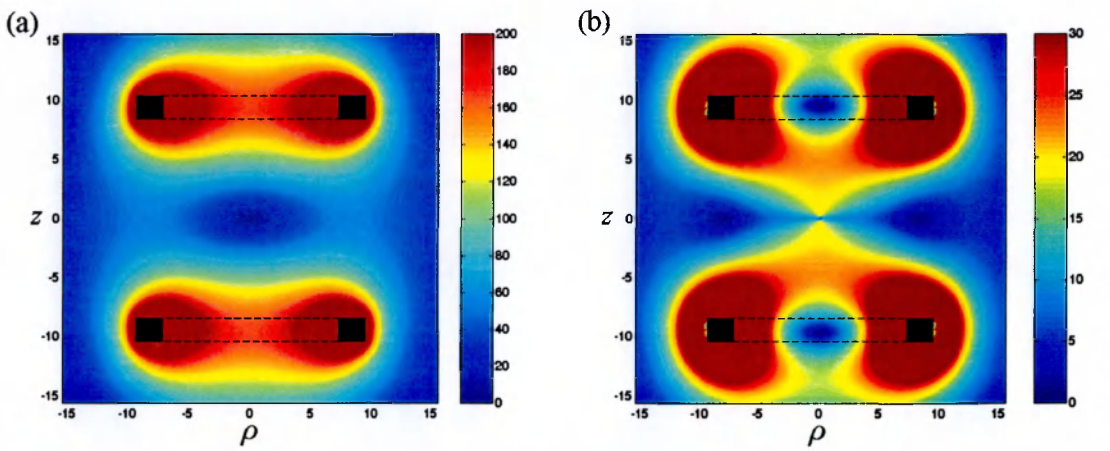

Figure 4.16 - Numerical calculations showing the (a) magnetic field and (b) magnetic field gradient in the cylindrical coordinates (ρ,z) for the anti-Helmholtz coils used and a current of 10 A. The black squares and dashed lines represent the position and extent of the coils.

[1] This geometry requires that the distance between the coils and their radius are equal.

The new anti-Helmholtz coils are held with their z-axis parallel to the optical table by a 3-axis positioning mount, so that they can be aligned precisely with respect to the laser beams.

4.6.4 Present situation of the second-generation MOT

At the completion of the Author's studentship, the MOT has been installed and tested, but not fully characterised. The trapping beams have been expanded to a diameter of 4 cm and a new and improved dark SPOT configuration has been set-up. This configuration combines two dark spot images in the centre of the trap to reduce the leakage of atoms into the grey regions of the circularised repumping beams. In this case the dark spot is generated by a ball-bearing held on a microscope slide, which produces a cleaner dark spot profile than the copper disk. Preliminary results have shown that up to 90% of the population falls into the lower $5S_{1/2}(F=1)$ ground state in this configuration with the help of a depumping laser to pump the population into this state, but no proper study has been done yet.

Chapter 5

Transient EIT Experiments

Previous work in this laboratory [7,8] made preliminary observations in our first-generation MOT of probe EIT transients immediately after switching on the coupling field. When the coupling field was switched on by a Pockels cell, the rapid rise in probe transparency exhibited an overshoot before settling down to the steady state. This overshoot was interpreted as the first Rabi half cycle in the transient nutation or ringing, but it did not reach gain owing to absorption on uncoupled Zeeman transitions and dephasing effects. In the experiments reported in this Chapter the coupling field intensity has been increased to the point where a clear Rabi ringing cycle reaching well into gain is observed. We have also extended previous work in transient EIT by studying turn-on and turn-off transients, and the region of parameter space investigated is much broader than previously studied. This is the only work we know of that studies turn-off transients for off-resonant probe and coupling fields, inversionless gain away from resonance and transient dressed state interference away from either bare or dressed

state resonance. The results are supported by density matrix computations of a three-level lambda system supplemented by observational data on the strengths of uncoupled absorptions and the effects of the MOT fields. Furthermore we present new analytical results, derived using the Laplace transform method, so extending the two-level approach presented in [114]. Our theoretical results also generalise those of Li and Xiao [15] for mutual resonance to include two-photon dephasing and arbitrary initial ground state populations, and we predict a new frequency of oscillation in the probe transient response. We also present an analytical solution, to first order in the probe strength, for the probe absorption when the coupling field is non-adiabatically turned off for arbitrary detunings of coupling and probe fields. Our analysis is performed explicitly in the bare state basis. The results provide insight into how atomic systems become dressed by intense laser fields. The work described in this Chapter has been published in Physical Review A [51,52].

The organisation of this Chapter is as follows. Section 5.1 surveys the different transient regimes studied in the past years. Section 5.2 outlines the Laplace transform method for calculating the non-adiabatic transient probe evolution of an ideal Λ system, presents some simple analytical results for coupling field turn-on and turn-off, and gives an overview of the general predictions for arbitrary detunings of both fields. Section 5.3 describes the experimental realisation of a Λ system in laser-cooled rubidium and describes the experimental set-up. Section 5.4 presents the results of turn-on experiments for resonant fields, showing that for sufficiently large coupling field Rabi frequencies, the transient probe ringing exhibits gain peaks, confirming the interpretation of previous work [7,15-17]. This is followed by Section 5.5, where probe transients are studied over a very wide range of probe and coupling field detunings in

both turn-on and turn-off experiments. The summary and conclusions are presented in Section 5.6.

5.1 Different transient regimes

A natural classification of EIT response with switched fields is based on the relative time scales involved. In the *adiabatic* regime the switching is assumed to occur sufficiently slowly that the system evolves smoothly from one steady state to another. For EIT systems where the Rabi frequency is comparable to the atomic lifetime, the switching is adiabatic when it occurs on a time scale that is long compared with the relevant optical pumping times. For example, steady-state Λ-type EIT with resonant fields is characterised by the ground state populations being in the dark (non-absorbing) superposition of the two ground states. If the intensity ratio or relative phase of the two optical fields changes, then the composition of the non-absorbing superposition state changes, and so the populations have to be pumped into the new non-absorbing state to maintain transparency. Thus the adiabatic condition requires the switching of the optical fields to be slow compared with the time taken for optical pumping from the light (absorbing) state to the dark state. This is the regime used in the recent studies of optical information storage and retrieval [53,115], the single photon switch [9] and its classical precursor [29,116].

There is another adiabatic regime in pulsed systems where evolution occurs between ground states without spontaneous dissipation. In the work by Harris and Luo [14] on the conditions for preparing EIT, this was achieved by using extremely large Rabi frequencies so that all system evolution to the dark state was achieved on timescales much shorter than the spontaneous emission time. Not requiring such

extreme Rabi frequencies, adiabatic switching using the well-known STIRAP schemes [117] decouples the evolution from the spontaneous emission, and so adiabatic evolution occurs on timescales independent of spontaneous emission time. The picosecond pulse experiment of Nottlemann *et al.* [50] is also effectively in the adiabatic regime. In their experiment the relative phase of the two Zeeman ground states oscillates by RF Larmor precession in a magnetic field, and the probe pulses are timed to arrive at the particular times in the RF cycle when the ground states are in the dark state. We are not concerned with adiabatic regimes in this work.

We are concerned with the *non-adiabatic* regime, where the switching time is very fast on the scale of optical pumping times, and all other relevant time scales, with the coupling field strength comparable to the spontaneous emission rate. The theoretical studies by Li and Xiao [15] and Zhu [16,17] assume (as we do) instantaneous switching and are therefore in the non-adiabatic regime, as are the two experimental observations in Λ systems [7,21] where the coupling field was rapidly switched using a Pockels cell. These studies were restricted to special cases of resonant fields and some specific detunings.

There has also been interest in a further non-adiabatic time regime where effects are studied on timescales comparable with the transition period, see for example [118] where the Rabi frequency of the coupling field was comparable to the transition frequency in a Galium-Arsenide semiconductor, and in the N-V centre of diamond [119] where RF transitions at the Rabi frequency were further driven by intense fields. Such regimes are quite different from those considered here as they go beyond conventional Bloch analysis of the atomic evolution.

5.2 Transient EIT in a lambda system

We now present the theory of non-adiabatic transient EIT in an ideal three-level Λ system. We are interested in the probe response as the coupling field is turned on and off non-adiabatically. All previous theoretical studies [15-17] have solved the master equations numerically in limited regimes to find the probe response. However, in some cases we have been able to solve these equations analytically using the Laplace transform, given some approximations. The use of the Laplace transform to obtain analytical results was developed by T. B. Smith in [52]. In this Section we present the main idea behind this method and results concerning our experiments.

5.2.1 The ideal three-level Λ system

We consider an ideal closed Λ system of three non-degenerate levels excited by monochromatic laser beams, as shown in Figure 5.1. The sample is assumed to be optically thin and so propagation effects are not considered. The atomic energy levels

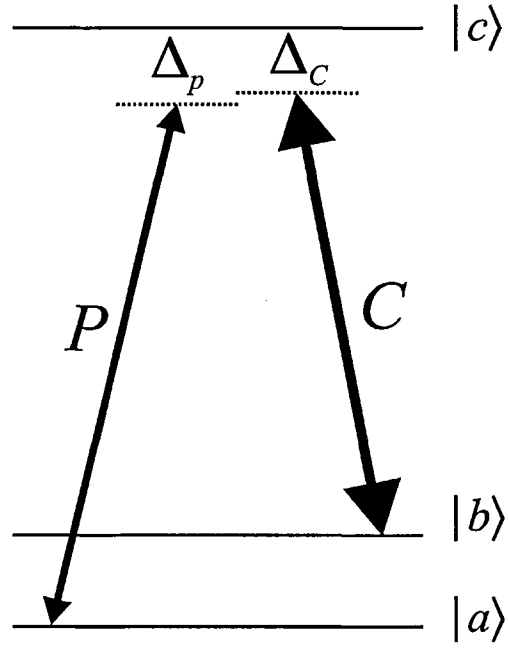

Figure 5.1 - Model energy level diagram.

are labelled in order of increasing energy $|a\rangle$, $|b\rangle$ and $|c\rangle$. The $|a\rangle-|c\rangle$ ($|b\rangle-|c\rangle$) transition is coupled by an optical field with frequency ω_p (ω_C) and detuning $\Delta_p=\omega_p-\omega_{ca}$ ($\Delta_C=\omega_C-\omega_{cb}$). The transition frequencies are defined $\omega_{\beta\alpha}=\omega_\beta-\omega_\alpha$, where α, $\beta=a$, b, c, and in our system $\omega_{ba}\ll\omega_{ca}$, ω_{cb}. For convenience we also define $\Delta_{pC}=\Delta_p-\Delta_C$. The state $|c\rangle$ is an excited state which decays by spontaneous emission to the ground (or metastable) states $|a\rangle$ and $|b\rangle$ at rates Γ_{ca} and Γ_{cb} respectively. There is assumed to be decay of the (two-photon) coherence on the $|a\rangle-|b\rangle$ transition at a rate Γ_{ba}, but no incoherent coupling between these two states. The Rabi frequency of field C (P) is $\Omega_C=\mathbf{d}_{cb}\cdot\mathbf{E}_C$ ($\Omega_p=\mathbf{d}_{ca}\cdot\mathbf{E}_p$) where $\mathbf{d}_{\alpha\beta}$ is the electric-dipole moment of the $|\alpha\rangle-|\beta\rangle$ transition, $\mathbf{E}_\gamma$ is the electric vector of optical field γ, and we have chosen units such that $\hbar=1$ so that energies are measured in units of frequency. Optical field C is the pump or coupling field and field P is the probe. For the purposes of this work we usually assume that the probe is weak, i.e. $\Omega_p\ll\Gamma_{ca}$ although the density matrix equations are presented without this assumption.

In the bare state basis, the density matrix equations of motion for the system in the rotating frame are those of (2.9), which we repeat here for convenience

$$
\begin{aligned}
\dot{\rho}_{aa} &= \Gamma_{ca}\rho_{cc} + i\frac{\Omega_p}{2}(\rho_{ca} - \rho_{ac}),\\
\dot{\rho}_{ab} &= \left(-i\Delta_{pC} - \Gamma_{ba}\right)\rho_{ab} + i\left[-\frac{\Omega_C(t)}{2}\rho_{ac} + \frac{\Omega_p}{2}\rho_{cb}\right],\\
\dot{\rho}_{ac} &= \left(-i\Delta_p - \frac{\Gamma_{ca}+\Gamma_{cb}}{2}\right)\rho_{ac} + i\left[-\frac{\Omega_C(t)}{2}\rho_{ab} + \frac{\Omega_p}{2}(\rho_{cc} - \rho_{aa})\right],\\
\dot{\rho}_{bb} &= \Gamma_{cb}\rho_{cc} + i\frac{\Omega_C(t)}{2}(\rho_{cb} - \rho_{bc}),\\
\dot{\rho}_{bc} &= \left(-i\Delta_C - \frac{\Gamma_{ca}+\Gamma_{cb}}{2}\right)\rho_{bc} + i\left[\frac{\Omega_C(t)}{2}(\rho_{cc} - \rho_{bb}) - \frac{\Omega_p}{2}\rho_{ba}\right],\\
\dot{\rho}_{cc} &= -(\Gamma_{ca}+\Gamma_{cb})\rho_{cc} + i\left[\frac{\Omega_C(t)}{2}(\rho_{bc} - \rho_{cb}) + \frac{\Omega_p}{2}(\rho_{ac} - \rho_{ca})\right],\\
\rho_{\alpha\beta} &= \rho^*_{\beta\alpha},\\
1 &= \rho_{aa} + \rho_{bb} + \rho_{cc}.
\end{aligned}
\tag{5.1}
$$

Because we measure probe absorption, which is proportional to $\mathrm{Im}[\rho_{ac}(t)]$, we concentrate on this component of the density matrix.

5.2.2 The Laplace transform method

The standard approach to solving (5.1) is to numerically integrate them (see for example [17]). This method has the advantage of conceptual ease and has been used to generate some of the theoretical turn-on results presented in this work. However this approach has the deficiencies that it is not analytic and therefore gives minimal insight into the underlying dynamics of the problem, and that it can suffer cumulative numerical errors. Accordingly, we have also considered a Laplace transform solution, which can avoid these difficulties. The Laplace method (in appropriate limits) is more amenable to analysis and in this work we present what we believe to be several new analytical results, especially the turn-off equations. We find an extra frequency of oscillation when the system responds to turning on the coupling field, and suggest the regime where this might be observable. Equations (5.1) are linear and so any solution depends only linearly on the initial conditions. This avoids the problem of cumulative

numerical errors, even when the Laplace method cannot easily produce simple explicit formulae, making the solutions more robust.

Any solution to (5.1) has the form

$$\rho_{\alpha\beta}(t) = \sum_l a_l e^{b_l t}. \tag{5.2}$$

Our goal therefore is to determine coefficients a_l and b_l. The difficulty lies in the fact that the coefficients depend on some or all of the system parameters, including Ω_C and Ω_p.

Defining the Laplace transform of $\rho_{\alpha\beta}(t)$ to be $r_{\alpha\beta}(p)$ we have [120]

$$r_{\alpha\beta}(p) = \int_0^\infty e^{-pt} \rho_{\alpha\beta}(t) dt, \tag{5.3}$$

and the transform of $\dot{\rho}_{\alpha\beta}(t)$ is $pr_{\alpha\beta}(p) - \rho^0_{\alpha\beta}$ where $\rho^0_{\alpha\beta} = \rho_{\alpha\beta}(0)$. Then (5.1) generate nine coupled algebraic equations for the $r_{\alpha\beta}(p)$. By manipulating these equations, one finds four closed equations for r_{bc}, r_{cb}, r_{ac}, and r_{ca}. For a full description of how the Laplace transform method is used, refer to [52].

We now present an application of the method to the transients following turn-on and turn-off of the coupling field. The solutions are provided to first order in the probe intensity, which corresponds to the experimental situation. For simplicity the turn-on expression is only given for resonant fields, however the turn-off result is presented for arbitrary detunings. This section ends with a graphical overview and discussion of the general turn-on and turn-off dynamics. To facilitate matters, at very little cost, we shall henceforth take $\Gamma_{cb}=\Gamma_{ca}=\Gamma/2$, which corresponds to the experimental case of Section 5.3.

5.2.3 Turn-on transient with resonant fields

We now outline how the Laplace transform method [52] is used to find $\mathrm{Im}[\rho_{ac}(t)]$ after the coupling field is turned on at time $t=0$. It is assumed that the probe has been on for some time in order to establish values for ρ_{aa}^0, ρ_{bb}^0 and $\rho_{ac}^0=(\rho_{ca}^0)^*$, which will be the only non-zero values of $\rho_{\alpha\beta}^0$. For a weak probe $\Omega_p \ll \Gamma$, we treat the problem to first order in the probe intensity. This corresponds to the experimental situation to be described in Sections 5.3 and onwards. We shall assume, for simplicity, that $\Gamma_{ba}=0$, although we shall restore a finite Γ_{ba} later on in this Section. Then for resonant excitation, i.e. $\Delta_C=\Delta_p=0$, we find, using *Mathematica*, that the Laplace transform of $\mathrm{Im}[\rho_{ac}(t)]$ to first order in Ω_p follows from

$$\frac{r_{ac}(p)-r_{ca}(p)}{2i}=\frac{\mathrm{Im}(\rho_{ac}^0)p}{p\Gamma/2+p^2+(\Omega_C/2)^2}+\frac{(\rho_{bb}^0-\rho_{aa}^0)\Omega_p/2}{p\Gamma/2+p^2+(\Omega_C/2)^2} -\frac{\Omega_p}{2}\frac{\rho_{bb}^0\Gamma/2+(\rho_{aa}^0-1)(p-\Gamma/2)+2\rho_{bb}^0 p}{p(p+\Gamma/2)(p+\Gamma)+(4p+\Gamma)(\Omega_C/2)^2}. \tag{5.4}$$

It is worth looking at the partial contribution given by the first term on the right hand side of (5.4), namely $\mathrm{Im}(\rho_{ac}^0)p/[p\Gamma/2+p^2+(\Omega_C/2)^2]$ for which the poles are

$$p=-\frac{\Gamma}{4}\pm i\frac{\sqrt{\Omega_C^2-(\Gamma/2)^2}}{2}. \tag{5.5}$$

The inverse transform is easily found to give

$$\mathrm{Im}[\rho_{ac}(t)]=\mathrm{Im}(\rho_{ac}^0)e^{-\Gamma t/4}\left[\cos\left(\frac{ft}{2}\right)-\frac{\Gamma}{2f}\sin\left(\frac{ft}{2}\right)\right], \tag{5.6}$$

where $f=\sqrt{\Omega_C^2-(\Gamma/2)^2}$. This result, which corresponds to damped Rabi nutation, was quoted in Section 2.1.2 and a similar result is given by Li and Xiao [15].

More generally, the contributions of ρ_{aa}^0 and ρ_{bb}^0 may not be ignorable, especially if Im(ρ_{ac}^0) is small or zero. Therefore we look at the full expression, (5.4), for which the first two terms are easily inverted. The denominator of the third term, however, is a cubic polynomial in p and can be somewhat complicated. However, as we are primarily interested in the case when the coupling field is strong, namely when $\Omega_C \gg \Gamma$, we can neglect terms of order Γ/Ω_C in these roots. This way, the roots p_1 and p_2 in the first two terms on the right hand side of (5.4) can be estimated as

$$p_1 = p_2^* \approx -\frac{\Gamma}{4} + i\frac{\Omega_C}{2}, \tag{5.7}$$

and those of the third term as

$$\begin{aligned} p_3 &\approx -\frac{\Gamma}{4}, \\ p_4 = p_5^* &\approx -\frac{5\Gamma}{8} + i\Omega_C. \end{aligned} \tag{5.8}$$

Note that p_1 and p_2 give rise to damped oscillations of angular frequency $\Omega_C/2$ as seen from (5.6), that p_3 yields a simple damped term, and that p_4 and p_5 give rise to damped oscillations of angular frequency Ω_C. Using these roots, it is a matter of algebra to derive the following approximation to Im[$\rho_{ac}(t)$]:

$$\mathrm{Im}[\rho_{ac}(t)] = \Phi_{12}(t) + \Phi_3(t) + \Phi_{45}(t), \tag{5.9}$$

where

$$\begin{aligned} \Phi_{12}(t) &\approx \left\{ \mathrm{Im}(\rho_{ac}^0)\cos\left(\frac{\Omega_C t}{2}\right) - \frac{\Gamma}{2\Omega_C}\left[(\rho_{aa}^0 - \rho_{bb}^0)\frac{2\Omega_p}{\Gamma} + \mathrm{Im}(\rho_{ac}^0) \right] \sin\left(\frac{\Omega_C t}{2}\right) \right\} e^{-\Gamma t/4}, \\ \Phi_3(t) &\approx -\frac{2\Omega_p}{\Gamma}\frac{12(1-\rho_{aa}^0)}{9+(8\Omega_C/\Gamma)^2} e^{-\Gamma t/4}, \\ \Phi_{45}(t) &\approx \frac{2\Omega_p}{\Gamma}\left[\frac{12(1-\rho_{aa}^0)}{9+(8\Omega_C/\Gamma)^2}\cos(\Omega_C t) + \frac{1-\rho_{aa}^0-2\rho_{bb}^0}{2}\frac{\Gamma}{2\Omega_C}\sin(\Omega_C t) \right] e^{-5\Gamma t/8}. \end{aligned} \tag{5.10}$$

We have compared, using *Mathematica*, the exact numerical inversion of (5.4) with the approximations in (5.10), i.e. $\Gamma_{cb}=\Gamma_{ca}=\Gamma/2$, $\Gamma_{ba}=0$ and $\Omega_p \ll \Gamma \ll \Omega_C$. The agreement is qualitatively good even for values of $\Omega_C \gtrsim \Gamma$.

In (5.9), $\Phi_{12}(t)$ is the contribution of the poles p_1 and p_2. That part of $\Phi_{12}(t)$ that is proportional to $\mathrm{Im}(\rho_{ac}^0)$ reduces to (5.6) in the limit $\Gamma/\Omega_C \to 0$. $\Phi_3(t)$ results from the pole at p_3 and is strictly monotonically decreasing with time. $\Phi_{45}(t)$ results from poles p_4 and p_5 and oscillates twice as fast as $\Phi_{12}(t)$.

In all the transient experimental and theoretical studies we know (including this present experimental study), the system behaviour is dominated by $\Phi_{12}(t)$; however, should $\mathrm{Im}(\rho_{ac}^0)$ be small or zero with approximately equal ground state populations (i.e. $\rho_{aa}^0 \approx \rho_{bb}^0$), then the faster oscillations of Φ_{45} might be observable. One way to do this would be to switch on *both* the probe and pump non-adiabatically at $t=0$. In this case we would have (in general) non-zero ρ_{aa}^0, ρ_{bb}^0 and $\rho_{cc}^0 = 1-\rho_{aa}^0-\rho_{bb}^0$, but vanishing off-diagonal components. A discussion of the faster oscillations using the 3-D Vector Model [66,67] appears in Appendix C.

Equations (5.6) to (5.10) were derived setting $\Gamma_{ba}=0$. In experimental realisations, a non-zero value of Γ_{ba} can result from collisions, trap inhomogeneities, laser linewidths, magnetic fields and other effects. We can generalise (5.6) including this dephasing, to yield

$$\mathrm{Im}[\rho_{ac}(t)] \approx \mathrm{Im}(\rho_{ac}^0)\left[\cos\left(\frac{f't}{2}\right)-\frac{\Gamma/2-\Gamma_{ba}}{f'}\sin\left(\frac{f't}{2}\right)\right]e^{-t(\Gamma/2+\Gamma_{ba})/2}, \qquad (5.11)$$

where $f'=\sqrt{\Omega_C^2-(\Gamma/2-\Gamma_{ba})^2}$. We can also obtain the general forms of (5.10) (for $\Omega_C \gg \Gamma$):

$$\Phi_{12}(t)=\mathrm{Im}\left(\rho_{ac}^{0}\right)\left[\cos\left(\frac{\Omega_C t}{2}\right)-\frac{\Gamma/2-\Gamma_{ba}}{\Omega_C}\sin\left(\frac{\Omega_C t}{2}\right)\right]e^{-t(\Gamma/2+\Gamma_{ba})/2}$$
$$+\frac{\Omega_p}{\Omega_C}\left[\left(\rho_{bb}^{0}-\rho_{aa}^{0}\right)\sin\left(\frac{\Omega_C t}{2}\right)+\frac{5\rho_{aa}^{0}+\rho_{bb}^{0}-2}{3}\frac{\Gamma_{ba}}{\Omega_C}\cos\left(\frac{\Omega_C t}{2}\right)\right]e^{-t(\Gamma/2+\Gamma_{ba})/2},$$
$$\Phi_{3}(t)=\frac{\Omega_p}{\Omega_C^2}\left[\frac{3\left(1-\rho_{aa}^{0}\right)}{4}\left(\Gamma/2-4\Gamma_{ba}\right)e^{-\Gamma t/4}-2\Gamma_{ba}\right], \tag{5.12}$$
$$\Phi_{45}(t)=\frac{\Omega_p}{\Omega_C^2}\left(\frac{3\left(1-\rho_{aa}^{0}\right)}{4}\Gamma/2+\frac{1-\rho_{aa}^{0}-2\rho_{bb}^{0}}{3}\Gamma_{ba}\right)\cos\left(\Omega_C t\right)e^{-5\Gamma t/8}$$
$$+\frac{\Omega_p}{\Omega_C}\frac{1-\rho_{aa}^{0}-2\rho_{bb}^{0}}{2}\sin\left(\Omega_C t\right)e^{-5\Gamma t/8}.$$

Note how the addition of Γ_{ba} has modified all three Φ components, adding terms to the amplitudes of the oscillations as well as their decay rates. This is an important result because, as mentioned before, our experiments were carried out with a non-zero Γ_{ba}.

We have not considered the case of non-resonant fields because it becomes too complicated. Instead we can numerically solve (5.1) to find the probe response in this case, as we shall see in Section 5.2.5 later on.

5.2.4 Turn-off transient for arbitrary detunings of pump and probe

The turn-off case is relatively simple as only the probe field acts during the transient period. Thus we are concerned with optical pumping by the probe with the appropriate initial conditions. We suppose that both the coupling and probe fields have been turned on for a time long compared to Γ^{-1} and the coupling field is then switched off at a time now taken to be $t=0$. Working to first order in Ω_p/Γ as before, we find with *Mathematica* that the inverse Laplace transform of $\rho_{ac}(t)$ is

$$r_{ac}(p)=\frac{1}{p+\Gamma/2+i\Delta_p}\left[\rho_{ac}^{0}+i\frac{\Omega_p}{2}\frac{(p-\Gamma/2)\left(1-\rho_{bb}^{0}\right)-\rho_{aa}^{0}(2p+\Gamma/2)}{p(p+\Gamma)}\right]. \tag{5.13}$$

The initial values ρ_{aa}^{0}, ρ_{bb}^{0} and ρ_{cc}^{0} are found by solving for the $r_{\alpha\beta}(p)$ during the epoch when both fields act, and then taking the long-time limits [52]. Thus we have

$$\begin{aligned}
&\rho_{aa}^{0}=1,\\
&\rho_{ac}^{0}=\frac{\Omega_p}{2}\frac{\Delta_{pC}-i\Gamma_{ba}}{\left(\Omega_C^2/4-\Delta_p\Delta_{pC}+\Gamma_{ba}\Gamma/2\right)+i\left(\Delta_{pC}\Gamma/2+\Delta_p\Gamma_{ba}\right)},\\
&\rho_{bb}^{0}=0,
\end{aligned} \tag{5.14}$$

so that,

$$r_{ac}(p)=\frac{1}{p+\Gamma/2+i\Delta_p}\left(\rho_{ac}^{0}-i\frac{\Omega_p}{p}\right), \tag{5.15}$$

This expression contains simple poles at $p=0$ and $p=-\Gamma/2-i\Delta_p$ so that for $t\geq 0$ one has

$$\rho_{ac}(t)\approx\rho_{ac}^{0}e^{-(\Gamma/2+i\Delta_p)t}-i\frac{\Omega_p}{2}\frac{1-e^{-(\Gamma/2+i\Delta_p)t}}{\Gamma/2+i\Delta_p}. \tag{5.16}$$

Finally, using (5.14) for ρ_{ac}^{0}, and taking the imaginary part of $\rho_{ac}(t)$, gives

$$\begin{aligned}
\mathrm{Im}\left[\rho_{ac}(t)\right]=&-\frac{\Omega_p}{2}\frac{\Gamma/2+e^{-\Gamma t/2}\left[\Delta_p\sin\left(\Delta_p t\right)-\frac{\Gamma}{2}\cos\left(\Delta_p t\right)\right]}{(\Gamma/2)^2+\Delta_p^2}\\
&-\frac{\Omega_p}{2}e^{-\Gamma t/2}\frac{\left[\Delta_{pC}^2\Gamma/2+\Gamma_{ba}\left(\Gamma_{ba}\Gamma/2+\Omega_C^2/4\right)\right]}{\left(\Gamma_{ba}\Gamma/2-\Delta_p\Delta_{pC}+\Omega_C^2/4\right)^2+\left(\Delta_{pC}\Gamma/2+\Delta_p\Gamma_{ba}\right)^2}\cos\left(\Delta_p t\right)\\
&-\frac{\Omega_p}{2}e^{-\Gamma t/2}\frac{\Delta_{pC}\left[\Omega_C^2/4-\Delta_p\left(\Delta_{pC}+2\Gamma_{ba}^2/\Gamma\right)\right]}{\left(\Gamma_{ba}\Gamma/2-\Delta_p\Delta_{pC}+\Omega_C^2/4\right)^2+\left(\Delta_{pC}\Gamma/2+\Delta_p\Gamma_{ba}\right)^2}\sin\left(\Delta_p t\right),
\end{aligned} \tag{5.17}$$

which is our analytical expression for the turn-off transient.

It is interesting to note that Γ_{ba} enters (5.16) and (5.17) only through the initial conditions. This may be understood by recalling that Γ_{ba} refers to a two photon dephasing, and so will not be dynamically important when only the probe field is acting. We note that, at $t=0$ (the instant of turn-off) one has, from (5.14) or (5.17),

$$\mathrm{Im}\left(\rho_{ac}^{0}\right)=-\frac{\Omega_p}{2}\frac{\Delta_{pC}^2\Gamma/2+\Gamma_{ba}\left(\Gamma_{ba}\Gamma/2+\Omega_C^2/4\right)}{\left(\Gamma_{ba}\Gamma/2-\Delta_p\Delta_{pC}+\Omega_C^2/4\right)^2+\left(\Delta_{pC}\Gamma/2+\Delta_p\Gamma_{ba}\right)^2}, \tag{5.18}$$

which is the general expression for the steady-state EIT lineshape for arbitrary detunings, obtainable from (2.10).

5.2.5 Overview of transient response

We now present an overview of the turn-on and turn-off transients for the ideal three-level system displayed as colour plots, showing $\mathrm{Im}[\rho_{ac}(t)]$ as a function of time t and probe detuning Δ_p. The parameters are chosen to correspond closely to the experimental conditions described in detail in the following sections. In order to generate the colour plots, we numerically turned on the probe field at a finite negative time ($t=-100\,\mathrm{ns}\approx 4\Gamma^{-1}$) that is sufficient to build up a steady state ρ_{ac}^{0}. Initial populations (at $t=-100\,\mathrm{ns}$) were chosen so that the populations at time $t=0$ corresponded closely to the experimental conditions ($\rho_{aa}(t=-100\,\mathrm{ns})=0.95$, $\rho_{bb}(t=-100\,\mathrm{ns})=0.05$). We then numerically solve (5.1) to find the probe response after $t=0$.

For the purpose of interpretation, we find it convenient to describe the transient behaviour in terms of the evolution of the system between one described by bare sates and one described by dressed states. The method for transforming between bare and dressed bases is given in [11].

The turn-on transients are shown in Figure 5.2(a) and (b), where the coupling field is switched on at $t=0$. We consider first the case of a resonant coupling field, Figure 5.2(a). Scanning the entire figure from left to right, we first see (for $t<0$) the Lorentzian probe absorption feature of spectral width Γ as the probe drives the bare $|a\rangle - |c\rangle$ transition. Then in the transient regime from $t=0$ to several Γ^{-1}, we find modified Rabi nutations due primarily to the coupling of the ground state $|a\rangle$ to the dressed states $|\pm\rangle = \left(|b\rangle \pm |c\rangle\right)/\sqrt{2}$. If the probe were to couple $|a\rangle$ to a single dressed state, say $|+\rangle$, it would undergo decaying Rabi oscillations at the detuned frequency $\sqrt{\left(\Delta_p - \Omega_C/2\right)^2 + \Omega_p^2}$. The peaks of these oscillations would lie on the curves

$\Delta_p = \pm 2\pi n/t + \Omega_C/2$ for $t \ll 2\pi/\Omega_p$ and n=1, 2, ... Oscillations of this kind are clearly evident in Figure 5.2(a) for each of the dressed states. However, the fact that the probe couples $|a\rangle$ to both dressed states simultaneously, evidently, results in *interference* between the Rabi oscillations due to the probe interacting with each dressed state separately. This suggests that the central pattern in Figure 5.2(a) represents transient dressed-state interferences. In addition, for $\Delta_p \approx 0$, the preparation of the system before the coupling field is switched on induces relatively strong absorption, and therefore a larger value of $\mathrm{Im}(\rho_{ac})$ at $t=0$. This leads to enhanced Rabi nutations along the $\Delta_p=0$ line for $t>0$. Finally, for long times, we see the two well-resolved absorption features, each of width $\Gamma/2$, corresponding to the well known Autler-Townes doublet [60]. We note that our colour plots show a superficial similarity to the three-dimensional plots presented by Lu *et al.* [13] but the different initial conditions between the two cases studied result in quite different dynamics.

We now focus on the case where the probe too is fixed on resonance, i.e. the time-line $\Delta_p=0$ in Figure 5.2(a). Here, for $t>0$, we see gain and absorption cycles of the kind discussed in refs [15,17]. For a strong coupling field ($\Omega_C/\Gamma \gg 1$) this transient ($\Delta_p=0$) is well described by (5.11). Two other lines of note are at $\Delta_p = \pm\Omega_C/2$ where transparency for $t<0$ changes transiently to absorption as the probe begins to resonantly monitor a transition to a dressed state.

Figure 5.2(b) shows the case of a detuned coupling field. Again, we observe a transient regime featuring absorption and gain regions evolving to the resolved dressed state absorption features centred at $\Delta_p = \Delta_C/2 \pm \sqrt{(\Omega_C^2 + \Delta_C^2)/4}$, but in this case we can clearly distinguish between the dominant or major dressed state and the narrower minor dressed state. In the bare state picture, in the limit of large Δ_C these two features are

associated, respectively, with one-photon absorption ($|a\rangle \rightarrow |c\rangle$) and two-photon absorption ($|a\rangle \rightarrow |c\rangle \rightarrow |b\rangle$).

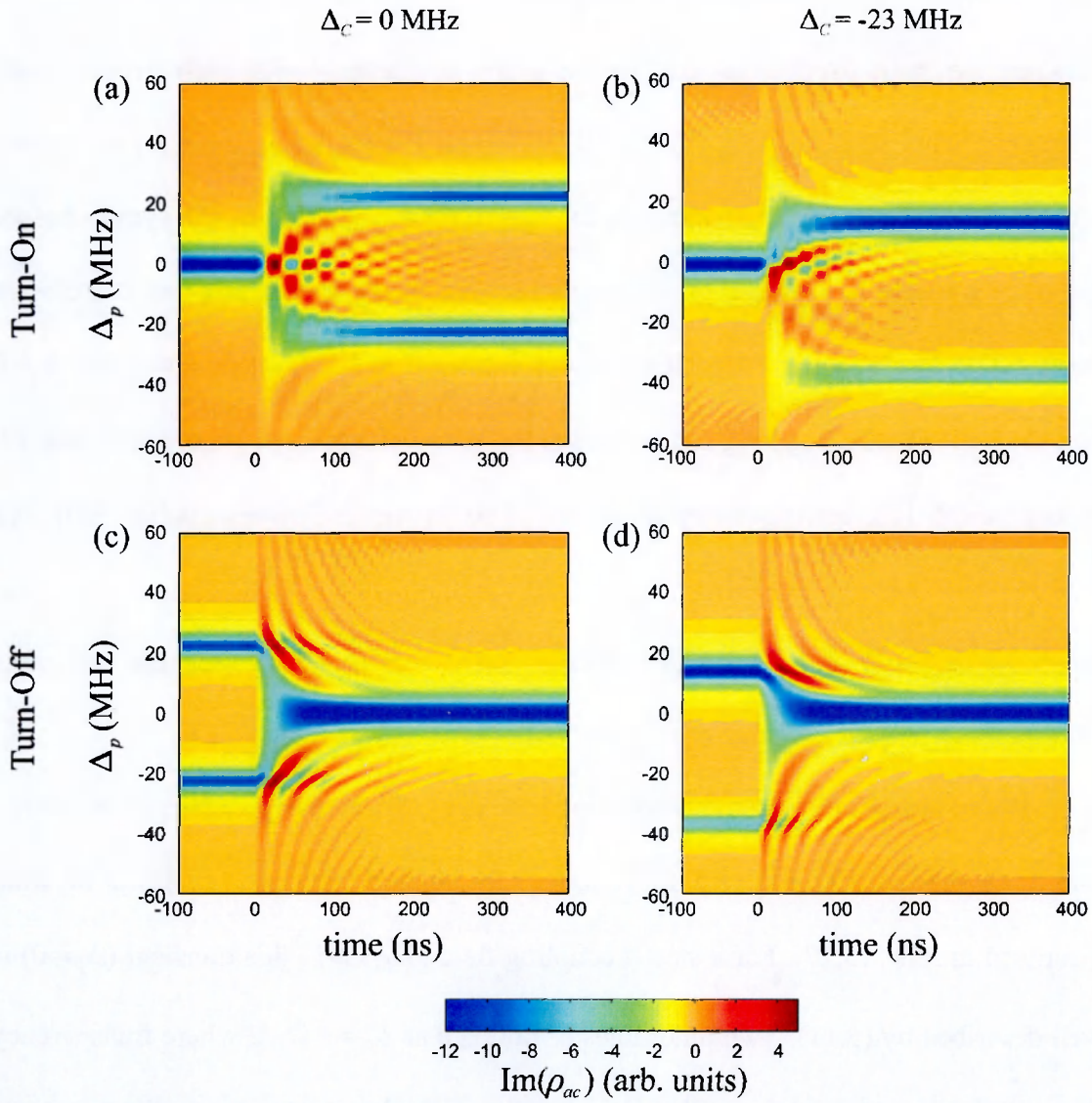

Figure 5.2 - Colour plots of $\mathrm{Im}[\rho_{ac}(t)]$ as a function of time, t, and probe detuning, Δ_p for (a) turn-on, resonant coupling field: Δ_C=0 MHz; (b) turn-on, detuned coupling field: Δ_C=−23 MHz; (c) turn-off, resonant coupling field: Δ_C=0 MHz; and (d) turn-off, detuned coupling field: Δ_C=−23 MHz. In all cases we have used: Ω_C=45 MHz, Ω_p=1 MHz, Γ=5.68 MHz and Γ_{ba}=3.4 MHz. (The effect of uncoupled absorptions are not included in these plots.)

We now consider the turn-off transients shown in Figure 5.2(c) and (d), where both fields are assumed to have been on for all negative times to establish the initial conditions, and the coupling field is switched off at t=0. The dominant feature in the transient regime is the $1/t$ broadened absorption region where the probe begins to drive

the bare transition. Of more interest are the strong transient gain peaks that can be seen along the two lines $\Delta_p = \Delta_C/2 \pm \sqrt{(\Omega_C^2 + \Delta_C^2)/4}$ at the levels associated with the two dressed state transitions before turn-off. This is simply the off-resonant probe monitoring the relaxation of a two-level atom with specially prepared initial conditions. We note that these transient gain regions are tunable by varying the detuning and strength of the coupling beam, and are remote from any uncoupled absorptions that might exist in a real Λ system around the Δ_p=0 region (see [29] and Section 5.3.2). We note also that the entire (t, Δ_p) region of this Figure is described by (5.17).

A detailed comparison between the theoretical and experimental results for selected horizontal lines (constant Δ_p) on Figure 5.2 will be presented in Sections 5.4 and 5.5.

5.3 Experimental set-up and the Rb system

In this Section we describe our experimental arrangement for transient EIT experiments in the real ^{87}Rb Λ system in our MOT. In an experimental realisation like this one, it is necessary to take into account not only the behaviour of the ideal model (Figure 5.1), but also the light shifts due to off-resonant interactions with other nearby hyperfine levels, and the effects of level degeneracies which lead to uncoupled absorption of the probe. The origins of uncoupled absorptions are described in this Section.

5.3.1 Experimental set-up and procedure

The lambda system we have studied is formed by the weak probe field P and the strong coupling field C shown in Figure 5.3. The ^{87}Rb sample was cooled in the MOT

system previously described in Section 4.3. It contained about 5×10^7 atoms in a region of diameter about 3 mm.

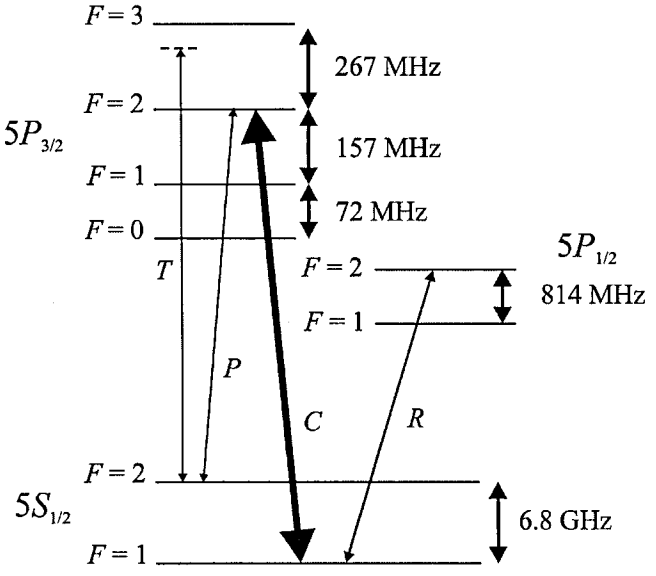

Figure 5.3 - The ^{87}Rb system in which the experiments are carried out.

The coupling beam C has an average intensity of $\approx$100 mW/cm^2 in a roughly elliptical profile of 2 mm×4 mm and is detuned by a variable amount Δ_C from the $5S_{1/2}(F=1)$ to $5P_{3/2}(F=2)$ transition. This detuning was achieved by locking the master lasers to a well-defined crossover in the saturated absorption spectrum and then shifting the master laser frequency using an acousto-optical modulator to provide a well-defined frequency.

The probe beam P has an average intensity $\approx$0.03 mW/cm^2 in a diameter $\approx$1 mm. It can be locked to or scanned across the $5S_{1/2}(F=2)$ to $5P_{3/2}(F=2)$ transition by varying the cavity size of the external-cavity grating-controlled diode laser (ECDL) using the voltage offset of the PZT, which was monitored on a voltmeter. This voltage was calibrated using the saturated absorption spectrum in a standard Rb cell (see Figure 5.4(a)). Drifts in the cavity size due to temperature fluctuations were checked and corrected for by determining the voltage that put the probe field on resonance at the

beginning of each transient experiment, as shown on Figure 5.4(b). Nevertheless, the absolute detuning of the probe field could not be determined to an accuracy better than about half a linewidth (≈3 MHz), except when the field was locked to resonance. Standard detunings used were generally much larger than 3 MHz, with dressed state detunings being as large as 36 MHz. The measured transients were stored in a Tektronix TDS520B digital oscilloscope. Instabilities in our control method limited the maximum number of averages to about 50.

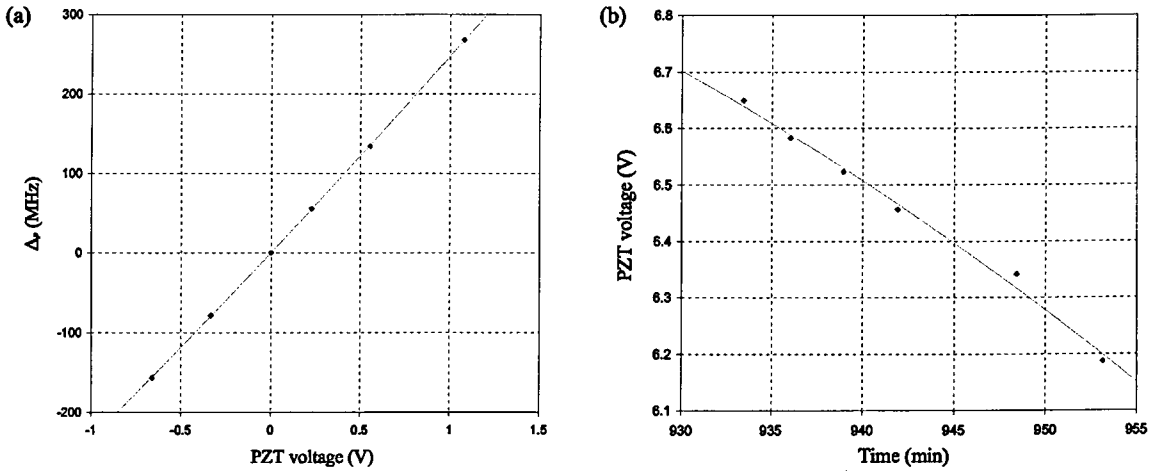

Figure 5.4 - Detuning calibration plots, showing (a) Δ_p vs. PZT voltage offset for a saturated absorption trace, and (b) voltage drift of a saturated absorption peak in time.

Our experiments were carried out in the optically thin regime with maximum probe absorption of about 15% at resonance. The probe Rabi frequency of about 4 MHz gave a good signal to noise ratio without producing any measurable power broadening. Under these conditions the probe absorption increases linearly with probe intensity and it was found convenient to normalise our probe absorption/transmission levels to the steady state absorption in the absence of the coupling field. We define the maximum probe absorption in the absence of a coupling field as the zero transmission level. Thus, if we define the voltage measured on our photodetector as $\mathcal{V}$, the signal for maximum probe absorption (minimum probe transmission) $\mathcal{V}_{min}$ and the signal without any probe absorption $\mathcal{V}_0$, then our scaled transmission levels for a detected signal are defined by

$$T = \frac{\mathcal{V} - \mathcal{V}_{min}}{\mathcal{V}_0 - \mathcal{V}_{min}}. \tag{5.19}$$

This definition for the transmission has the advantage of being simple and robust against day-to-day fluctuations in the number of atoms trapped in our sample (provided we are in a linear absorption regime). It is also easy to make direct comparisons with theory by noting that any detected changes in signal level will be proportional to $\mathrm{Im}(\rho_{ac})$, with values of $T>1$ associated with gain and $T<1$ indicating absorption. Because of small drifts in the intensities of our laser diodes (which were run in constant current mode for maximum frequency and mode stability), probe transmission levels were measured with the MOT turned off between transient runs and the transmission level at the time of the experiment inferred using a linear regression. This introduced errors in the transmission levels making these lower than zero for maximum absorption and larger than one for total transparency in some cases.

A schematic showing the layout of coupling and probe beams is shown in Figure 5.5. The beams propagated in the sample with orthogonal linear polarisations and with an angle of about 20° between their directions of propagation, which was found to give a good overlap of the probe with the coupling field in the cold sample.

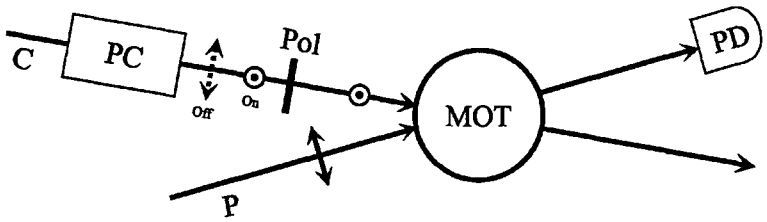

Figure 5.5 - Schematic of the experimental arrangement showing the relevant beams and their polarisations. *PD* is an avalanche photodiode, *PC* is a Pockels cell, *Pol* is a polariser. The trapping and repumping fields are not shown for clarity.

Non-adiabatic switching of the coupling field was realised using a Gsänger LM10 Pockels cell with a custom designed high voltage switch, which is driven by a pulse 10 μs long with a repetition rate of 10 Hz. The rise time of the switch and associated

detection circuitry was less than 6 ns, as shown in Figure 5.6. The excited $5P_{3/2}$ state lifetime is 28 ns and the relevant Rabi periods are of similar magnitude and so the non-adiabatic condition is fairly well satisfied. Because the fall time of the switch is very long, the Pockels cell could only be operated in either fast turn-on or fast turn-off mode, necessitating separate experiments to observe turn-on and turn-off transients. As the Pockels cell is switched on, it rotates the polarisation of the coupling beam, which then passes through a polariser that selects only the rotated polarisation (see Figure 5.5), hence switching on and off the coupling beam. Changing between turn-on and turn-off experiments was realised by rotating the plane of polarisation of the coupling field by 90° before entering the Pockels cell.

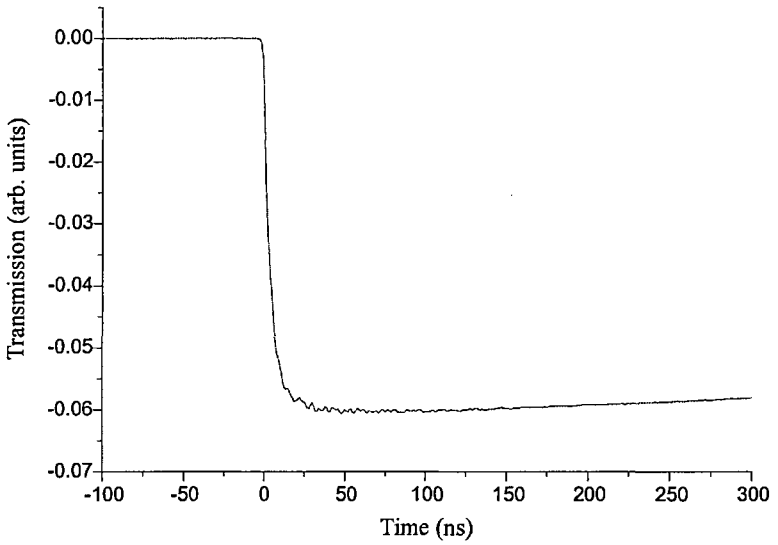

Figure 5.6 - Coupling field transmission as a function of time showing the switching of the Pockels cell.

5.3.2 Zeeman degeneracies and uncoupled absorptions

Many manifestations of Zeeman degeneracy have been reported in EIT experiments: optical pumping among Zeeman levels and to other levels [39], coherent population trapping by the coupling beam [35], the inversion of EIT dips (i.e. electromagnetically induced absorption) [121], and absorption of the probe beam on

Zeeman transitions that are not coupled by the coupling beam [122]. These latter uncoupled absorptions are a constant feature of our probe spectra, superimposed on the Λ system spectra we are interested in.

Figure 5.7 illustrates the individual Zeeman states of the hyperfine levels coupled by the probe P (fine lines) and coupling field C (thick lines). The quantisation axis in Figure 5.7(a) has been taken to be along the polarisation of P. Also shown in Figure 5.7 are the corresponding Clebsch-Gordan coefficients. The states $|m\rangle_X$ are labelled in terms of the magnetic quantum number m and X, where X is one of a, b or c which correspond to the $5S_{1/2}(F=2)$, $5S_{1/2}(F=1)$ and $5P_{3/2}(F=2)$ levels respectively in Figure 5.3.

Figure 5.7 shows that the coupling field C (thick lines) alone provides a doubly-driven V configuration as well as a separate quadruply-driven 'W' configuration. Taking account of the additional states coupled by P it appears that a seven-state (Figure 5.7(b)) and, separately, a five-state (Figure 5.7(c)) model are necessary to describe the dynamics of the experiment. The state $|0\rangle_a$ does not interact with any fields. However, it can be shown [29] that, with the following change of basis

$$\begin{aligned} |m,\pm\rangle_X &\equiv \frac{1}{\sqrt{2}}\left(|m\rangle_X \pm |-m\rangle_X\right), \\ |\alpha\rangle_c &\equiv \frac{1}{2}|0\rangle_c + \frac{\sqrt{3}}{2}|2,+\rangle_c, \\ |\beta\rangle_c &\equiv \frac{\sqrt{3}}{2}|0\rangle_c - \frac{1}{2}|2,+\rangle_c, \end{aligned} \tag{5.20}$$

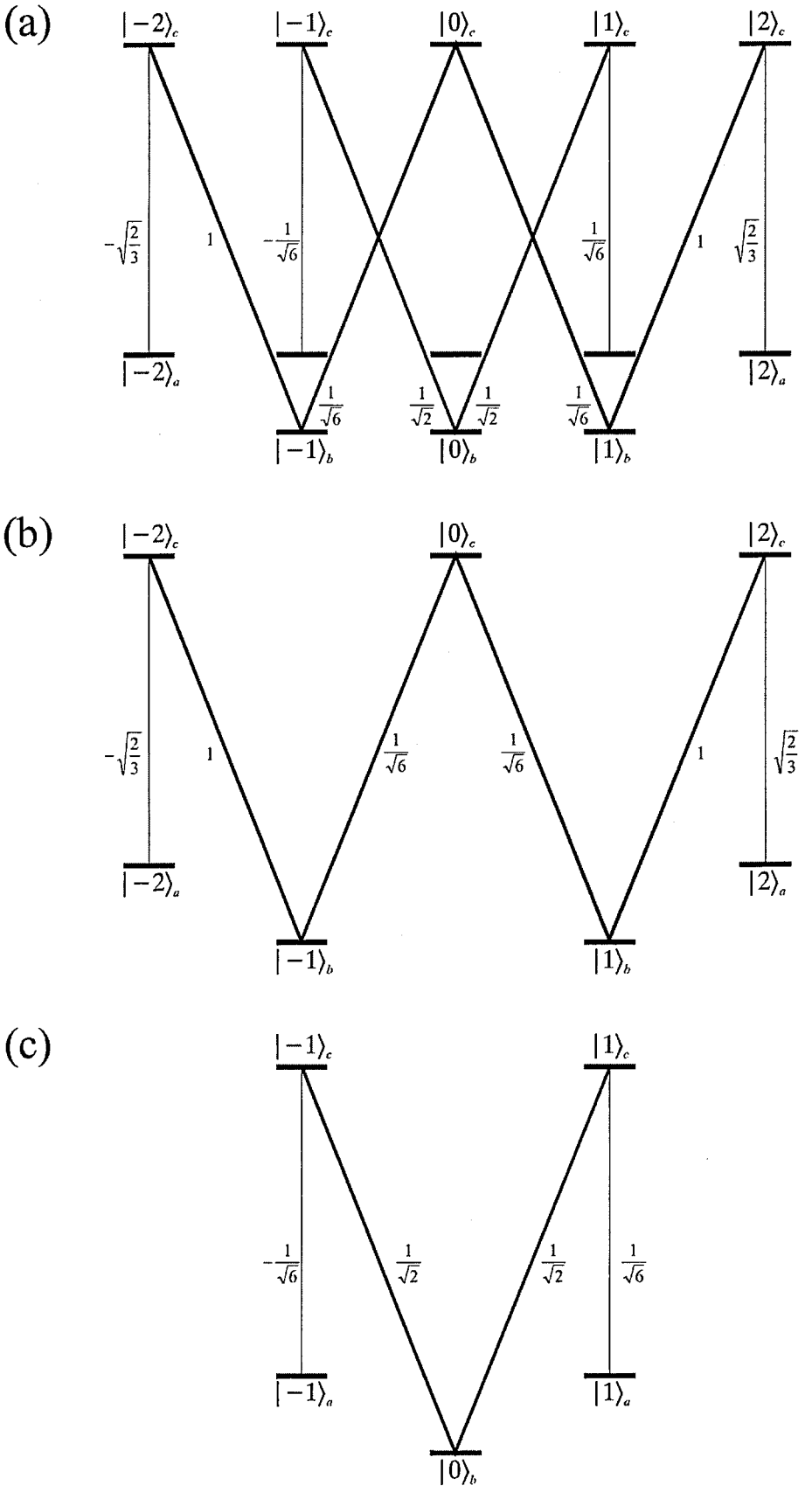

Figure 5.7 - Zeeman states, coupled transitions and Clebsch-Gordan coefficients in the (a) whole system (b) the seven-state system and (c) the five-state system. The fields *P* and *C* are represented respectively by thin lines and thick lines.

this complex structure reduces to sets of simple coupled systems. Figure 5.8 shows the transitions in this new basis. Three Λ systems, of the type shown in Figure 5.1, are clearly evident in the new basis. Also shown are the effective Clebsch-Gordan coefficients for the new transformed transitions. The dashed lines in Figure 5.8 represent transitions probed by field *P* but not directly coupled by the coupling field *C*. They correspond to what are called uncoupled absorptions of the probe.

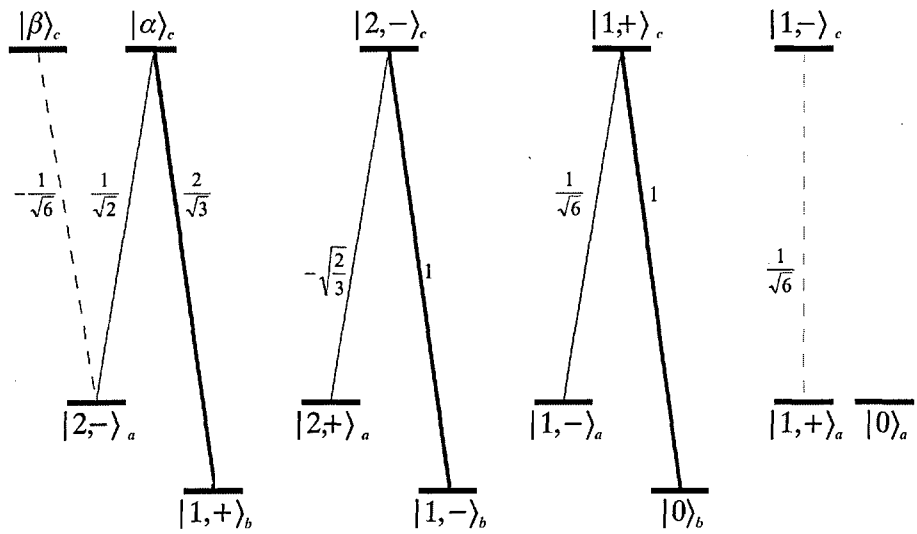

Figure 5.8 - Zeeman states, coupled transitions and Clebsch-Gordan coefficients in the new basis, showing the uncoupled absorptions (dashed transitions). Three separate Λ systems are clearly visible in the new basis. The fields *P* and *C* are represented respectively by thin lines and thick lines.

The four coupled states on the left of Figure 5.8 show that the (relatively weak) field *P* simultaneously probes a Λ system as well as the uncoupled $|2,-\rangle_a \rightarrow |\beta\rangle_c$ transition. This uncoupled transition simply causes additional absorption and scattering of field *P* and so, essentially, this four-state system can be treated as an ideal three-state Λ system (as shown in Figure 5.1) with an additional uncoupled absorption. Thus, the underlying probe absorption profile is due essentially to three separate Λ systems (solid lines) with two uncoupled absorptions (dashed lines).

Each Λ system has a different set of (effective) Clebsch-Gordan coefficients, and so the Rabi frequencies for the fields *P* and *C* differ from one Λ system to the next.

Since the position of the peaks in the steady-state probe absorption spectrum depend on the Rabi frequency of C, the absorption peaks due to each Λ system occur at different probe detunings. However, these differences are relatively small, corresponding to about a 10% shift in the separation of Autler-Townes peaks. A *single* three-state model, as given in Section 5.2, is therefore sufficient to model our experiment, provided we allow for broadened absorption peaks and uncoupled absorptions.

The square of Clebsch-Gordan coefficients of the dashed transitions, giving the uncoupled absorptions, is 1/6. We can compare this with the different polarisation scheme in which all fields are linearly polarised along the same axis. In this case there are two uncoupled absorption transitions from $|\pm 2\rangle_a$ to $|\pm 2\rangle_c$ for which the square of the corresponding Clebsch-Gordan coefficients is 2/3. That is, the absorption of the uncoupled transitions in the parallel-linear polarisation scheme is *four times* that of our orthogonal-linear polarisation scheme for the same degree of occupation. This clearly shows the advantage of our choice of polarisation scheme, assuming the $5S_{1/2}(F=2)$ Zeeman sublevels are equally populated. In our experiment, new atoms are continuously moving into and out of the (trapping) interaction region, the trapping magnetic fields produce Zeeman mixing amongst ground states and the trapping field weakly couples the $5S_{1/2}(F=2)$ level to the upper $5P_{3/2}(F=3)$ level. All these effects tend to redistribute population amongst the states of the $5S_{1/2}(F=2)$ level. The treatment of these effects to calculate the relative occupations of the $5S_{1/2}(F=2)$ states is, however, beyond the scope of this work. Thus, while we can identify the transitions responsible for the uncoupled absorptions and justify our polarisation scheme, we have no quantitative estimates of the strength of the absorptions. In our turn-on experiments, uncoupled absorptions were found to contribute about 20% of the maximum resonant absorption and are assumed to have a Lorentzian line shape centred at zero probe detuning.

Finally we note that state $|0\rangle_a$, uncoupled by any field, is a dark state. In an ideal system, all atoms would eventually decay to this state and so the steady state would be one of complete transparency of the probe field. However, the above mechanisms which tend to redistribute the population of the $5S_{1/2}(F=2)$ level will also tend to depopulate the state $|0\rangle_a$.

5.4 Effects of the coupling field Rabi frequency

We first carried out a study of the effects of the coupling field Rabi frequency in turn-on transient experiments when both fields are resonant. This study is an extension of the work carried out previously in this laboratory [7,8], taken to large coupling field strength where Rabi oscillations and transient gain can be observed.

5.4.1 Steady-state calibration traces

Figure 5.9(a) shows the steady state EIT absorption spectra for different coupling field Rabi frequencies as the probe beam is scanned across the $5S_{1/2}(F=2)$ to $5P_{3/2}(F=2)$ transition and the coupling beam remains on. We have used these traces to calibrate various parameters for the transient traces presented in Figure 5.9(b). As explained above, each steady-state spectrum consists essentially of a central uncoupled absorption peak (labelled *U*) situated between the two Autler-Townes peaks of an EIT profile (labelled 1 and 2). We measured the separation of the Autler-Townes peaks to yield a calibration of Ω_C.

Because *C* is a strong field, it interacts with neighbouring transitions (mainly the $5S_{1/2}(F=1)$ to $5P_{3/2}(F=1)$), causing a light shift on the $5S_{1/2}(F=1)$ level of the sample with respect to the same level in the saturated absorption cell. For this reason, *C* had to

be detuned with respect to the saturated absorption transition in order to keep it resonant with the transition in the sample. This light shift varied with Ω_C with a maximum value of 7 MHz.

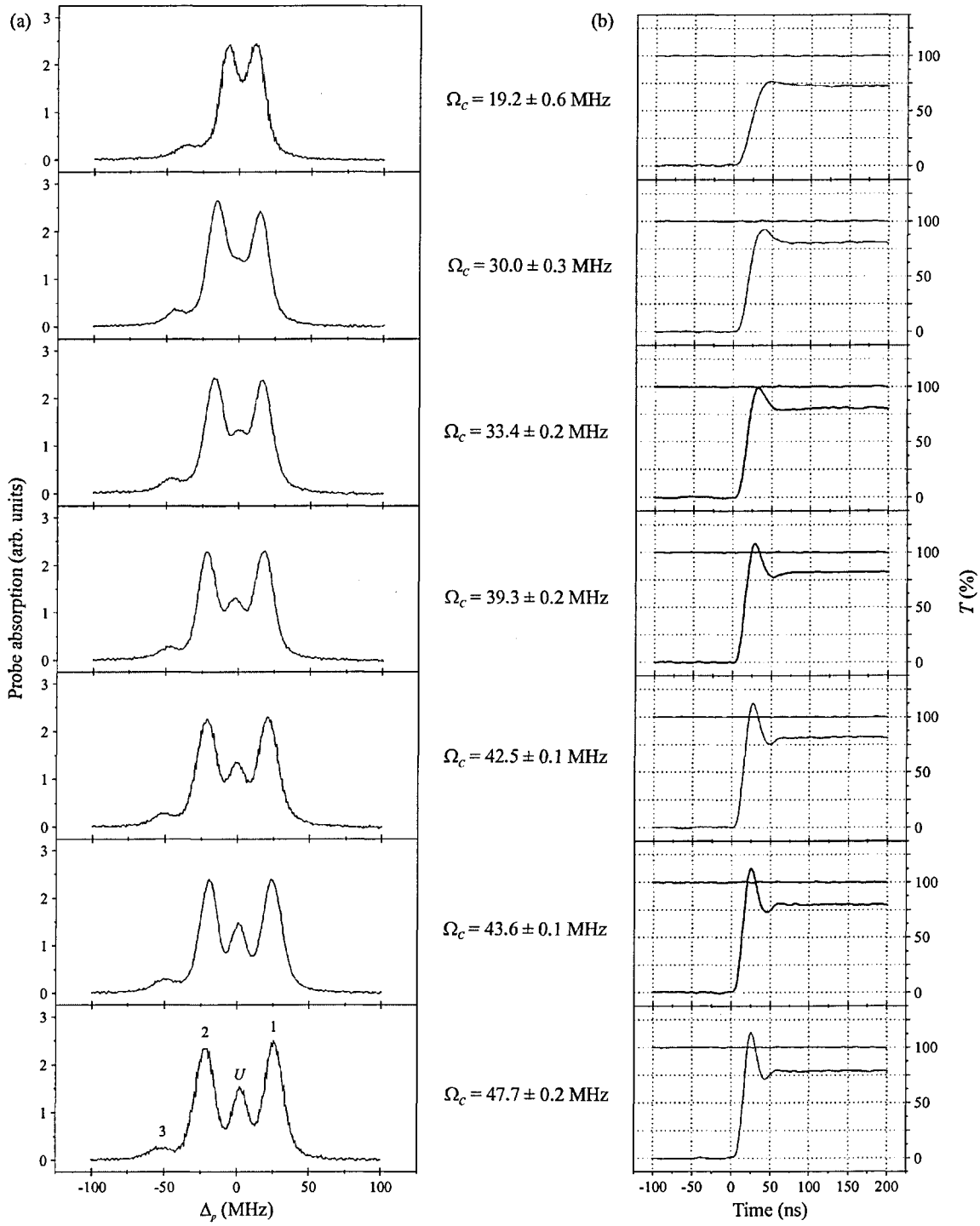

Figure 5.9 - (a) Steady state probe absorption spectra. (b) Probe transient transmission traces as *C* is turned on at time *t*=0. The peaks labelled 1 and 2 correspond to the main Autler-Townes peaks, peak 3 is the small V-type EIT peak, and *U* is the uncoupled absorption peak. Each trace is an average over 200 scans.

Furthermore, the trapping beams T act as a detuned coupling field with P in a V-type EIT configuration, as can be seen from Figure 5.3. This splits each of the three peaks into two, one of which is very much larger than the other because T is detuned by -13 MHz. The light-shifted peaks are the ones clearly visible in the traces shown in Figure 5.9(a). Of the smaller peaks, only the one corresponding to the red-detuned Autler-Townes peak is visible in these traces (labelled 3). It was also necessary to shift the frequency of P by 4 MHz to take account of these light shifts caused by the trapping beams T.

Finally, we note that the broad linewidths of our spectra are a consequence of broadening effects due to beam profile inhomogeneities, variations of Clebsch-Gordan coefficients between the different Zeeman transitions mentioned before, the spread of intensity in the standing wave field of the counter-propagating trapping beams in the MOT which causes a spread in the detuning of the probe field due to the spatially varying light shifts, and finally Zeeman splitting due the MOT's magnetic field gradient.

5.4.2 Transient traces

The transient traces in Figure 5.9(b) were obtained with the fields locked to their corresponding transitions of the cold sample, as described above. The absolute steady-state probe absorption without the coupling field is $\approx$20%.

Figure 5.9(b) shows the probe transient transmission (5.19) when C is turned on at time $t=0$ for various coupling field Rabi frequencies Ω_C. It is to be noted that the probe transmission relaxes approximately to the 80% level instead of the 100% level as predicted by [15-17]. This is mainly due to the uncoupled absorption peak and, to a lesser degree, dephasing mechanisms and inhomogeneities which reduce the visibility

of the transparency window, as seen in the respective steady state EIT traces in Figure 5.9(a).

An important feature of these traces is the development of a whole cycle of Rabi oscillation for the largest coupling field strengths used. The fact that only one whole Rabi cycle is seen, is mainly because of the line-broadening caused by the spread in trapping beam intensities mentioned above. This is in good agreement with our model when the spread in trapping beam intensity is taken into account.

Despite the limiting effects of uncoupled absorptions and line-broadening, it is possible to see as much as 15±5% gain for maximum Ω_C, and an increase in the frequency of the Rabi cycle with Ω_C as predicted by the theory (see Figure 5.2). Figure 5.10 shows the maximum transmission T_{max} at the peak of the Rabi cycle as a function of Ω_C. Gain (T>100%) is seen in this plot after a threshold Rabi frequency of $\Omega_C \approx 33$ MHz. Numerically subtracting the effects of the uncoupled absorptions would yield a maximum gain ≈45% and a significantly lower threshold Rabi frequency. The

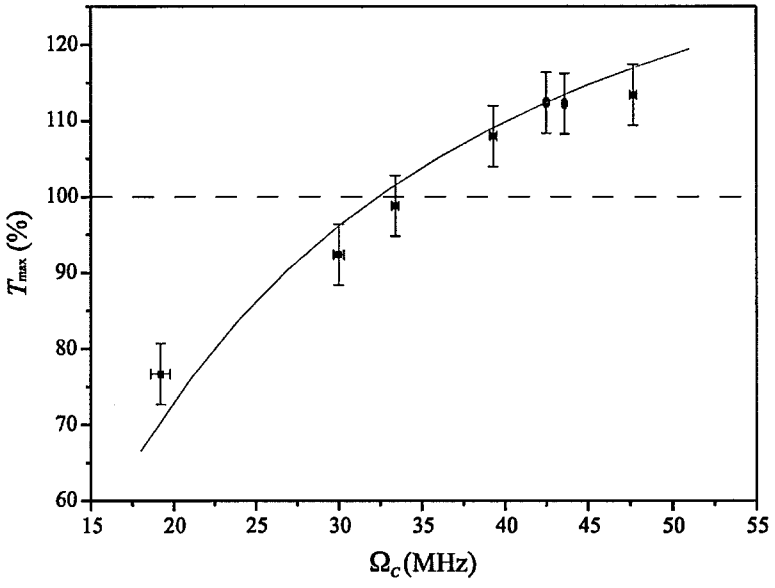

Figure 5.10 - The height *h* of the first Rabi cycle peak plotted against Ω_C when *C* is locked to the light-shifted transition of the atoms in the MOT. The solid line is a theoretical model.

solid line in Figure 5.10 corresponds to a theoretical expectation derived from our three-level atom model with an initial population distribution of 75% in the $5S_{1/2}(F=2)$ and 25% in the $5S_{1/2}(F=1)$ ground levels, as established from independent absorption measurements. Our computations show that for these initial conditions there is no inversion at any time on either the one photon probe transition or the two-photon transition $5S_{1/2}(F=1)\rightarrow 5P_{3/2}(F=2)\rightarrow 5S_{1/2}(F=2)$, and so this is transient probe gain without population inversion in the bare state basis.

Theoretical modelling of our system was performed by numerically integrating the density matrix equations of motion presented earlier and incorporating the spread of probe detunings due to the spatial variation in the light shifts induced by trapping fields. It is difficult to fully model this spread in trapping field intensity as the standing wave pattern is critically dependent on the slowly varying, but unknown, relative phases of the component fields of the trapping beams (for a full description of these effects see [87,97]). Experimentally, the mean light shift was corrected by shifting the frequency of the probe field accordingly, while in the numerical models, a truncated Lorentzian distribution of detuned probe fields was found to give good agreement with the experimental results.

5.5 Resonant and non-resonant switching

In this Section, we present experimental turn-on and turn-off transients for the resonant and the non-resonant coupling and probe fields, together with the corresponding theoretical curves. Turn-on theory transients were obtained by numerically solving (5.1). Turn-off theory transients were obtained by fitting the

experimental data to (5.17). In each case representative selections of probe detunings are chosen so that horizontal lines across Figure 5.2(a)-(d) are explored.

For the most part our theoretically fitted values of Δ_p agree within ± 3 MHz with those determined using the piezo offset of the probe cavity. In a small number of experiments (Figure 5.14(c) and (d)), we discovered larger discrepancies, which we attribute to the presence of a frequency jump of the probe laser. Because we were aware that this procedure is susceptible to errors caused by probe laser frequency jumps, we have presented values of Δ_p obtained by fitting the theory to the experimental results. It has been less easy to make direct comparisons of the overall transmission levels and there are minor inconsistencies when comparing experimental with theoretical levels in our transients. We believe that these inconsistencies are due to difficulties in correcting for all of the intensity fluctuations and drifts in our lasers on the timescales of our experiments, especially as they relate to probe laser mode hops.

As in Section 5.4, we begin by presenting the corresponding steady-state EIT spectra.

5.5.1 Steady-state calibration traces

We first present experimental steady-state probe frequency spectra (EIT traces) for a resonant and a non-resonant coupling field with the same parameters that apply in the transient experiments. The central region of Figure 5.11(a) shows the probe spectrum for the resonant coupling field, similar to those in Figure 5.9(a). The dressed state absorption peaks are clearly resolved on either side of the uncoupled absorption at $\Delta_p=0$. The Rabi frequency of the coupling field can be inferred from this Figure to be $\Omega_C=45$ MHz. This value is consistent with that obtained from beam parameters and absorption line strengths. Also seen in Figure 5.11(a) are the absorption peaks on the

$5S_{1/2}(F=2)$ to $5P_{3/2}(F=1)$ transition at $\Delta_p=-157$ MHz and the $5S_{1/2}(F=2)$ to $5P_{3/2}(F=3)$ transition at $\Delta_p=267$ MHz. These peaks were used for frequency calibration purposes. Figure 5.11(b) shows the probe spectrum when the coupling field is detuned by $\Delta_C=-23$ MHz. The major dressed state absorption peak is seen at $\Delta_p=14$ MHz and the minor one at $\Delta_p=-37$ MHz. Uncoupled absorptions are barely resolved in the wing of the major dressed state. We note again that the linewidths in these spectra are approximately 11 MHz, or nearly twice the spontaneous decay rate of the $5P_{3/2}$ levels, due to the inhomogeneities mentioned earlier. Accordingly we have taken a phenomenological value for the linewidth of $\Gamma=11$ MHz in our theoretical transients rather than the standard value of 5.68 MHz. Our transient theory (Section 5.2) assumes a branching ratio of unity, i.e. $\Gamma_{cb}=\Gamma_{ca}=\Gamma/2$. This is appropriate here because the total decay rate of each of the excited $5P_{3/2}(F=2)$ states branches equally to the ground $5S_{1/2}(F=2$ and $F=1)$ manifolds. The two-photon dephasing rate is taken to be $\Gamma_{ba}=0.3\Gamma$ [7,8].

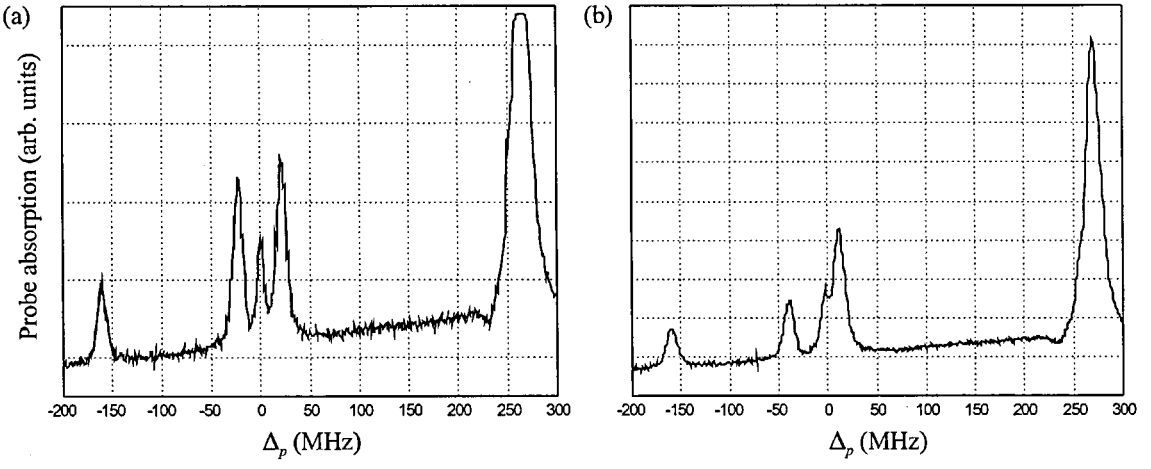

Figure 5.11 - Steady state probe transmission spectra. (a) On-resonance coupling field with Rabi frequency $\Omega_C=45$ MHz. (b) Off-resonant coupling excitation with Rabi frequency $\Omega_C=45$ MHz and detuning $\Delta_C=-23$ MHz. Each trace is an average over 50 scans. Day to day fluctuations in signal levels mean that the absorption scales in (a) and (b) are different.

5.5.2 Switching on the coupling field

For these experiments the coupling field is turned on at time $t=0$, after the probe field and MOT fields have been on for a long time.

Resonant coupling field

The left-hand traces in Figure 5.12(a)-(c) show the experimental results for turning on a resonant coupling field ($\Delta_C=0$) of Rabi frequency $\Omega_C=45$ MHz, for various probe field detunings (essentially, we are exploring horizontal lines of Figure

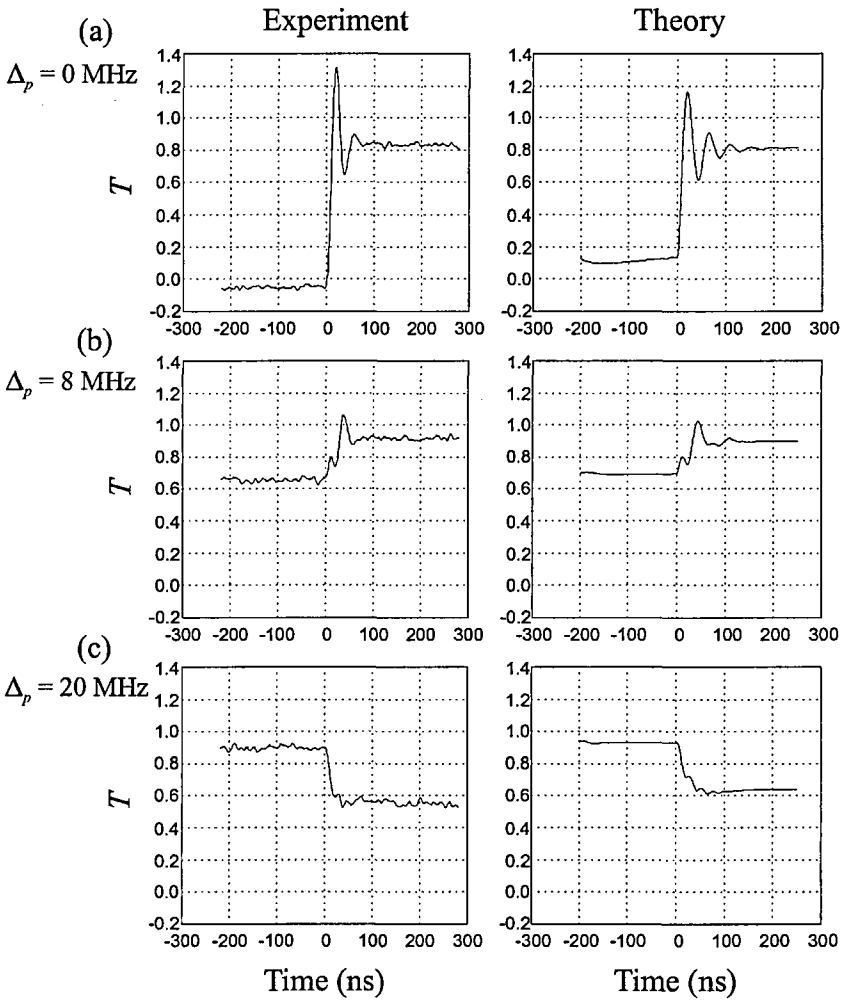

Figure 5.12 - Turn-on transients for varying probe detunings with a resonant coupling field: (a) $\Delta_p=0$ MHz (resonant probe), (b) $\Delta_p=8$ MHz, and (c) $\Delta_p=20$ MHz (dressed state filling). In all cases $\Omega_C=45$ MHz, 50 averages were taken.

5.2(a)). The right hand traces show the corresponding theory curves, with the steady transmission levels adjusted to take account of the uncoupled absorption. Figure 5.12(a) shows the well-known case of zero probe detuning ($\Delta_p=0$) exhibiting significant gain ($T=1.35$) despite the presence of uncoupled absorption. The long-time transmission settles down to the value of $T=0.8$ showing the effects of uncoupled absorption as well as effects due to the phenomenological two-photon dephasing rate ($\Gamma_{ba}=0.3\Gamma$). In Figure 5.12(c) the probe detuning is 20 MHz and so the probe transmission is almost unity before turn-on. After turn-on, the transmission falls transiently as the probe begins to resonantly couple the dressed state. The long-time transmission is close to the value 0.5 which is expected from the equal absorption strengths of the two dressed states. We term this phenomenon *dressed-state filling*, because the increase in probe absorption and the associated movement of coherences and populations are accompanying the transient dressing of the $|a\rangle-|c\rangle$ transition. This has previously been called three-level free-induction decay [11]. Figure 5.12(b) shows an intermediate case with probe detuning of $\Delta_p=8$ MHz. No significant differences were found between negative and positive detunings of the probe, as expected from the theory, and so negative detuning traces are not shown.

Note that in Figure 5.12(a) the transmission level appears to be below zero before turn-on. This is due to the intensity drifts of the lasers mention previously in Section 5.3.1, which introduces an error in the determind T. Similarly, Figure 5.12(c) shows a value below 1 instead of total transparency.

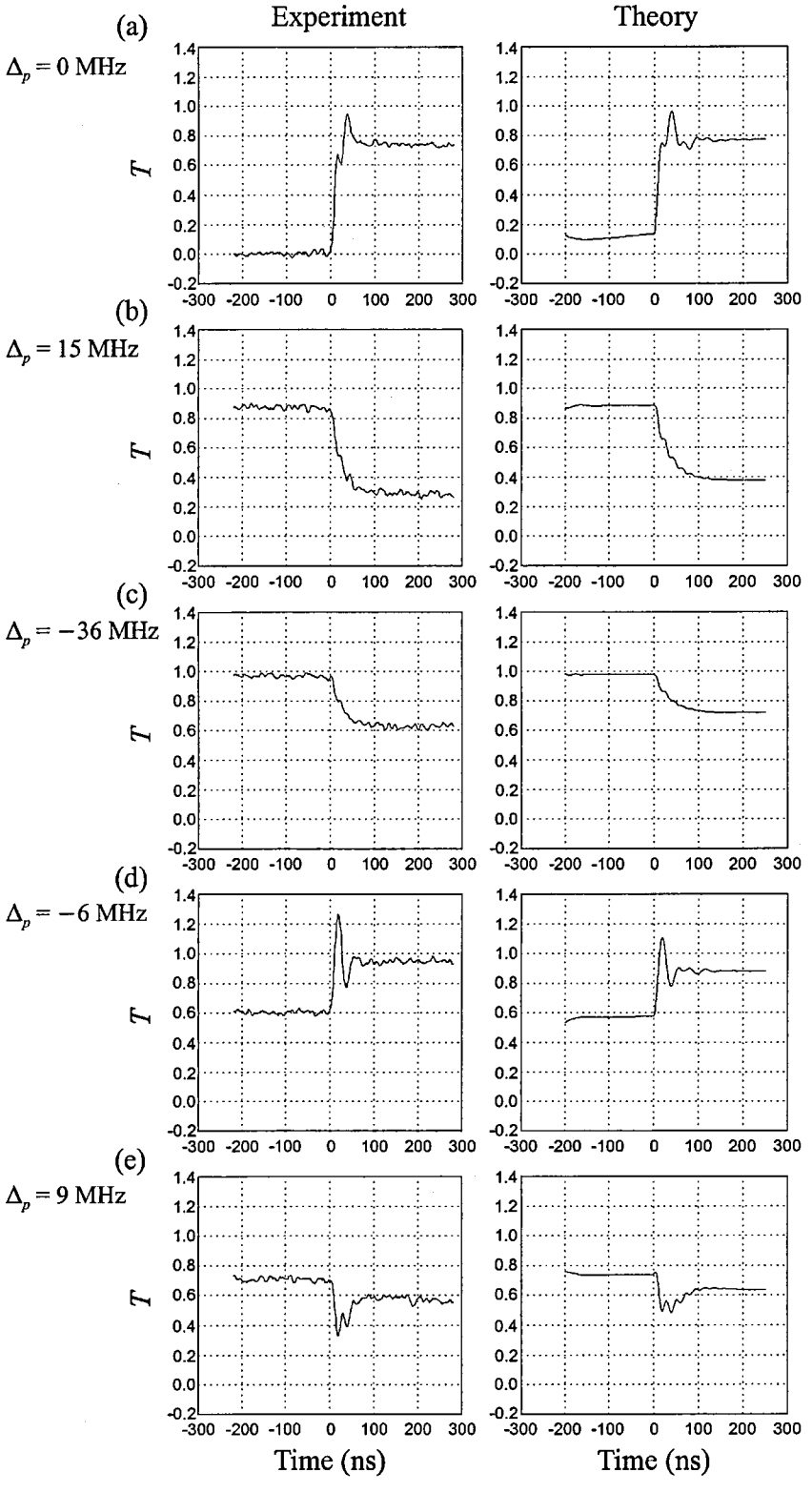

Figure 5.13 - Turn-on transients for varying probe detunings with an off-resonant coupling field: (a) Δ_p=0 MHz (resonant probe), (b) Δ_p=15 MHz (major dressed state filling), (c) Δ_p=−36 MHz (minor dressed state filling), (d) Δ_p=−6 MHz, and (e) Δ_p=9 MHz. In all cases Ω_C=45 MHz, Δ_C=−23 MHz, 50 averages were taken.

Non-resonant coupling field

We now consider the case where the coupling field is detuned from resonance by $\Delta_C = -23$ MHz, representing horizontal lines on Figure 5.2(b). Other parameters and the dynamics before turn-on are the same as before. Experimental and theoretical transient results are presented in Figure 5.13(a)-(e). The first three figures show (a) the case of a resonant probe, (b) the filling of the major dressed state ($\Delta_p = 15$ MHz), and (c) the filling of the minor dressed state ($\Delta_p = -37$ MHz). Trace (d) shows the case where the probe is detuned just to the red of the bare state absorption line ($\Delta_p = -6$ MHz). It is interesting because of the clarity of the signal obtained coupled with the relatively high gain ($T \approx 1.26$) making this a promising region for further transient gain experiments. Finally in Figure 5.13(e) ($\Delta_p = 9$ MHz) the probe is detuned by a similar amount to the blue and shows enhanced absorption dips.

5.5.3 Switching off the coupling field

The experimental conditions for turn-off were different in some respects from those for turn-on. The maximum coupling-field intensity passing the Pockels cell for turn-off was $\Omega_C = 46$ MHz, slightly greater than that for turn-on; also the uncoupled absorption levels are slightly different, probably as a result of optical pumping amongst the Zeeman substates by the coupling field before turn-off. We have found that some of the experimental turn-off transients are remarkable for the high gain and clarity of signal obtained. We attribute the clearer signals to the fact that the system is simpler without the inhomogeneous light shift effects of the coupling field.

Using the analytical result (5.17) with the addition of the effects of uncoupled absorption, we have been able to perform fits to the experimental data using *Origin 6.0284*. The results of these fits are presented as the theoretical traces. The

interdependence of many of the parameters means that some parameters cannot be adequately determined using this method. Fortunately the probe detuning, Δ_p, can be well determined using this method, and the agreement between experiment and theory shows that our system is well described by our three level analysis. Except where mentioned, the values for Δ_p quoted below were determined using the curve fitting. In this Section, $t=0$ defines the turn-off time.

Resonant coupling field

The experimental and corresponding theoretical transients for a resonant coupling field and a range of probe detunings are presented in Figure 5.14. These results correspond to horizontal lines on Figure 5.2(c). Case (a) for a resonant probe shows the transmission dropping from the uncoupled absorption level of $T\approx0.6$ to $T=0$ as the probe fills the bare state transition. Of more interest is case (b) where the probe is detuned to a level corresponding to a pre turn-off dressed state ($\Delta_p=-22$ MHz$\approx-\Omega_C/2$). We term this case *dressed-state emptying* by comparison with the dressed-state filling reported above. The very clear signal features a gain peak rising to $T=1.35$, making this another promising region for further study of transient gain. We note that this is a tunable gain region and is remote from any uncoupled absorptions. The figure also shows two full periods of oscillation. The measured period of oscillation was found to be 46 ns, which is consistent with the probe detuning of -22 MHz determined from the PZT offset voltage. Figure 5.14(c) and (d) were taken for probe detunings of $\Delta_p=17$ MHz and $\Delta_p=-36$ MHz respectively. These results show that cycles of gain and absorption can be present even when there is little or no change in the steady state transmission. We note that the fitted probe detunings of these last two traces are not consistent with those derived from the PZT offset voltages,

namely 7 ± 3 MHz and -12 ± 3 MHz, respectively. As mentioned before, we have attributed this to frequency jumps in the probe laser.

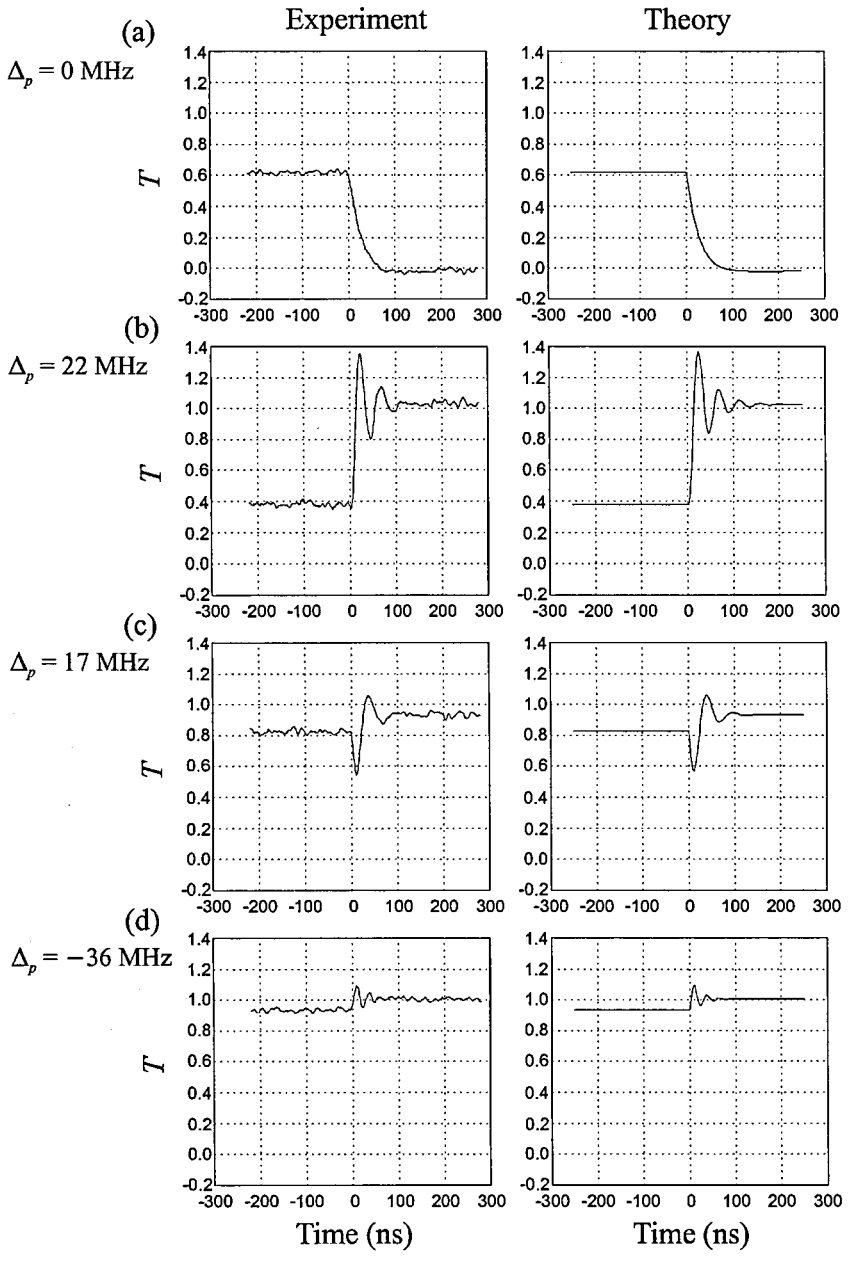

Figure 5.14 - Turn-off transients for a strong, on-resonant coupling field: (a) Δ_p=0 MHz (bare state filling), (b) Δ_p=22 MHz (dressed state emptying), (c) Δ_p=17 MHz, and (d) Δ_p=−36 MHz. In all cases Ω_C=46 MHz before turn-off and 50 averages were taken.

Non-resonant coupling field

The turn-off results for a detuned coupling field (horizontal lines on Figure 5.2(d)) are shown in Figure 5.15. Case (a) shows the transient filling of the bare state and is similar to Figure 5.14(a). Cases (b) and (c) show the major and minor dressed states

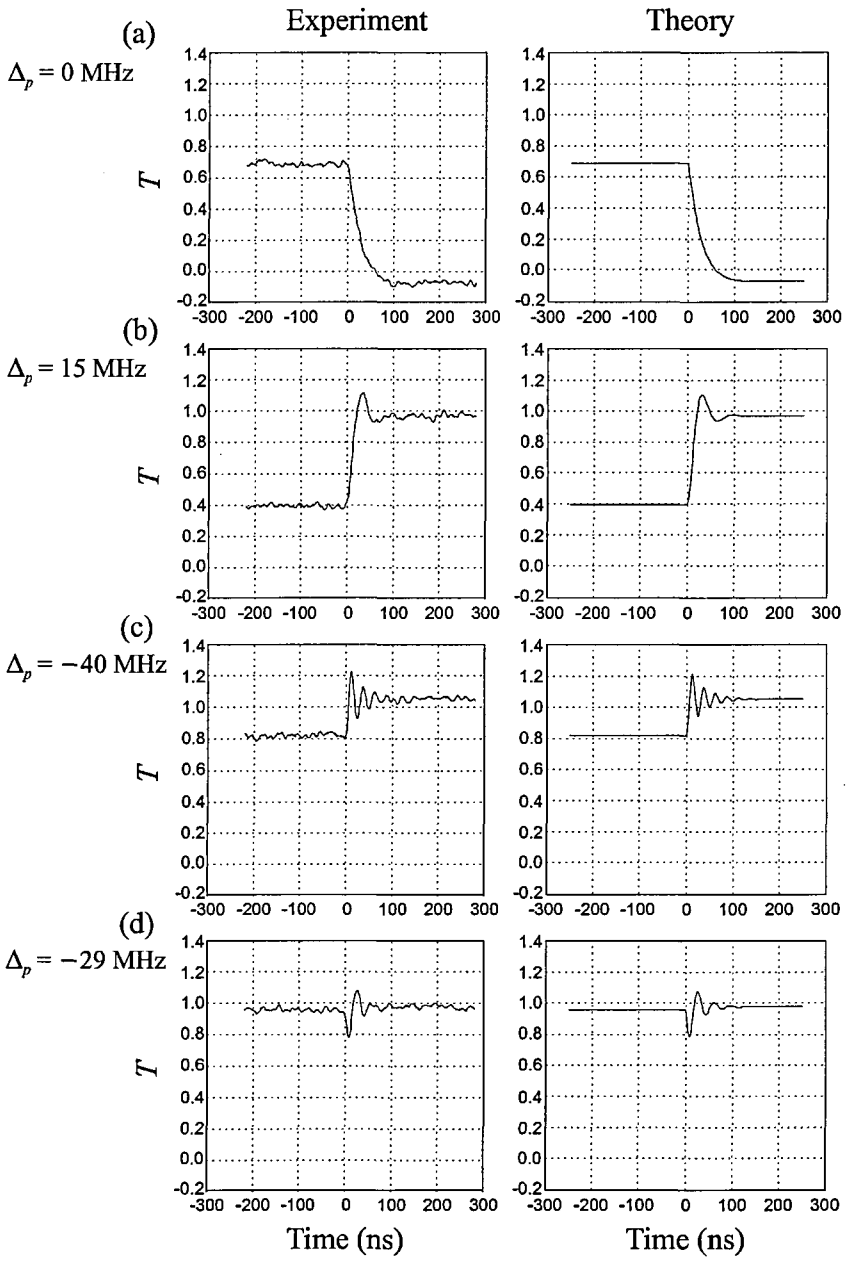

Figure 5.15 - Turn-off transients for a strong, off-resonant coupling field: (a) Δ_p=0 MHz (bare state filling), (b) Δ_p=15 MHz (major dressed state emptying), (c) Δ_p=−40 MHz (minor dressed state emptying), and (d) Δ_p=−29 MHz. In all cases Δ_C=−23 MHz, Ω_C=46 MHz before turn-off and 50 averages were taken.

emptying respectively. As in the case of a resonant coupling field, these transients are characterised by ringing and gain. In case (b) (Δ_p=15MHz, corresponding to the major dressed state) these effects are somewhat obscured by being in the wings of the uncoupled absorption. In contrast, case (c) (Δ_p=−40 MHz, corresponding to the minor dressed state) shows larger gain and exceptionally clear ringing. A fit to the decay of the ringing is shown in Figure 5.16. As expected, this gives a decay rate of 5.5 MHz, which corresponds to half the phenomenological decay rate measured from the probe spectral linewidths. Finally, Figure 5.15(d) is for a probe detuning of Δ_p=−29 MHz, again showing transient features between two regions of steady-state transparency.

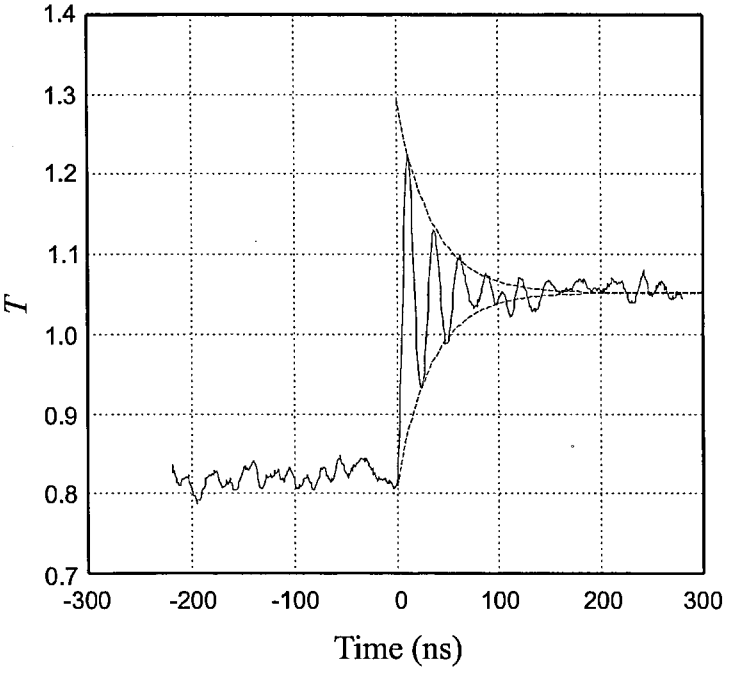

Figure 5.16 - Close-up of experimental Figure 5.15(c) showing the minor dressed state emptying (solid curve) with fitted exponential decays overlaid (dashed curves).

5.6 Summary and conclusions

We have carried out a theoretical and experimental study of resonant and non-resonant transient phenomena associated with the switching of the coupling field on and off in a Λ-type EIT system. These studies have shown novel transient gain features and aid the understanding of transient dressing.

We have experimentally observed interesting transient gain features in both the turn-on and turn-off regimes. We have found it useful to interpret the transient dynamics in terms of the filling and emptying of dressed states. The absolute peak gain values, especially the dressed state emptying, were found to be comparable in strength to the more usual, resonant turn-on case (Section 5.5.2). Non-resonant gain peaks have an important advantage over resonant gain peaks in that they can be tuned by appropriate choice of coupling strengths and detunings. In this way they can, for example, be removed from uncoupled absorptions or perhaps used to match transitions of different frequencies. The turn-off experiments exhibited extremely clear transient signals. We note that by working with other configurations, for example, by reversing the roles of C and P in a dark SPOT trap [106,108], it should be possible to eliminate the broadening effects of the trapping fields and the uncoupled absorptions, and thereby observe larger gain. Another possible way of removing broadening effects of the trapping fields could be by carrying out the experiments in a transient sample immediately after switching off all trapping fields. We have now developed this facility, but we did not have the time to carry out further transient experiments.

On the theory side, we have obtained some new analytical results. In particular we give the weak probe response after turning off the coupling field for arbitrary detunings of both fields. Analysis of the resonant turn-on using the Laplace method enabled us to identify a frequency of oscillation not reported previously. In Appendix C, we analyse

this oscillation in terms of the 3-D Vector Model and outline a parameter regime where we would expect it to be observable.

These transient results are important in the field of gain without inversion because, although transient, they provide tunable gain without population inversion. Especially in the turn-off case, where the clear gain cycles of the dressed-state emptying case (Figure 5.16) could easily be tuned by detuning the coupling field or varying its Rabi frequency. These results also provide some insight on how this system evolves between one described by bare states and one described by dressed states.

Chapter 6

Experiments on the Doubly-Driven V System

In this Chapter we investigate the absorption spectra of a doubly-driven Rb V system probed to a fourth level. The resulting N scheme is shown in Figure 6.1. This system is of interest in the study of photon blockade [1-4], single photon switching [9], cross- and self-phase modulation [123], and other related studies. Most of the work described here has been published [29]. A similar study, also in a Rb MOT but using a different level scheme, was also published [31] at about the same time, indicating the intense interest in this field. Other related theoretical studies are listed in Refs. [24-26].

Section 6.1 presents a dressed-state analysis of the strongly-pumped model V system of Figure 6.1, showing the expected dependence of the probe absorption spectrum on Rabi frequencies and detunings. Section 6.2 describes our experimental realisation of this system in the Rb MOT. The effects of level degeneracies are

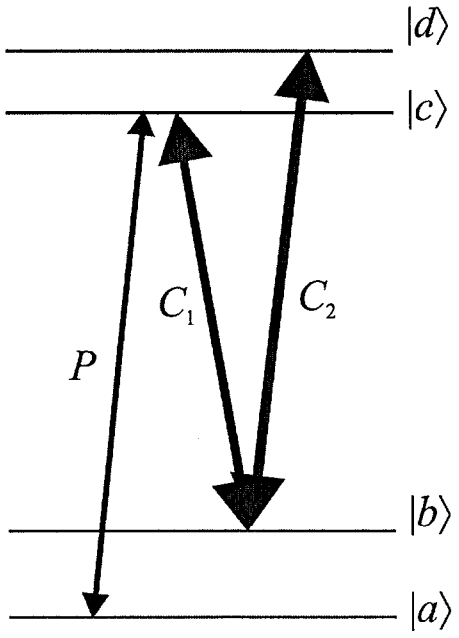

Figure 6.1 - The four-state N configuration. C_1 and C_2 are strong coupling fields driving a V system. P is a weak probe field.

discussed and EIT spectra are shown to illustrate the effects of light shifts and uncoupled absorptions in our experiment. The main results are presented in Section 6.3 where both coupling fields are applied and probe spectra obtained for various coupling field intensities and detunings. Finally, we present the summary and conclusions in Section 6.4.

6.1 Theory of the doubly-driven V system

Figure 6.1 shows a four state N configuration, although for the purposes of this discussion we shall consider it as a three-state V scheme formed by the states $|b\rangle$, $|c\rangle$ and $|d\rangle$ and strong coupling fields C_1 and C_2 of frequencies ω_1 and ω_2, probed weakly on the $|a\rangle - |c\rangle$ transition. The Hamiltonian describing the system consisting of the atom and the two coupling fields can be written down in the semiclassical limit and taking the rotating wave approximation as

$$\hat{H} = \hat{A} + \hat{I}, \tag{6.1}$$

where

$$\begin{aligned} \hat{A} &= \Delta_1 |b\rangle\langle b| + (\Delta_1 - \Delta_2)|d\rangle\langle d|, \\ \hat{I} &= \frac{\Omega_1}{2}(|c\rangle\langle b| + |b\rangle\langle c|) + \frac{\Omega_2}{2}(|d\rangle\langle b| + |b\rangle\langle d|). \end{aligned} \tag{6.2}$$

$\hat{A}$ and $\hat{I}$ represent the atomic and interaction parts of the Hamiltonian $\hat{H}$. $\Delta_1 = \omega_1 - \omega_{cb}$ ($\Delta_2 = \omega_2 - \omega_{db}$) is the detuning of coupling field C_1 (C_2) from the $|b\rangle - |c\rangle$ ($|b\rangle - |d\rangle$) transition and $\omega_{\beta\alpha}$ is the transition frequency of the $|\alpha\rangle - |\beta\rangle$ transition for $\alpha, \beta = a, b, c, d$. $\Omega_j = \mathbf{d}_j \cdot \mathbf{E}_j$ is the Rabi frequency of field $j = 1, 2$ where the electric field $\mathbf{E}_j$ interacts only with its quasi-resonant transition with electric dipole moment $\mathbf{d}_j$. As in Chapter 5, we have chosen units such that $\hbar = 1$ so energies are measured in units of frequency.

Because there are three basis states that describe the system, in the most general case, we expect a characteristic three-line spectrum when performing probe absorption experiments. Writing out the Hamiltonian in matrix form gives

$$\hat{H} = \begin{bmatrix} \Delta_1 & \Omega_1/2 & \Omega_2/2 \\ \Omega_1/2 & 0 & 0 \\ \Omega_2/2 & 0 & \Delta_1 - \Delta_2 \end{bmatrix}. \tag{6.3}$$

Following the method in Shore [124] we diagonalise (6.3) and hence derive the doubly dressed-state energies

$$\begin{aligned} \mathcal{E}_1 &= -\tfrac{1}{3}\alpha + \tfrac{2}{3} p \cos\left(\tfrac{\Theta}{3}\right), \\ \mathcal{E}_2 &= -\tfrac{1}{3}\alpha - \tfrac{2}{3} p \cos\left(\tfrac{\Theta}{3} + \tfrac{\pi}{3}\right), \\ \mathcal{E}_3 &= -\tfrac{1}{3}\alpha - \tfrac{2}{3} p \cos\left(\tfrac{\Theta}{3} - \tfrac{\pi}{3}\right), \end{aligned} \tag{6.4}$$

with

$$\begin{aligned}
\alpha &= -2\Delta_1 + \Delta_2, \\
\beta &= \Delta_1(\Delta_1 - \Delta_2) - \tfrac{1}{4}\left(\Omega_1^2 + \Omega_2^2\right), \\
p &= \sqrt{\alpha^2 - 3\beta}, \\
\cos\Theta &= -\frac{27\gamma + 2\alpha^3 - 9\alpha\beta}{2p^3}, \\
\gamma &= \tfrac{1}{4}\left(\Delta_1\Omega_1^2 - \Delta_2\Omega_1^2\right).
\end{aligned} \tag{6.5}$$

The corresponding dressed-state vector for energy $\mathcal{E}_\nu$ is

$$|D_\nu\rangle = \frac{\mathcal{E}_\nu \dfrac{\Omega_2}{2}|b\rangle + \dfrac{\Omega_1\Omega_2}{4}|c\rangle + \left(\mathcal{E}_\nu(\mathcal{E}_\nu - \Delta_1) - \dfrac{\Omega_1^2}{4}\right)|d\rangle}{N_\nu}, \tag{6.6}$$

with

$$N_\nu = \sqrt{\mathcal{E}_\nu^2 \frac{\Omega_2^2}{4} + \left(\mathcal{E}_\nu(\mathcal{E}_\nu - \Delta_1) - \frac{\Omega_1^2}{4}\right)^2 + \frac{\Omega_1^2\Omega_2^2}{16}} \tag{6.7}$$

being the normalisation constant and $\nu = 1, 2, 3$ indexing the dressed state.

We will now consider in the following Subsections several special cases of theoretical and experimental interest.

6.1.1 Mutual resonance

The first and simplest case to consider is that of mutual resonance of the two coupling fields, i.e. $\Delta_1 = \Delta_2 = 0$. In this case the dressed-state energies and vectors are

$$\begin{aligned}
\mathcal{E}_1 &= \tfrac{1}{2}\sqrt{\Omega_1^2 + \Omega_2^2}, \\
\mathcal{E}_2 &= 0, \\
\mathcal{E}_3 &= -\tfrac{1}{2}\sqrt{\Omega_1^2 + \Omega_2^2},
\end{aligned} \tag{6.8}$$

and

$$|D_1\rangle = \frac{1}{\sqrt{2}}\left(|b\rangle + \frac{\Omega_1}{\sqrt{\Omega_1^2+\Omega_2^2}}|c\rangle + \frac{\Omega_2}{\sqrt{\Omega_1^2+\Omega_2^2}}|d\rangle\right),$$
$$|D_2\rangle = 0|b\rangle - \frac{\Omega_2}{\sqrt{\Omega_1^2+\Omega_2^2}}|c\rangle + \frac{\Omega_1}{\sqrt{\Omega_1^2+\Omega_2^2}}|d\rangle, \qquad (6.9)$$
$$|D_3\rangle = \frac{1}{\sqrt{2}}\left(-|b\rangle + \frac{\Omega_1}{\sqrt{\Omega_1^2+\Omega_2^2}}|c\rangle + \frac{\Omega_2}{\sqrt{\Omega_1^2+\Omega_2^2}}|d\rangle\right).$$

These results can be used to predict the spectrum obtained when probing the doubly driven $|c\rangle - |d\rangle$ transition via the $|a\rangle - |c\rangle$ transition with a weak field of frequency ω_p and detuning $\Delta_p = \omega_p - \omega_{ca}$. The resulting spectrum can be thought of as being made up of a Rabi split doublet, with effective Rabi frequency $\Omega_{\text{eff}}^2 \equiv \Omega_1^2 + \Omega_2^2$, and a three-photon resonance absorption peak at $\Delta_p = 0$. The central peak is strictly only on the three-photon resonance (i.e. satisfies $\Delta_p - \Delta_1 + \Delta_2 = 0$) when $\Delta_1 = \Delta_2$, or in appropriate limits. However, for simplicity we shall refer to the central peak as a three-photon absorption peak when it closely approximates this resonance condition. We note that the probe coupling will be dominated by the $|a\rangle - |c\rangle$ transition as the other transitions are significantly off resonance in the bare atomic basis. Also, in the strong coupling regime (Ω_1, $\Omega_2 \gg \Omega_p$), which applies in our experiments, almost all the population is optically pumped into the state $|a\rangle$ with negligible population in the dressed states. Under these conditions the probe absorption will be proportional to the coefficient $A_v = |\langle c|D_v\rangle|^2$, being

$$A_1 = \frac{1}{2}\frac{\Omega_1^2}{\Omega_{\text{eff}}^2}, \quad A_2 = \frac{\Omega_2^2}{\Omega_{\text{eff}}^2}, \quad A_3 = \frac{1}{2}\frac{\Omega_1^2}{\Omega_{\text{eff}}^2}. \qquad (6.10)$$

This implies that the peaks corresponding to the absorption from state $|a\rangle$ to the outer states $|D_1\rangle$ and $|D_3\rangle$ will have equal heights and dominate the spectrum in the limit $\Omega_1/\Omega_2 \gg 1$, whilst the three-photon absorption peak, corresponding to absorption to $|D_2\rangle$,

will dominate in the limit $\Omega_2/\Omega_1 \gg 1$. Graphs showing the energy levels ε_ν and coefficients A_ν as a function of Ω_2/Ω_1 are presented in Figure 6.2(a) and (b) respectively. These results are similar to those presented for a ladder system by Wei *et al.* [26].

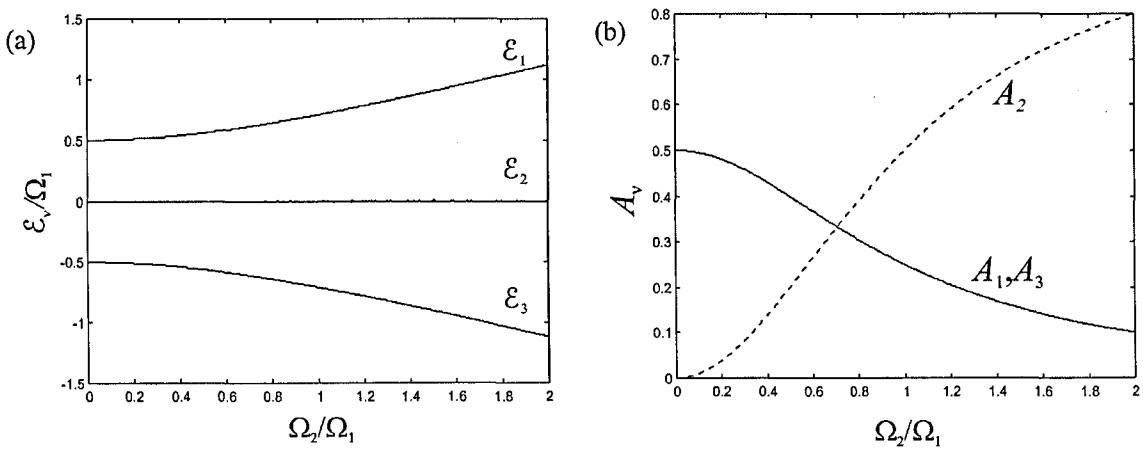

Figure 6.2 - (a) ε_ν/Ω_1 (ν=1, 2, 3), as a function of Ω_2/Ω_1, with $\Delta_1=\Delta_2=0$. (b) The coefficients A_ν as a function of Ω_2/Ω_1.

6.1.2 Effect of detuning C_2

If we now let the detuning Δ_2 of the second coupling field vary, we can numerically solve (6.4) to obtain the dressed-state energies dependency with Δ_2. The results are shown in Figure 6.3. For large $|\Delta_2|$, C_2 has no effect on the system and so it is merely a simple Autler-Townes system. However, as C_2 approaches resonance, the system is transformed into a more complex three-dressed-states one, and back to Autler-Townes when C_2 travels away of resonance. The corresponding three-peak probe absorption spectrum is expected to migrate towards the red as the energies ε_ν fall with increasing detuning Δ_2.

6.1.3 Small equal detunings of C_1 and C_2

In the real system (see Figure 6.4) field C_1 will act non-resonantly with neighbouring transitions, especially the $5S_{1/2}(F=1) \rightarrow 5P_{3/2}(F=1)$ transition, causing

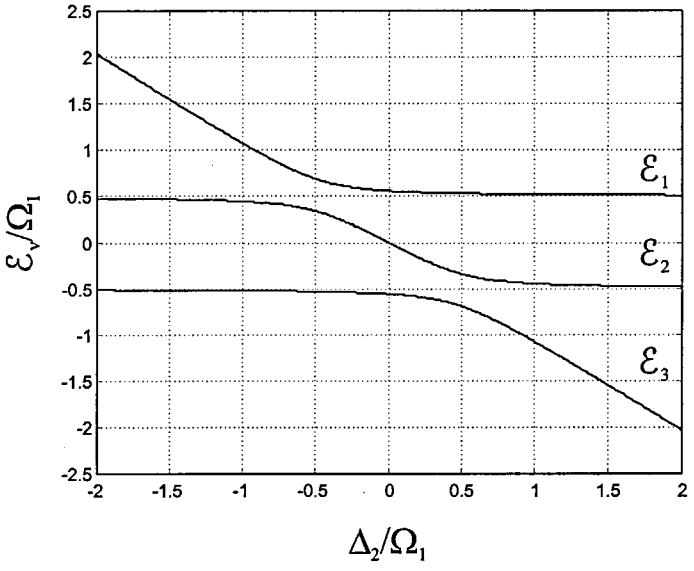

Figure 6.3 - Dressed-state energies as a function of Δ_2.

small light shifts of state $|b\rangle$ (see Section 6.3.1). We can model this effect phenomenologically by introducing a small common detuning of the coupling fields, i.e. we let $\Delta_1=\Delta_2=\Delta$. We present a first order solution for the eigenvalues in the limit $|\Delta| \ll \Omega_{\text{eff}}$. In this case we find that the dressed-state energies are

$$\begin{aligned}
\mathcal{E}_1 &= \frac{\Omega_{\text{eff}}}{2}\left(1+\frac{\Delta}{\Omega_{\text{eff}}}\right)+O\left(\frac{\Delta}{\Omega_{\text{eff}}}\right)^2, \\
\mathcal{E}_2 &= O\left(\frac{\Delta}{\Omega_{\text{eff}}}\right)^2, \\
\mathcal{E}_3 &= -\frac{\Omega_{\text{eff}}}{2}\left(1-\frac{\Delta}{\Omega_{\text{eff}}}\right)+O\left(\frac{\Delta}{\Omega_{\text{eff}}}\right)^2,
\end{aligned} \tag{6.11}$$

and the probe absorptions are

$$\begin{aligned}
A_1 &= \frac{\Omega_1^2}{2\Omega_{\text{eff}}^2}\left(1-\frac{\Delta}{\Omega_{\text{eff}}}\right)+O\left(\frac{\Delta}{\Omega_{\text{eff}}}\right)^2, \\
A_2 &= \frac{\Omega_2^2}{\Omega_{\text{eff}}^2}+O\left(\frac{\Delta}{\Omega_{\text{eff}}}\right)^3, \\
A_3 &= \frac{\Omega_1^2}{2\Omega_{\text{eff}}^2}\left(1+\frac{\Delta}{\Omega_{\text{eff}}}\right)+O\left(\frac{\Delta}{\Omega_{\text{eff}}}\right)^2.
\end{aligned} \tag{6.12}$$

It is interesting to see how, to second order in Δ, only the states $|D_1\rangle$ and $|D_3\rangle$ are affected by the detunings, by an amount proportional to $|\Delta/\Omega_{\text{eff}}| \ll 1$. Therefore, $|D_2\rangle$ remains unshifted and its induced absorption remains the same despite the detuning.

6.1.4 Small different detunings of C_1 and C_2

The case where field C_1 and field C_2 are slightly detuned from resonance by different amounts ($|\Delta_1|$, $|\Delta_2| \ll \Omega_{\text{eff}}$) is an important one to consider in our experiments because it allows the central absorption peak to be resolved from the uncoupled absorption peak (see Section 6.3.2). In this case, we find that the energy eigenstates (to first order) are

$$\begin{aligned}
\varepsilon_1 &= \frac{\Omega_{\text{eff}}}{2} + \frac{\Omega_2^2(\Delta_1 - \Delta_2)}{2\Omega_{\text{eff}}^2} + \frac{\Delta_1}{2} + O(\Delta_1, \Delta_2)^2, \\
\varepsilon_2 &= \frac{\Omega_1^2(\Delta_1 - \Delta_2)}{\Omega_{\text{eff}}^2} + O(\Delta_1, \Delta_2)^2, \\
\varepsilon_3 &= -\frac{\Omega_{\text{eff}}}{2} + \frac{\Omega_2^2(\Delta_1 - \Delta_2)}{2\Omega_{\text{eff}}^2} + \frac{\Delta_1}{2} + O(\Delta_1, \Delta_2)^2,
\end{aligned} \tag{6.13}$$

and the probe absorptions are

$$\begin{aligned}
A_1 &= \frac{\Omega_1^2}{2\Omega_{\text{eff}}^2}\left(1 - \frac{3\Omega_2^2(\Delta_1 - \Delta_2)}{\Omega_{\text{eff}}^3} - \frac{\Delta_1}{\Omega_{\text{eff}}}\right) + O(\Delta_1, \Delta_2)^2, \\
A_2 &= \frac{\Omega_2^2}{\Omega_{\text{eff}}^2} + O(\Delta_1, \Delta_2)^2, \\
A_3 &= \frac{\Omega_1^2}{2\Omega_{\text{eff}}^2}\left(1 + \frac{3\Omega_2^2(\Delta_1 - \Delta_2)}{\Omega_{\text{eff}}^3} + \frac{\Delta_1}{\Omega_{\text{eff}}}\right) + O(\Delta_1, \Delta_2)^2.
\end{aligned} \tag{6.14}$$

In this case, contrary to the previous one, $|D_2\rangle$ is shifted by the detunings Δ_1 and Δ_2, as along as they are different. However, as for equal detunings, its induced absorption remains the same despite the detunings.

6.2 The doubly-driven V system in the Rb MOT

An experimental realisation of the doubly-driven V system in the ^{87}Rb MOT is indicated in Figure 6.4. As in Chapter 5, we have to take into account the light shifts due to off-resonant interactions with other nearby hyperfine levels and the effects of level degeneracies, which lead to uncoupled absorption of the probe. This Section describes the experimental arrangement and discusses the effects of light shifts and uncoupled absorptions.

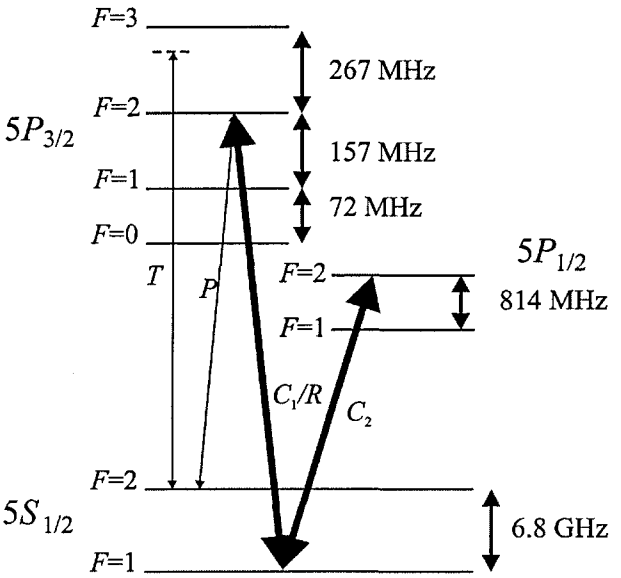

Figure 6.4 - The real ^{87}Rb system in which the experiments are carried out.

6.2.1 Experimental arrangement

All laser fields in Figure 6.4, except for the second coupling field, were derived from the 780-nm laser diodes described in Section 4.2, whilst the second coupling field was derived from the 795-nm laser diode, also described in Section 4.2. The trapping lasers T are locked and detuned by -13 MHz from the $5S_{1/2}(F=2)$ to $5P_{3/2}(F=3)$ transition. The trapping beam diameters are $\approx$1 cm and the total average intensity in the

cold atom sample is ≈60 mW/cm^2. The probe beam P can be scanned across the $5S_{1/2}(F=2)$ to $5P_{3/2}(F=2)$ transition by piezo-control of the external cavity. P has an average intensity ≈2 mW/cm^2 in a diameter ≈1 mm. The coupling beam C_1 and the trap's repumping field R are derived from the same laser, which is the slave of a locked ECDL. They are resonant with the $5S_{1/2}(F=1)$ to $5P_{3/2}(F=2)$ transition. The average intensity of C_1 is ≈400 mW/cm^2 in a roughly elliptical profile 2 mm×4 mm. A second coupling beam C_2 is quasi-resonant with the $5S_{1/2}(F=1)$ to $5P_{1/2}(F=2)$ transition at 795 nm (the D_1 line). For resonant experiments, C_2 was locked, but for detuned experiments it was stepped using the external cavity piezo with the frequency determined by a calibrated optical spectrum analyser. The average intensity of C_2 could be varied up to a maximum of ≈300 mW/cm^2, in a beam diameter ≈1.3 mm.

The experimental set-up is shown schematically in Figure 6.5. The probe P and the second coupling field C_2 are linearly polarised in the horizontal plane whilst the coupling field C_1 is linearly polarised in the vertical direction. This particular choice of orthogonal linear polarisations was chosen because it was found to reduce the uncoupled absorption of the probe field at the frequency of the $5S_{1/2}(F=2)$ to $5P_{3/2}(F=2)$ transition (see Section 5.3.2). The angle between the coupling fields C_1 and

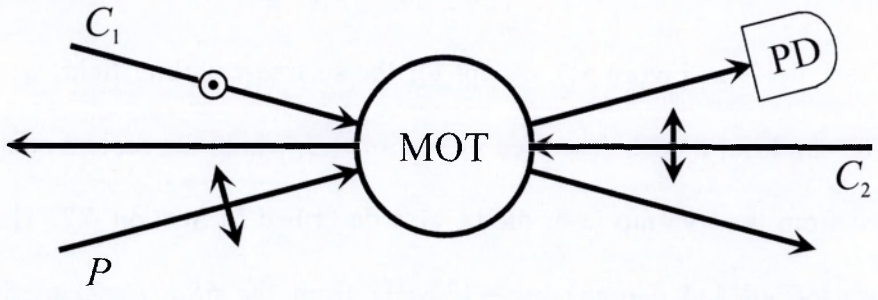

Figure 6.5 - Schematic of the experimental arrangement showing beam polarisations. *PD* is an avalanche photodiode. The trapping fields are not shown for clarity.

C_2 is about 175° while the probe propagates at an angle of about 20° with respect to C_1. These angles were found to give a good overlap of the probe with the coupling fields in the MOT. The paths of all three beams are coplanar.

6.2.2 Zeeman degeneracies and uncoupled absorptions

The origin of uncoupled absorptions in the probe spectra of the doubly-driven Rb V system is similar to that described in the Λ system of Section 5.3, but here we have to consider the effects of the additional coupling field C_2 and the additional level $5P_{1/2}(F=2)$.

Figure 6.6(a) illustrates the individual Zeeman states of the hyperfine levels coupled by the probe P (fine lines) and two driving fields C_1 (thick lines) and C_2 (double lines). The quantisation axis in Figure 6.6 has been taken to be along the polarisation of C_2. A small (≈7% of the intensity) contribution of sigma polarisation from the probe field due to the small (≈15°) angle between the polarisation of P and C_2 has been ignored. Also shown in Figure 6.6 are the corresponding Clebsch-Gordan coefficients. The states $|m\rangle_X$ are labelled in terms of the magnetic quantum number m and X, where X is one of a, b, c or d which correspond to the levels in Figure 6.1 and also to the $5S_{1/2}(F=2)$, $5S_{1/2}(F=1)$, $5P_{3/2}(F=2)$ and $5P_{1/2}(F=2)$ levels respectively in Figure 6.4.

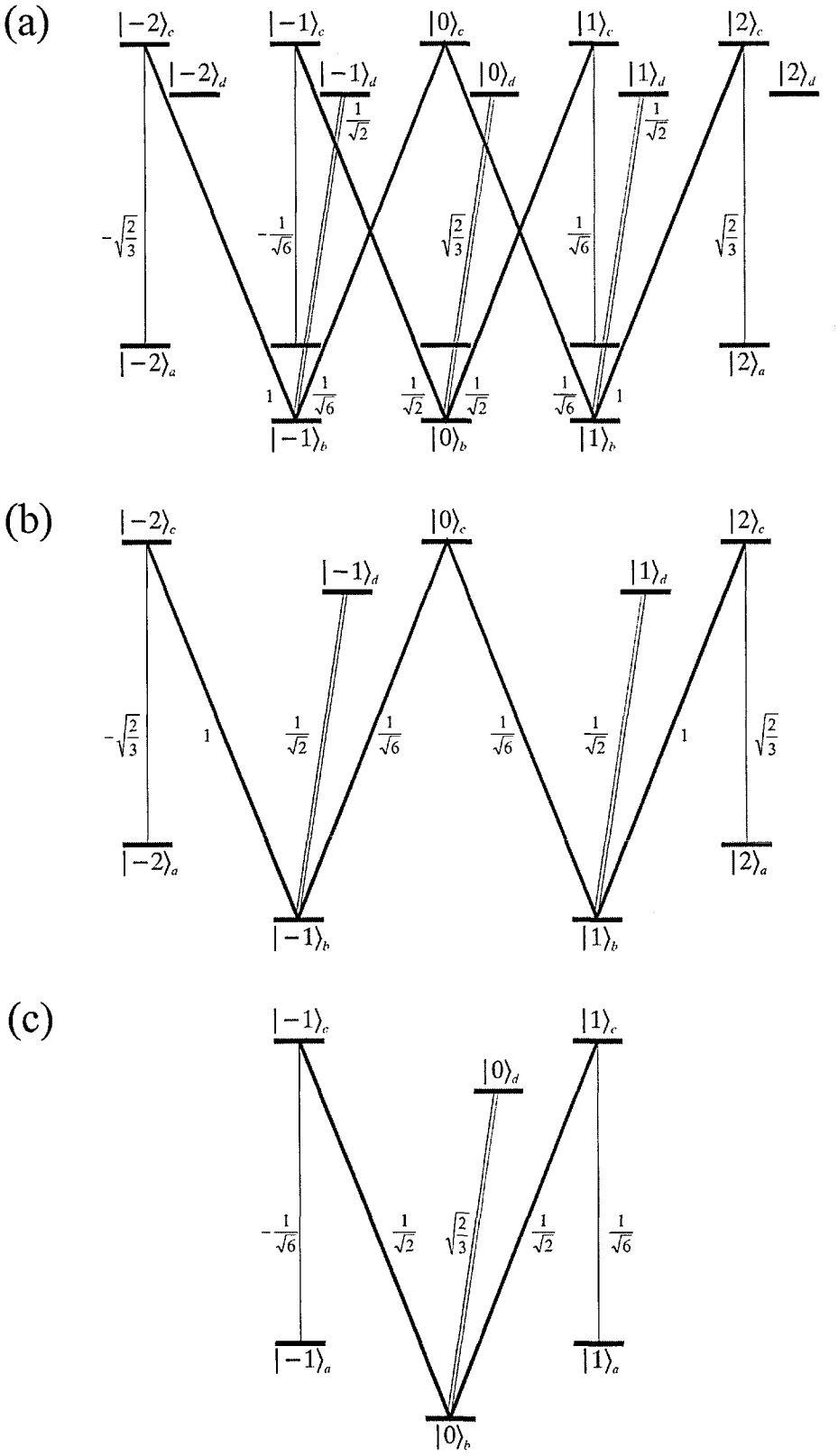

Figure 6.6 - Zeeman states, coupled transitions and Clebsch-Gordan coefficients in the (a) whole system (b) the nine-state system and (c) the six-state system. The fields P, C_1 and C_2 are represented respectively by thin lines, thick lines and double lines.

As in Figure 5.7(b) and (c), Figure 6.6(b) and (c) show the quadruply-driven 'W' configuration and the doubly-driven V configuration provided by the coupling field C_1 (thick lines) alone. Taking account of the additional states coupled by the fields C_2 and P it appears that a nine-state (Figure 6.6(b)) and, separately, a six-state (Figure 6.6(c)) model are necessary to describe the dynamics of the experiment. In this case, three states ($|0\rangle_a$, $|-2\rangle_d$ and $|2\rangle_d$) do not interact with any fields. By making the same change of basis as used in (5.20) in Section 5.3.2, this complex structure reduces to the sets of simple coupled systems shown in Figure 6.7. Three doubly driven V configurations, of the type shown in Figure 6.1, are clearly evident in the new basis. Also shown are the effective Clebsch-Gordan coefficients for the new transformed transitions.

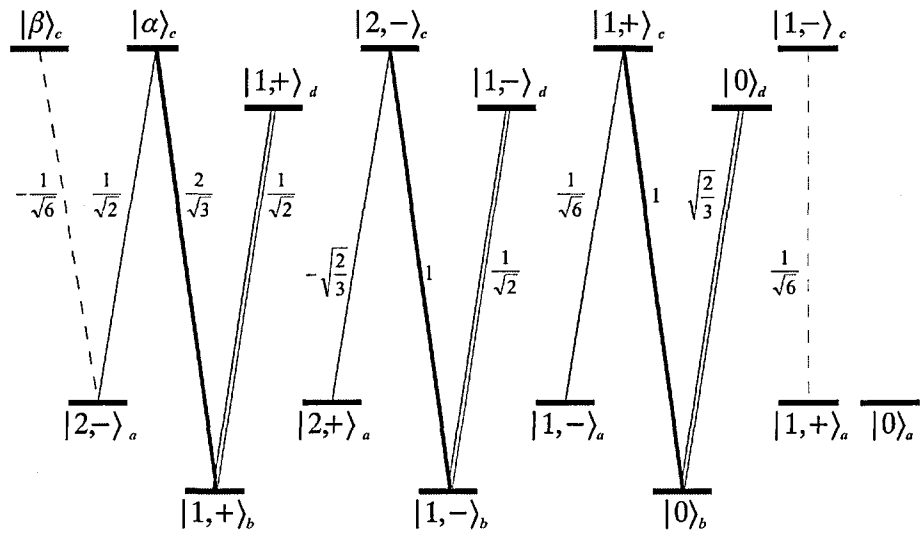

Figure 6.7 - Zeeman states, coupled transitions and Clebsch-Gordan coefficients in the new basis, showing the uncoupled absorptions (dashed transitions). Three separate N configurations are clearly visible in the new basis. The fields *P*, C_1 and C_2 are represented respectively by thin lines, thick lines and double lines.

Again, the five coupled states on the left of Figure 6.7 show that the (relatively weak) field P simultaneously probes a doubly-driven V configuration as well as the uncoupled $|2,-\rangle_a - |\beta\rangle_c$ transition. This uncoupled transition simply causes additional absorption and scattering of field P and so, essentially, this five-state system can be

treated as an ideal four-state N configuration (as shown in Figure 6.1) with an additional uncoupled absorption. Thus, the underlying probe absorption profile is due essentially to three separate N configurations (solid lines) with two uncoupled absorptions (dashed lines).

As in Section 5.3.2, each N configuration has a different set of (effective) Clebsch-Gordan coefficients, and so the Rabi frequencies for the fields P, C_1 and C_2 differ from one N configuration to the next. However, a single four-state model, as given in Section 6.1, is sufficient to model our experiment, provided we allow for broadened absorption peaks and uncoupled absorptions.

Finally we note that state $|0\rangle_a$ is again a dark state, i.e. uncoupled by any field. However, as mentioned previously, the population tends to redistribute among the $5S_{1/2}(F=2)$ Zeeman sublevels.

6.2.3 Light shifts and broadening effects

The coupling beams C_1 and C_2 are tuned to different optical transitions that are well-separated in frequency. This way, we avoid potentially complex mutual light shifts induced by the two beams. However, some other simple light shifts due to C_1 and the effects of the trapping beams do have to be taken into account.

While C_2 is turned off, C_1 and P form a Λ-type EIT system, as mentioned in Section 5.4.1 previously. Figure 6.8 shows the probe absorption spectrum with C_1 locked to the $5S_{1/2}(F=1)$ to $5P_{1/2}(F=2)$ transition in the saturated absorption cell, and with C_2 turned off. The probe detuning is taken to be zero when the probe frequency is equal to the $5S_{1/2}(F=2)$ to $5P_{3/2}(F=2)$ transition frequency in the saturated absorption cell. As before, the spectrum consists of a central peak situated between the two Autler-Townes peaks of a standard asymmetric EIT profile expected with detuned coupling

field. The central peak in the spectrum is caused by the previously mentioned uncoupled absorptions. The detuning of C_1 is due to the fact that the $5S_{1/2}(F=1)$ level of the sample is light-shifted with respect to the same level in the saturated absorption cell because of the interaction of C_1 with neighbouring transitions (mainly the $5S_{1/2}(F=1)$ to $5P_{3/2}(F=1)$). From the asymmetry of the spectrum, we have estimated this light shift to be $\approx$7 MHz.

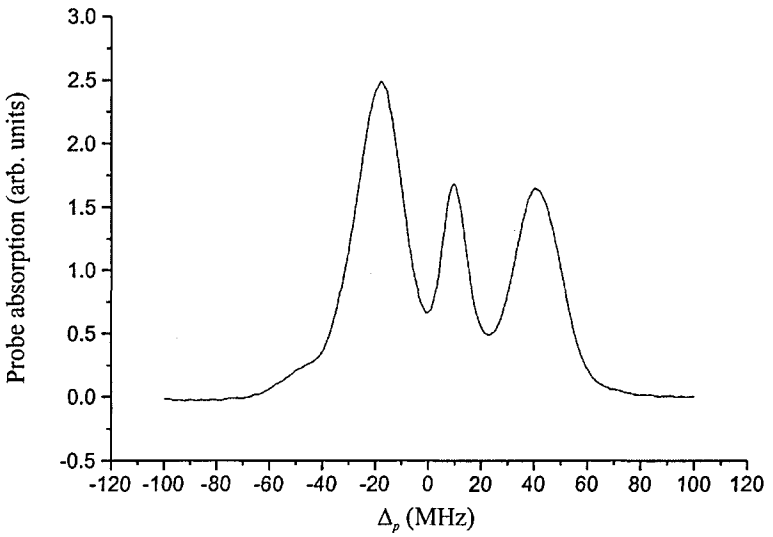

Figure 6.8 - Probe absorption spectrum with C_1 on and C_2 off. The spectrum is an average over 200 scans. Ω_1=62 MHz.

It is to be noted that all three peaks in Figure 6.8 are displaced by approximately 9 MHz with respect to the saturated absorption transition. Once more, this is because the trapping beams T act as a detuned coupling field with P in a V-type EIT configuration, as can be seen from Figure 6.4. The small red-detuned peak is just visible at $\Delta_p \approx -50$ MHz in Figure 6.8.

As mentioned in Section 5.4.1, the linewidths of our spectra are broadened by beam profile inhomogeneities, variations of Clebsch-Gordan coefficients between different Zeeman transitions, the spread in the intensities of the six interfering trapping beams in the MOT, and finally Zeeman splitting due to the MOT's magnetic field.

6.3 Three-peak spectra of the V system

Our experiments in the Rb N configuration of Figure 6.4 explore two aspects of the three-peak spectra predicted by our theory of Section 6.1. We first investigate the effects of increasing the power P_2 of the second coupling field C_2. The predicted behaviour, illustrated in Figure 6.2, shows an increasing separation of the two outer peaks and a growth of the three-photon absorption peak. We then turn our attention to the predicted migration of the three-peak spectra with the detuning of C_2, as illustrated by the dressed-state energies shown in Figure 6.3.

To this end we consider three different cases:

I. We study the effects of P_2 on the probe spectrum when C_1 and C_2 are tuned to their transitions in the saturated absorption cells and are therefore detuned by equal amounts ($\Delta \approx 7$ MHz) from the sample transitions, due to the C_1-induced light shifts described in Section 6.2.3. This is the case described in Section 6.1.3. The three-photon peak is expected to coincide with the saturated absorption peak in this case.

II. We study the effects of P_2 on the probe spectrum when C_1 is detuned by -19 MHz from the saturated absorption transition in order to resolve the three-peak spectra from the uncoupled absorptions. This is the case discussed in Section 6.1.4.

III. We study the effects of the detuning Δ_2 as C_1 remains resonant with the saturated absorption transition, the case discussed in Section 6.1.2.

6.3.1 Case I

The probe absorption spectra shown in Figure 6.9 were obtained with C_1 and C_2 tuned to their respective transitions in saturated absorption cells; these are the same conditions that applied in Figure 6.8 except that now C_2 is switched on and its power P_2 varied. A comparison of the spectra in Figure 6.9 shows that the height h_c of the central peak grows with P_2 due to the appearance of the three-photon absorption peak, as predicted in Section 6.1, on top of the uncoupled absorption peak. There is also an increase in the splitting, $\delta_{13}=\varepsilon_1-\varepsilon_3$, of the two Autler-Townes peaks.

These two effects are illustrated in Figure 6.10(a)&(b), where the height h_c and the splitting δ_{13} are plotted against the power P_2. The theoretical fits in these figures were obtained from the theory in Section 6.1.3, as follows. We assume that the contribution of the three-photon absorption peak is proportional to $A_2=|\langle c|D_2\rangle|^2$, and that both coupling fields have a common detuning of $\Delta\approx 7$ MHz from their respective transitions in the sample due to the C_1-induced light shift of the $5S_{1/2}(F=1)$ level[2]. We find from (6.11) and (6.12), to first order in Δ,

$$\begin{aligned} \delta_{13} &= \sqrt{\Omega_1^2+\Omega_2^2}+O(\Delta)^2, \\ h_c &= h_{uc}+B\frac{\Omega_2^2}{\Omega_1^2+\Omega_2^2}+O(\Delta)^3, \end{aligned} \tag{6.15}$$

where h_{uc} is the height of the uncoupled absorption peak, i.e. the height of the central peak when C_2 is turned off, and B is a constant. These equations have been fitted to the data points in Figure 6.10(a)&(b) using the following functional forms

[2] There are no significant light shifts due to C_2 because of the large splitting (814 MHz) between the excited states of the D_1 line.

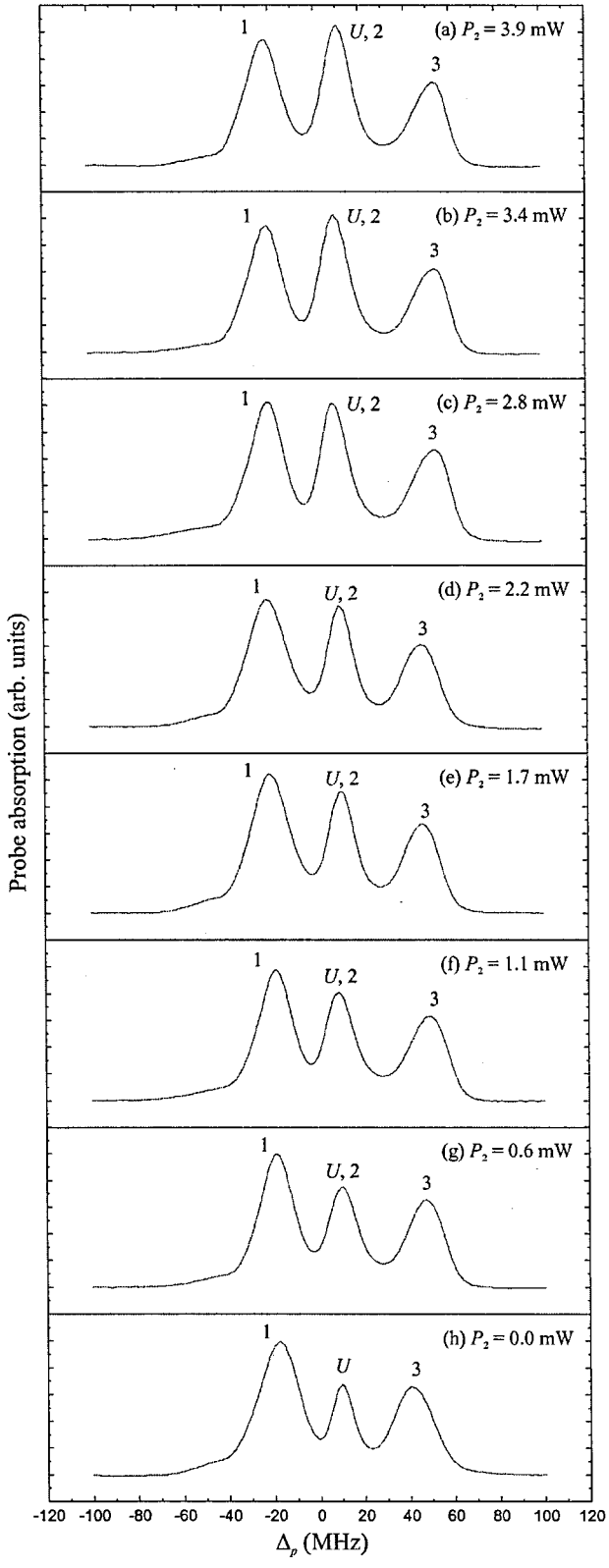

Figure 6.9 - Probe absorption spectra with both C_1 and C_2 on for various powers of C_2 and $\Delta \approx 7$ MHz. Each spectrum is an average over 200 scans.

$$\delta_{13} = \sqrt{a + bP_2},$$
$$h_c = d\frac{cP_2}{1+cP_2} + e. \tag{6.16}$$

The fit in Figure 6.10(a) gives a=3800±200 MHz^2, b=500±90 MHz^{2}mW^{-1}. From the value of a, it is easy to extract that Ω_1=62±2 MHz, and from $\sqrt{bP_2}$, we have Ω_2=(22±2 MHz/mW$^{1/2}$)$P_2^{1/2}$ with a maximum of Ω_2=44±5 MHz. These Rabi frequencies are consistent with the values estimated from the parameters of beams C_1 and C_2 and the Clebsch-Gordan coefficients of the transitions. The fit in Figure 6.10(b) gives c=0.15±0.1 mW^{-1}, d=3±1 and e=1.67±0.06. From $\sqrt{cP_2}$, we get Ω_2/Ω_1=0.8±0.3 for maximum Ω_2, which is consistent with the previous fit; the constant d determines the relative heights of the uncoupled absorption peak and the three-photon absorption peak. We note that for maximum power of C_2 the three-photon absorption peak accounts for approximately 0.4 of the total central peak height.

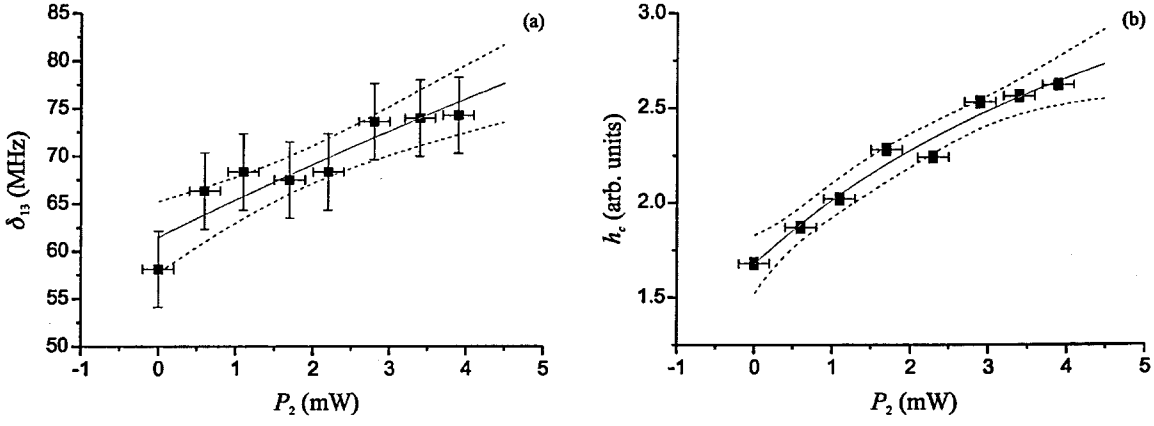

Figure 6.10 - (a) Separation of the Autler-Townes peaks δ_{13} and (b) the height h_c of the central absorption peak, plotted against the power P_2. The solid lines are the theoretical fits and the dashed lines are the 95% confidence bands.

6.3.2 Case II

In this case C_1 is detuned by −19 MHz from the saturated absorption transition, while maintaining C_2 tuned to the saturated absorption transition. This case has been

chosen because it is possible to resolve the C_2-induced peak from the uncoupled absorptions.

Figure 6.11 shows the probe absorption spectra for various values of P_2 when both coupling beams are on. By noting the asymmetry in Figure 6.11(f), it is clear that this corresponds to a case where C_1 is detuned. This detuning of the atoms in the cloud, can easily be determined by the asymmetry of the profile, and it was found to be $\Delta_1 \approx -10$ MHz.

Once again, as in Figure 6.9, we can see how the thee-photon peak, labelled 2, corresponding to $\mathcal{E}_2$, grows with P_2 as expected from the theory, but in this case it is resolved from the uncoupled absorptions. Again the splitting δ_{13} of the Autler-Townes and the height h_2 of the peak corresponding to $\mathcal{E}_2$ are plotted in Figure 6.12. From (6.13) and (6.14) we find

$$\begin{aligned} \delta_{13} &= \sqrt{\Omega_1^2 + \Omega_2^2} + O(\Delta_1, \Delta_2)^2, \\ h_2 &= B\frac{\Omega_2^2}{\Omega_1^2 + \Omega_2^2} + O(\Delta_1, \Delta_2)^2, \end{aligned} \tag{6.17}$$

where B is a constant. Their corresponding theoretical fits have been done in a similar way to those of Case I. The fit in Figure 6.12(a) gives $\Omega_1 = 65 \pm 2$ MHz and $\Omega_2 = (16 \pm 2\ \text{MHz/mW}^{1/2}) P_2^{1/2}$ with a maximum of $\Omega_2 = 31 \pm 4$ MHz. These Rabi frequencies are again consistent with the values estimated from the parameters of beams C_1 and C_2 and the Clebsch-Gordan coefficients of the transitions. The fit in Figure 6.12(b) gives $\Omega_2/\Omega_1 = 0.2 \pm 0.3$ for maximum Ω_2, which is consistent with the previous fit. The big error in this value, and the fact that it is only just consistent with that obtained in Case I, is due to the lack of sensitivity of the fitting curve to this parameter.

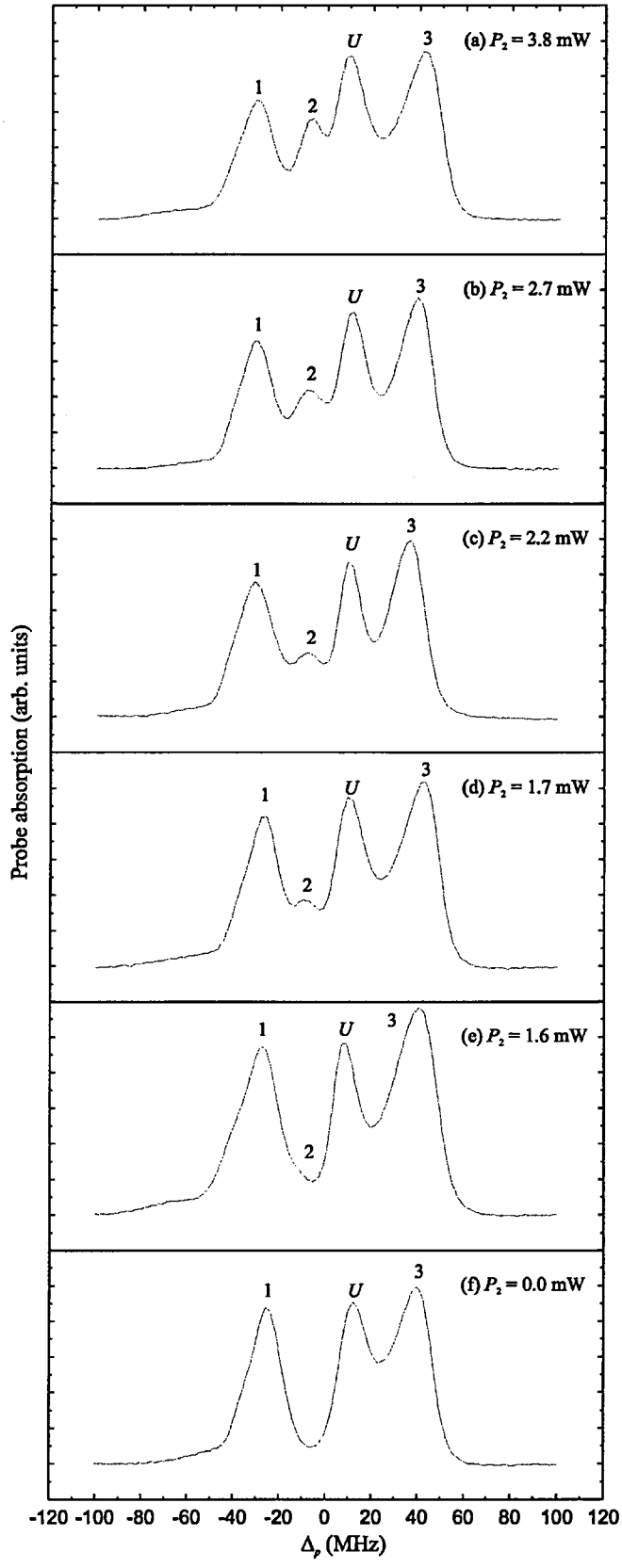

Figure 6.11 - Probe absorption spectra with both C_1 and C_2 on for various powers of C_2 and $\Delta_1 \approx -10$ MHz. Each spectrum is an average over 200 scans.

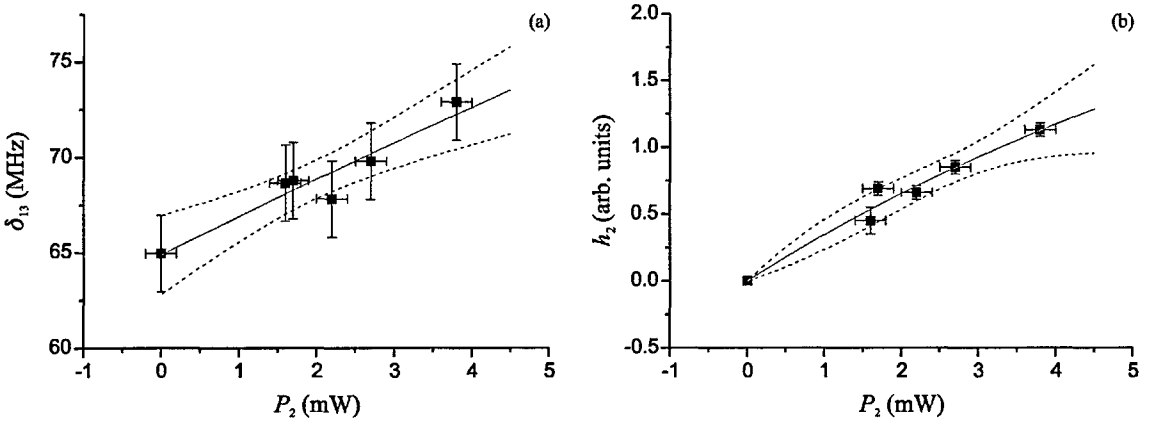

Figure 6.12 - (a) Separation of the Autler-Townes peaks δ_{13} and (b) the height h_2 of peak 2, plotted against the power P_2. The solid lines are the theoretical fits and the dashed lines are the 95% confidence bands.

6.3.3 Case III

We now consider the case where C_2 has its maximum intensity and its detuning Δ_2 is stepped across the $5S_{1/2}(F=1)$ to $5P_{1/2}(F=2)$ transition, with C_1 tuned to the saturated absorption line as before. The detuning of C_2 is measured by a calibrated spectrum analyser with respect to the saturated absorption line. The traces obtained are plotted in Figure 6.13. It is seen that as Δ_2 is stepped from the red towards the blue, the uncoupled absorption peak, labelled *U*, remains fixed in position as expected, but the peaks labelled 1, 2 an 3 migrate towards the red, with the central peak 2 moving across the uncoupled absorption. The positions of peaks 1, 2 and 3 are shown as points in Figure 6.14 with the curves showing the corresponding theoretical expectations (6.4) based on a detuning $\Delta_1 \approx 7$ MHz of C_1. This trace shows very good agreement between theory and experiments, although there is one point which does not match the theoretical expectation, probably due to a bad measurement. Note that the spectrum is a simple Autler-Townes doublet for $|\Delta_2| \gg \Omega_1$. We note that this behaviour is qualitatively similar to that predicted for a ladder system in [26].

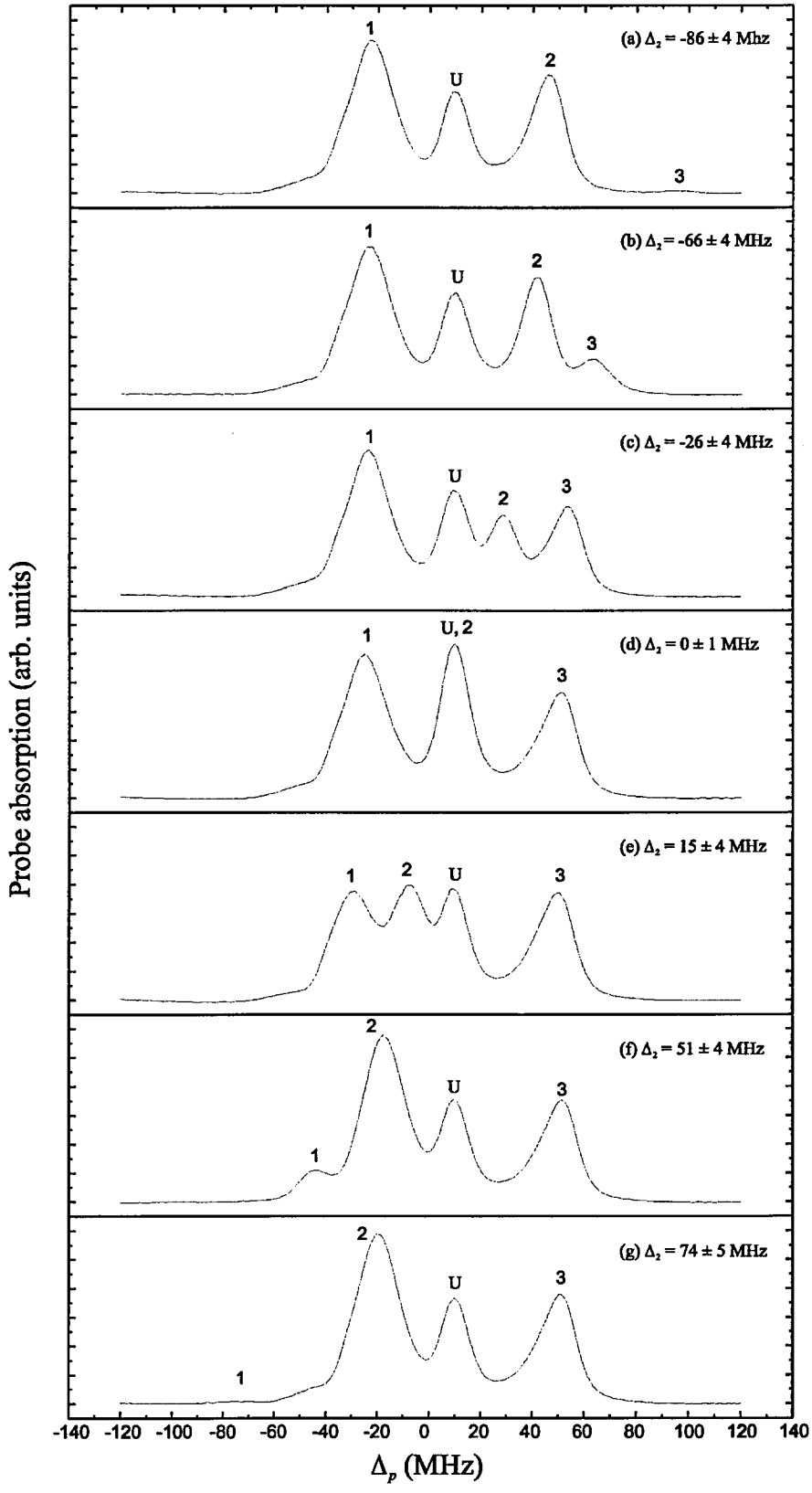

Figure 6.13 - Probe spectra showing the migration of the three-peak structure as the detuning Δ_2 of the coupling field C_2 is stepped from the red to the blue side of the resonance. The peaks are labelled 1, 2 and 3 corresponding to absorption to levels $\mathcal{E}_1$, $\mathcal{E}_2$ and $\mathcal{E}_3$. The uncoupled absorption peak is labelled *U*. Each spectrum is an average over 200 scans.

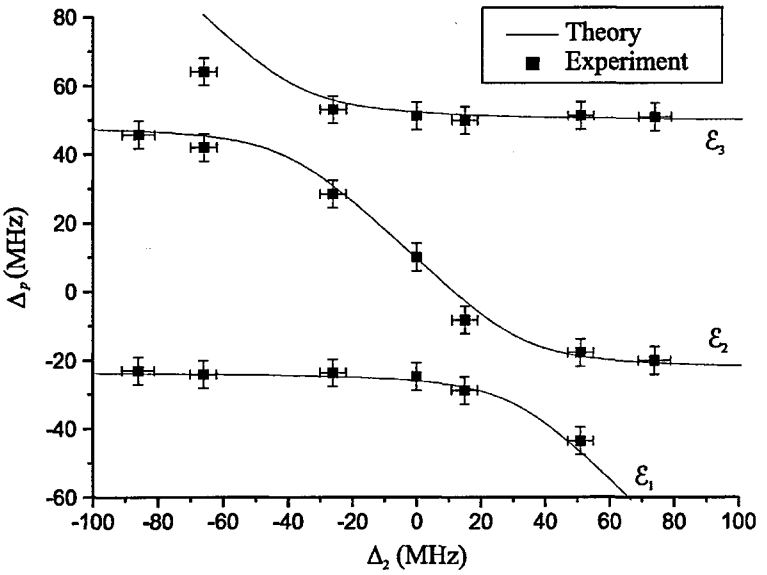

Figure 6.14 - The positions of the absorption peaks as a function of detuning Δ_2. The points are taken from the measured spectra and the red curves are the theoretical expectations based on a detuning Δ_1=7 MHz of C_1.

6.4 Summary and conclusions

We have studied a doubly driven V-system probed from a fourth level in an N configuration. The experiments show the expected three-peak spectrum with the growth of the three-photon absorption peak and the increasing separation of the Autler-Townes peaks as the second coupling field intensity is increased. We have also observed the evolution of the three-peak probe absorption spectrum as the detuning of one of the coupling fields is changed. After taking account of light shifts, the effects of the trapping beams and the uncoupled absorptions in this real system, the measured spectra are in good agreement with the analytical predictions. This investigation is important for the understanding of a physically realisable N system that might be used in cross-phase modulation, photon blockade [1-4] and other related studies. In particular for the single-photon switch proposed by Harris and Yamamoto [9], which is the quantum analogue to

our experiment. If our doubly-driven V system could be realised at the single-photon level and operate as a single-photon switch, it could become of great importance for quantum information processing applications.

Chapter 7

Summary, Conclusions and Look Ahead

We finish this thesis by presenting the summary and conclusions in Section 7.1, drawn from the work and experiments previously described. Finally, we outline in Section 7.2 the work currently being done in this laboratory and the possible extensions of this work.

7.1 Summary and conclusions

During the course of this thesis we have seen the development and upgrade of the experimental apparatus in Chapter 4, demonstrated Rabi ringing and gain features in transient EIT in Chapter 5, and also observed for the first time probe absorption spectra of a doubly-driven V system in Chapter 6. The summary and conclusions drawn from these three Chapters are brought together in the following Sections.

7.1.1 Development of experimental apparatus

In Chapter 4, we have described the development of the experimental apparatus previously used in this laboratory. We have increased the power of the lasers and changed their design to a more reliable one. We also built a new master-slave laser system at 780 nm and an ECDL at 795 nm. New saturated absorption set-ups and locking electronics accompanied this development to make the locking of these lasers more reliable. This work permitted the expansion of the trapping beams in order to trap a higher number of atoms. We can now trap of order 10^8 atoms compared to 10^7 before, and the trap is much more stable.

We also developed the ability to computer control the experiment by the installation of data acquisition cards and the writing of control software.

We did as well some preliminary experiments on implementing a dark SPOT. Although these experiments were in some ways incomplete, they showed a substantial increase in the lower ground state ($F=1$) population of Rb in the dark SPOT configuration. This preliminary work alerted us to some of the problems we would face when developing this technique for the second-generation MOT.

We ended Chapter 4 describing the building of a new second-generation MOT. This MOT has an increased trapping beam diameter, better quality optical windows, and an improved magnetic field gradient, allowing us to trap a still larger number of atoms, hopefully up to 10^9. Larger atomic densities could also be obtained with the help of an improved dark SPOT configuration.

7.1.2 Transient EIT

In Chapter 5, we carried out a theoretical and experimental study of resonant and non-resonant transient phenomena in a Λ-type EIT system when the coupling field is

non-adiabatically switched on and off. These studies have shown novel transient gain features and aid the understanding of how such a system evolves from one described by bare states to one described by dressed states.

We have obtained some new analytical transient results using the Laplace transform method. In particular we give the weak probe response in the turn-off regime for arbitrary detunings of the coupling and probe fields. We have identified a new frequency of oscillation in the turn-on case. We analysed this oscillation in terms of the 3-D Vector Model in Appendix C and suggested a parameter regime where we would expect it to be observable.

We have also experimentally observed interesting transient gain features in both the turn-on and turn-off regimes. The non-resonant gain peaks can be tuned by changing the coupling field Rabi frequency and detuning. In this way they can, for example, be removed from uncoupled absorptions or perhaps used to match transitions of different frequencies. The turn-off experiments exhibited extremely clear transient ringing. These results may be important in the field of gain without inversion because they provide tunable gain without population inversion. This is especially so in the turn-off case, where the clear gain cycles for dressed-state emptying (Figure 5.16) could easily be tuned by varying the intensity or detuning of the coupling field.

7.1.3 Doubly-driven V system

In Chapter 6, we have studied a doubly-driven V system probed from a fourth level in an N configuration. The experiments show the growth of the three-photon absorption peak and the increasing separation of the Autler-Townes peaks in the expected three-peak spectrum, as the second coupling field intensity is increased. We have also observed the evolution of the three-peak probe absorption spectrum as the detuning of one of the coupling fields is changed. The measured spectra are in good

agreement with the analytical predictions after taking account of light shifts, the effects of the trapping beams and the uncoupled absorptions in the real system.

This investigation is important for the understanding of a physically realisable N system that might be used in cross-phase modulation, photon blockade [1-4] and other related studies. The single-photon switch proposed by Harris and Yamamoto [9] (outlined in Section 2.2.2) is of particular interest because it is the quantum analogue to our experiment. If our doubly-driven V system could be realised at the single-photon level and operate as a single-photon switch, it could become of great importance for quantum information processing applications.

7.2 Look ahead

The experiments presented in this thesis have produced good original results which are well modelled by the theory presented when taking into account the particular experimental parameters. However, there is still room for improvement and further results could be obtained, especially after the commissioning of the second-generation MOT.

7.2.1 Improving the transient EIT experiments

Transient EIT could be improved by working with other configurations, for example, by reversing the roles of C and P in a dark SPOT trap [106,108]. In this configuration, the probe field would not be affected by the trapping fields because they would not share any levels. Therefore, it should be possible to eliminate the broadening effects of the trapping fields and the uncoupled absorptions, and thereby observe larger gain. With the building of the second-generation MOT, we have set-up a new improved dark SPOT configuration.

Another possible way of removing broadening effects of the trapping fields and the magnetic field gradient, could be by carrying out the experiments in a transient sample immediately after switching off all trapping and magnetic fields. We have now developed this facility in the second-generation MOT, and the current experiments being done in this laboratory have shown that there is an improvement in the $5S_{1/2}(F=1)$ population and the linewidths of the transitions when these fields are switched off. This is another current area of work.

7.2.2 Further experiments with the doubly-driven V system

As with the transient EIT experiments, the experiments on the doubly-driven V system could benefit from a dark SPOT configuration and switching off the trapping and magnetic fields of the MOT.

The cell of the new second-generation MOT has windows of high optical quality which gives us the opportunity of building an interferometer around the MOT. By placing the MOT in one of the arms of the interferometer as the perturbing medium, we would be able to measure the dispersion of the probe beam as it passes through the cloud of cold atoms in a similar way to [42,44]. This way we could measure the probe dispersion of an N system, such as the one studied in Chapter 6. In such a system, variations in the intensity and detuning of the second coupling field would induce phase shifts of the probe due to cross-phase modulation. Such an experiment would be of great interest in the area of ultra-slow and super-luminal light propagation [5,6,68-70], photon blockade [1-4] and more generally cross-phase modulation. This is the current area of work in this laboratory and some results are expected near the summer 2002.

Appendix A

Spectroscopic Data of Rubidium

Atomic number: $Z=37$

Relative atomic mass: 85.47

Relative abundance: $^{85}Rb=72\%$, $^{87}Rb=28\%$

Isotopic spin: $I=5/2$ (^{85}Rb), $I=3/2$ (^{87}Rb)

A.1 Relevant spectroscopic formulae

Some general spectroscopic formulae relevant to our experiments are presented here. These have been developed by Vaccaro [125] based on *The theory of coherent atomic excitation* by Shore [126], and have been used in this thesis to calculate Rabi frequencies, line strengths, saturation intensities, etc.

In the following equations we consider an atomic system with nuclear spin I, orbital-spin momentum J, total angular momentum F and magnetic quantum number M. The system has a decay rate $\Gamma_{J'J}$ from the state $|IJ'\rangle$ to $|IJ\rangle$, and this transition has a wavelength $\lambda_{J'J}$. ε_q is the polarisation component of the applied field, where $q=0,\pm1$ for π- and $\sigma^{\pm}$-polarised light. The coefficients (...,...|...) and { : : : } are the Clebsch-Gordan coefficients and the Wigner 6-j symbols, respectively, which are calculated in [126,127].

Partial decay rate from $IJ'F'$ to IJF:

$$\Gamma_{F'F} = (2J'+1)(2F+1)\begin{Bmatrix} J' & 1 & J \\ F & I & F' \end{Bmatrix}^2 \Gamma_{J'J}$$

Partial decay rate from $IJ'F'M'$ to $IJFM$:

$$\Gamma_{M'M} = (F\ M, 1\ q|F'\ M')^2 \Gamma_{F'F}$$

Saturation intensity from $IJ'F'$ to IJF:

$$I_{F'F}^{S} = \frac{2\pi^2 \hbar c \Gamma_{J'J}}{\lambda_{J'J}^3} \times \frac{1}{(2J'+1)(2F'+1)(2F+1)\begin{Bmatrix} J' & 1 & J \\ F & I & F' \end{Bmatrix}^2}$$

Rabi frequency from $IJ'F'$ to IJF:

$$\Omega_{F'F} = (-1)^{I+J+F+1} \Gamma_{J'J} \sqrt{\frac{I}{2I_{F'F}^{S}}}$$

Rabi frequency from $IJ'F'M'$ to $IJFM$:

$$\Omega_{M'M} = (-1)^{-M'-M+1} \Omega_{F'F} \sqrt{\frac{3}{2F+1}} \times \sum_q (-1)^q \varepsilon_q (F'\ M', 1\ -q|F\ M)$$

Electric dipole moment from IJ' to IJ:

$$\mu_{J'J} = \sqrt{\frac{3\epsilon_0 \hbar \lambda_{J'J}^3 \Gamma_{J'J}(2J'+1)}{8\pi^2}}$$

Electric dipole moment from $IJ'F'$ to IJF:

$$\mu_{F'F} = (-1)^{I+J+2F'+F-1} \sqrt{\frac{(2F'+1)(2F+1)}{3}} \times \begin{Bmatrix} J' & 1 & J \\ F & I & F' \end{Bmatrix} \mu_{J'J}$$

Electric dipole moment from *IJ'F'M'* to *IJFM*:

$$\mu_{M'M} = (-1)^{I+J+2F'+F-M'-M}\sqrt{(2F+1)}\begin{Bmatrix} J' & 1 & J \\ F & I & F' \end{Bmatrix} \times \mu_{J'J}\sum_q (-1)^q \varepsilon_q (F'\ M', 1\ -q | F\ M)$$

A.2 Hyperfine structure of rubidium

A.2.1 Hyperfine energy levels and data of the D_1 and D_2 lines

Here we show the hyperfine structure of the D_1 and D_2 lines of ^{87}Rb. Figure A.1 shows the hyperfine level diagram with the line strengths of each transition. Table A.1 shows the wavelength $\lambda_{JJ'}$ and decay rate $\Gamma_{JJ'}$ of each of the two lines and also the saturation intensities $I^S_{F'F}$, electric dipole moment $|\mu_{F'F}|$ and line strength $S_{FF'}$ of the different hyperfine transitions. These values have been calculated in [125].

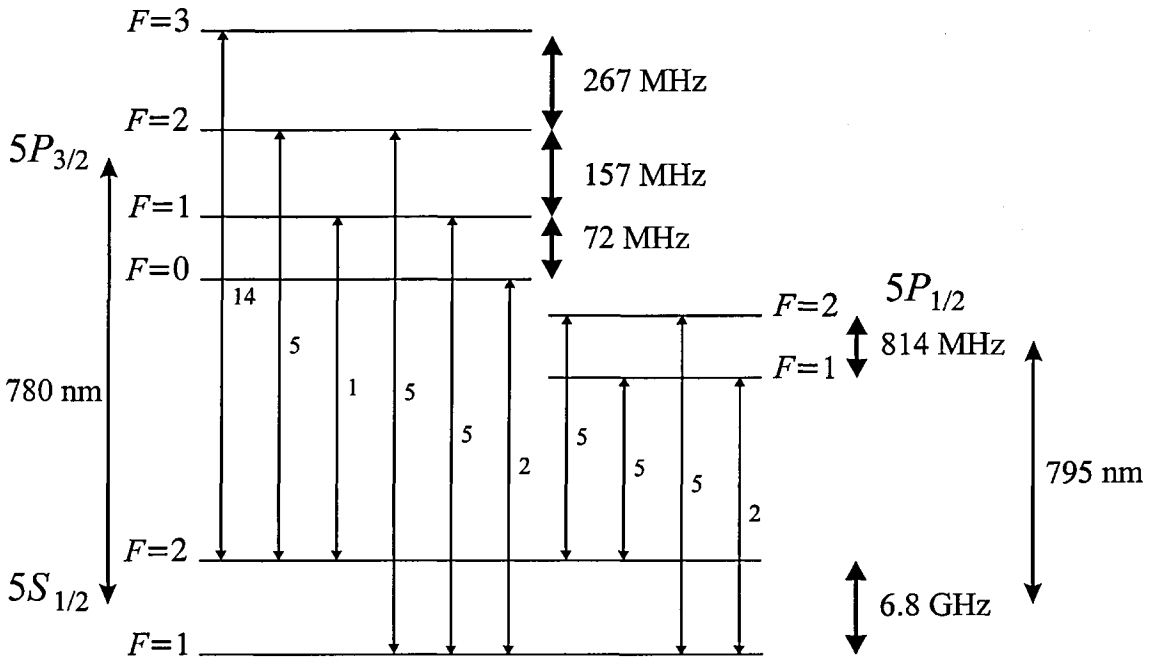

Figure A.1 - Hyperfine structure of the D_1 and D_2 lines of ^{87}Rb, showing the hyperfine line strengths.

Table A.1 - Hyperfine data of ^{87}Rb. From [125].

Line	$\lambda_{JJ'}$ nm	$\Gamma_{JJ'}$ MHz	F' upper	F ground	$I^S_{F'F}$ mW/cm^2	$\lvert\mu_{F'F}\rvert$ 10^{-29} C m	$S_{F'F}$ 10^{-58} C^2 m^2
D_1 $5S_{1/2}-5P_{1/2}$	794.76	$2\pi\times5.49$	2	2	1.71	2.26	5.11
			2	1	1.71	2.26	5.11
			1	2	1.71	2.26	5.11
			1	1	8.54	1.01	1.02
D_2 $5S_{1/2}-5P_{3/2}$	780.026	$2\pi\times5.68$	3	2	0.668	3.74	13.98
			2	2	1.87	2.23	4.97
			2	1	1.87	2.23	4.97
			1	2	9.35	0.999	0.998
			1	1	1.87	2.23	4.97
			0	1	4.68	1.41	1.99

A.2.2 Saturated absorption profiles

In this Section we present the saturated absorption spectra used to lock the lasers, as described in Section 4.2.3 (see Figure A.2 to Figure A.6). Table A.2 shows detuning Δ of each hyperfine level with respect to the line centre $\lambda_{JJ'}$. The data in this table has been obtained from [128].

Table A.2 - Hyperfine detuning Δ from the line centre $\lambda_{JJ'}$. From [128].

Line	$\lambda_{JJ'}$ nm	Species	F' upper	F ground	Δ MHz
D_1 $5S_{1/2}-5P_{1/2}$	794.76	87	1	2	−1881.547
			2	2	−1064.895
			1	1	4953.113
			2	1	5769.779
		85	2	3	−361.496
			3	3	0
			2	2	2674.230
			3	2	3035.726
D_2 $5S_{1/2}-5P_{3/2}$	780.026	87	1	2	−290.138
			2	2	−133.234
			3	2	134.216
			0	1	6472.296
			1	1	6544.543
			2	1	6701.464
		85	2	3	1075.851
			3	3	1139.267
			4	3	1260.874
			1	2	4082.219

			2	2	4111.608
			3	2	4175.055

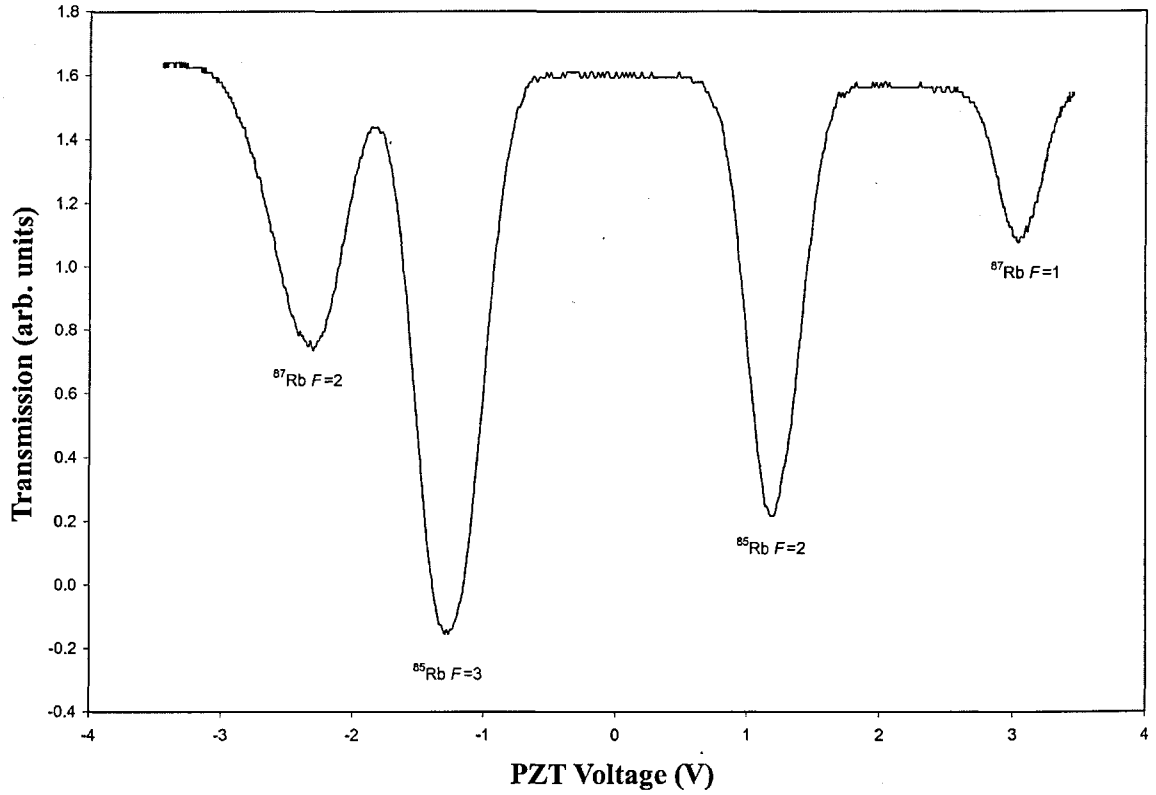

Figure A.2 – Doppler profile of the Rb D_2 line.

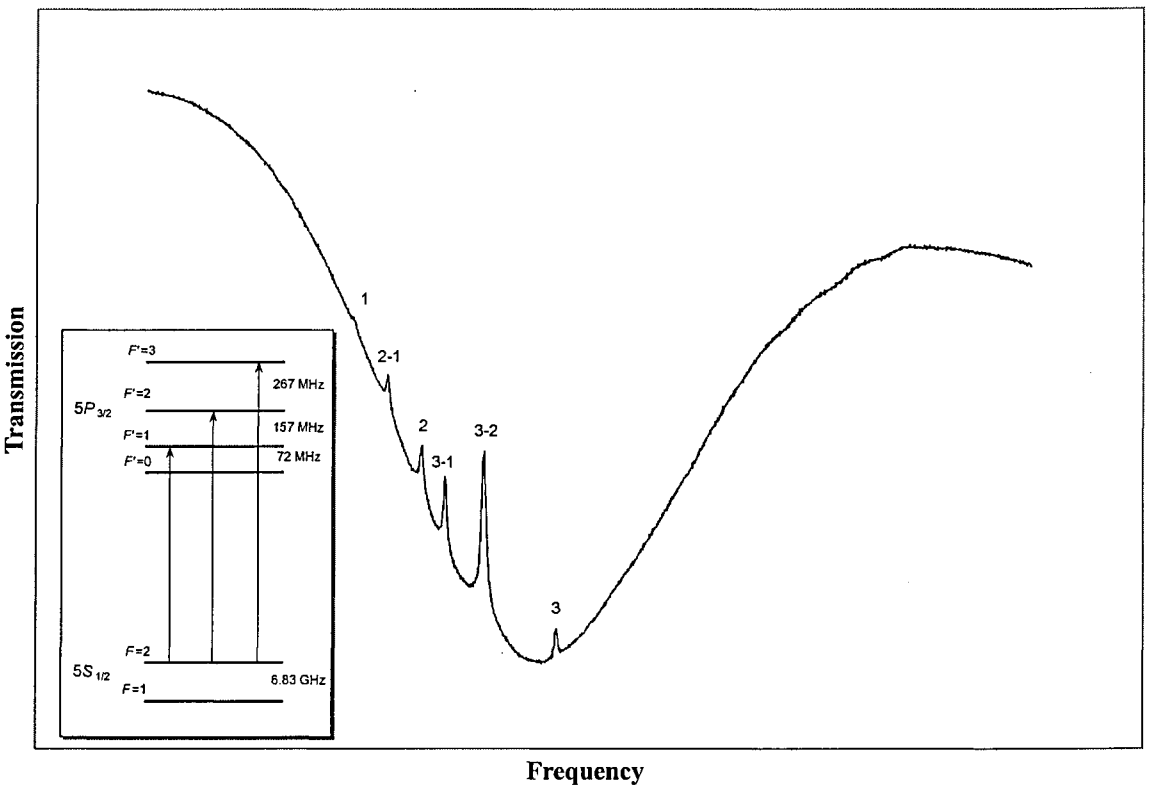

Figure A.3 - Saturated absorption profile of the ^{87}Rb F=2 manifold.

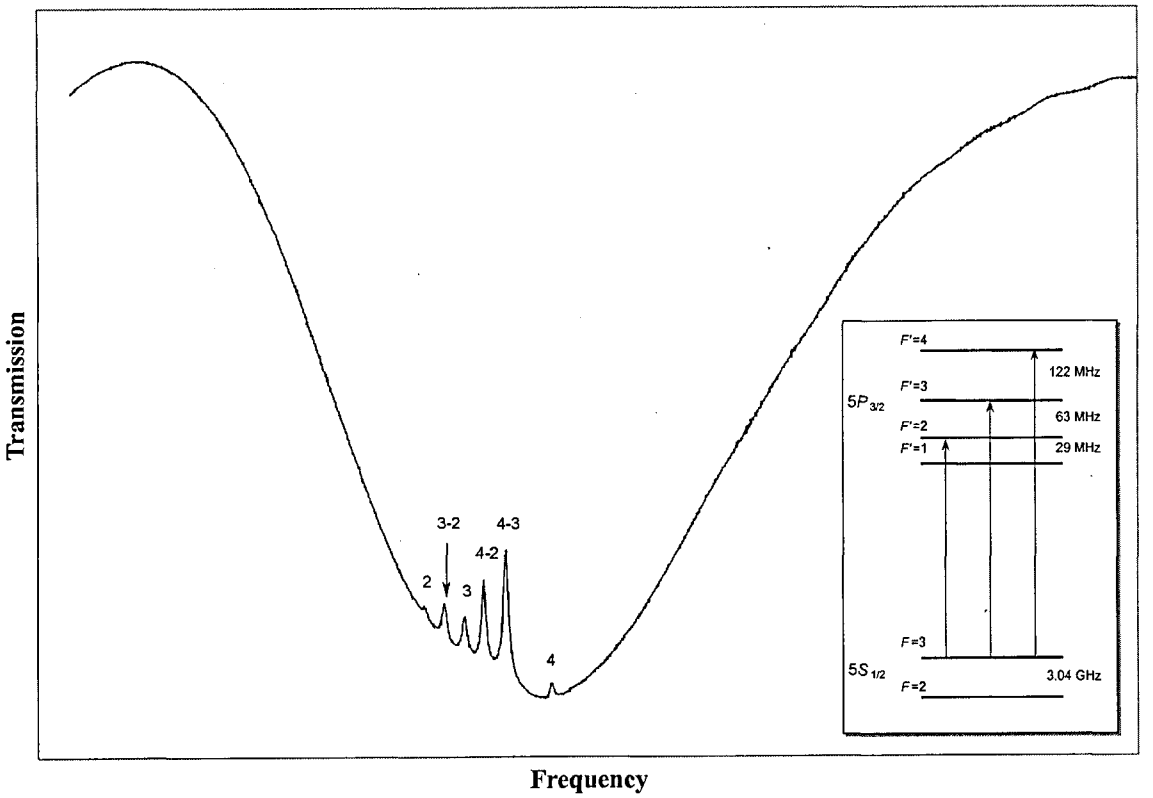

Figure A.4 - Saturated absorption profile of the ^{85}Rb F=3 manifold.

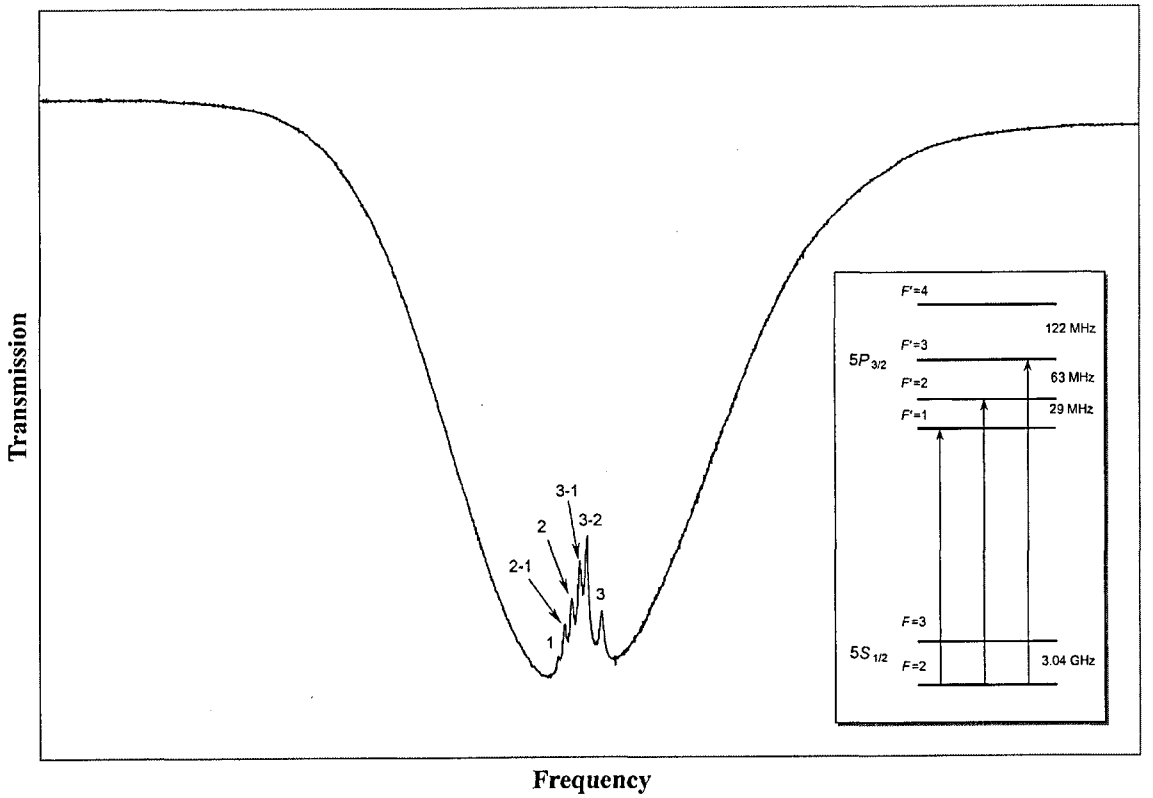

Figure A.5 - Saturated absorption profile of the ^{85}Rb F=2 manifold.

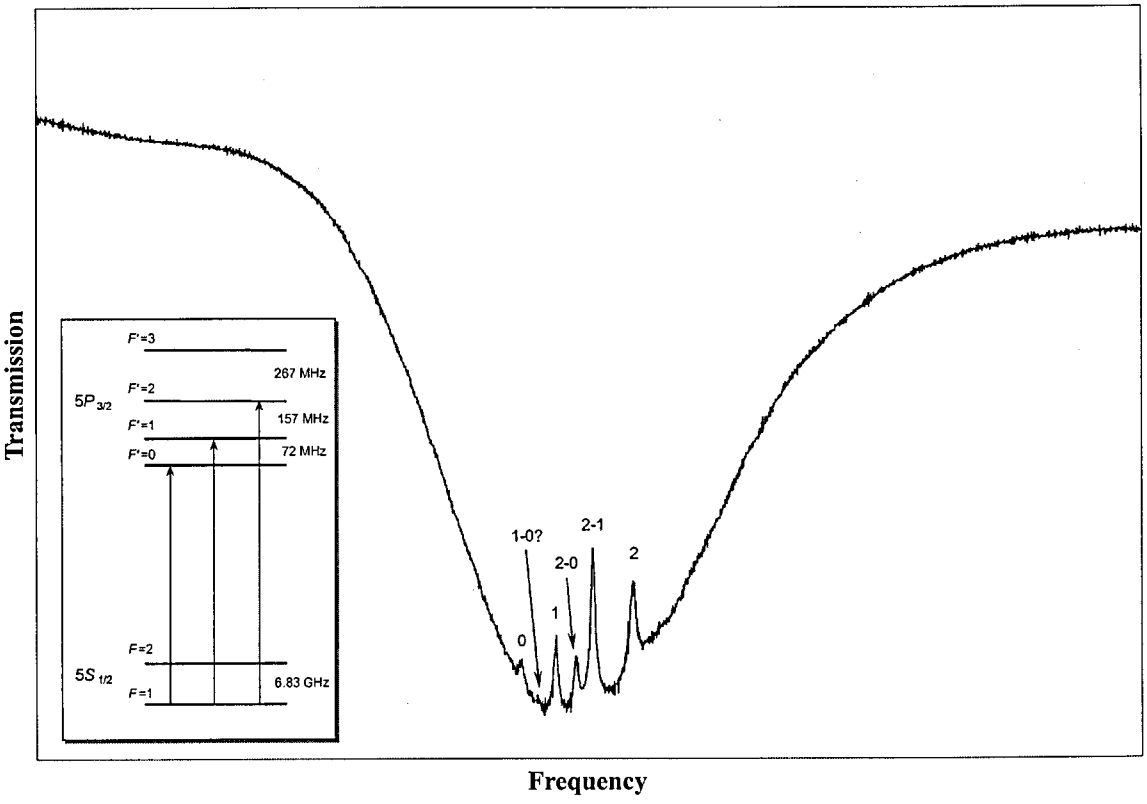

Figure A.6 - Saturated absorption profile of the ^{87}Rb F=1 manifold.

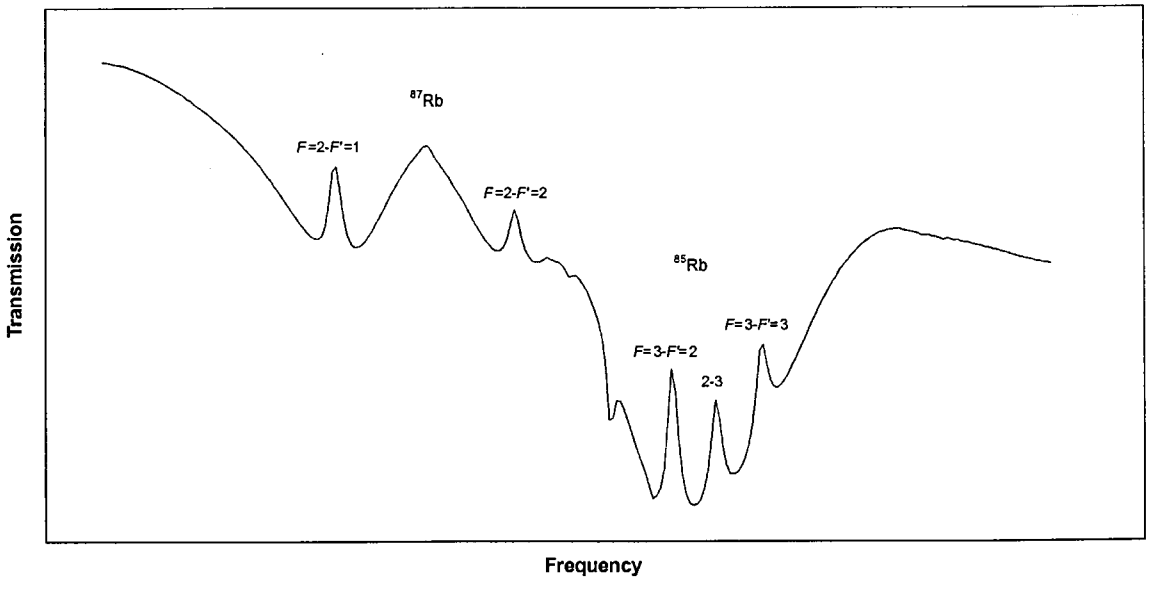

Figure A.7 - Saturated absorption profile of the D_1 line upper ground state manifold of ^{85}Rb and ^{87}Rb.

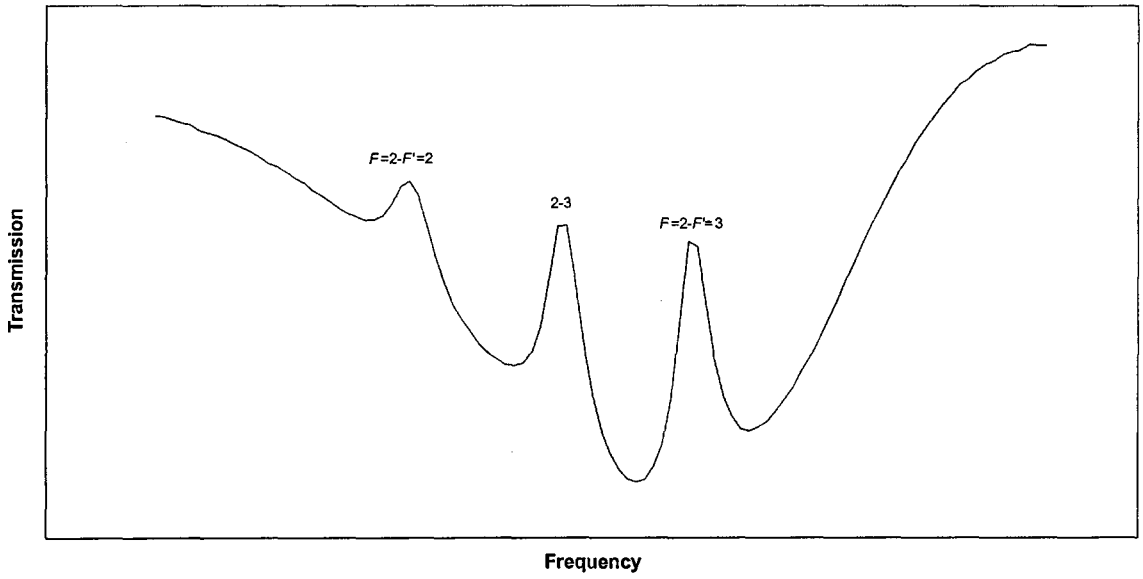

Figure A.8 - Saturated absorption profile of the D_1 line lower ground state manifold of ^{85}Rb.

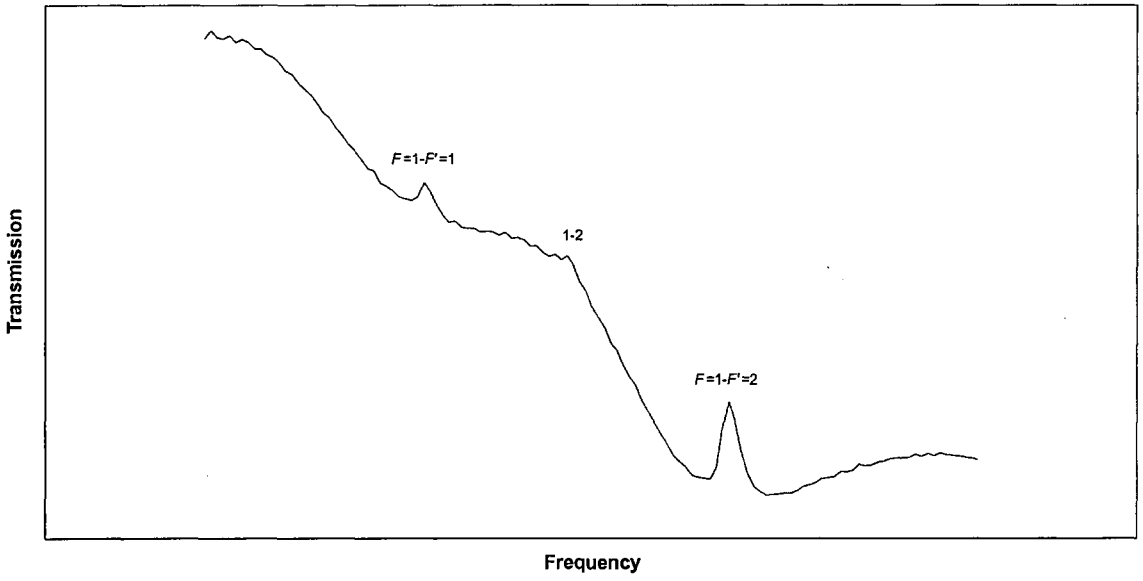

Figure A.9 - Saturated absorption profile of the D_1 line lower ground state manifold of ^{87}Rb.

Appendix B

Computer Control Programs

B.1 Tasks in the Experiments panel

B.1.1 The AHC&DET Scan task

Program file: `AHC&DETScan.daq`

Performs anti-Helmholtz coils and trapping beam detuning scans such as the one presented in Figure 4.9.

B.1.2 The Experiment Control task

Program file: `ExpControl.daq`

The main task that controls the anti-Helmholtz coils current, the AOMs frequency shift, the shutter and captures images of the cloud. It also calls the Image Analyser task to analyse any captured image.

B.1.3 The Image Analyser task

Program file: `ImAnalyser.daq`

Task called by the Experiment Control task to analyse the captured image. It is possible to extract image profiles, view a 3D representation of the image and save image. It can also be executed alone to analyse a previously saved image.

B.2 Tasks in the Test panel

B.2.1 The ATAO task

Program file: `ATAO.daq`

Test dialogue window for the AT-AO-10 board's analogue output channels.

B.2.2 The ATDIO task

Program file: `ATDIO.daq`

Test dialogue window for the AT-AO-10 board's digital I/O lines.

B.2.3 The LabAI task

Program file: `LabAI.daq`

Test dialogue window for the Lab-PC-1200AI board's analogue input channels.

B.2.4 The LabCount task

Program file: `LabCount.daq`

Test dialogue window for the Lab-PC-1200AI board's counter/timers.

B.2.5 The LabDIO task

Program file: `LabDIO.daq`

Test dialogue window for the Lab-PC-1200AI board's digital I/O lines.

B.2.6 The PCICount task

Program file: `PCICount.daq`

Test dialogue window for the PCI-6602 board's counter/timers.

B.2.7 The PCIDIO task

Program file: `PCIDIO`

Test dialogue window for the PCI-6602 board's digital I/O lines.

B.2.8 The Thurlby task

Program file: `Thurlby.daq`

Test dialogue window for a Thurlby power supply unit controlled via GPIB with the GPIB-PCII board.

Appendix C

Further Investigations of the "Fast" Oscillations

The oscillations in $\mathrm{Im}[\rho_{ac}(t)]$ at the angular frequency Ω_C noted in Section 5.2 are unusual in that the Rabi frequency usually associated with the cycling of population is approximately $\Omega_C/2$. This behaviour can be understood by means of the 3-D vector model [66,67] described in Section 2.1.2, where the evolution of the system, for zero decay rates and detunings, is described by

$$\frac{d\mathbf{v}}{dt} = \mathbf{\Omega} \times \mathbf{v}, \tag{C.1}$$

where $\mathbf{v}=(v_a, v_b, v_c)$ is a real vector representing the quantum amplitudes of states $|a\rangle$, $|b\rangle$ and $|c\rangle$, and $\mathbf{\Omega}=(\frac{1}{2}\Omega_C, -\frac{1}{2}\Omega_p, 0)$ is called the Rabi vector (see Figure 2.7). In this model, the state vector $\mathbf{v}$ precesses on a cone around the Rabi vector $\mathbf{\Omega}$, according to (C.1). The probe absorption coefficient is proportional to $-v_a v_c$ in this picture. Thus, as

v precesses around Ω, the product $-v_a v_c$ takes positive and negative values, which describes periods of absorption and gain, respectively.

We note from (5.9)&(5.10) that, in general, $\mathrm{Im}(\rho_{ac})$ has frequency components at both the $\Omega_C/2$ and Ω_C frequencies. However, there are two important cases where $\mathrm{Im}(\rho_{ac})$ oscillates at either $\Omega_C/2$ or Ω_C.

C.1 "Slow" oscillations

The first case is when $\rho_{aa}^0 = 1$. Substituting this into (5.10) gives $\mathrm{Im}(\rho_{ac})$ oscillating at a frequency of $\Omega_C/2$. In this case the initial state vector lies along the $\pm a$ axis, that is, $\mathbf{v}(0)=(\pm 1, 0, 0)^{\mathrm{T}}$. In time, the state vector v traces out an acute cone (of half angle θ) centred on $\pm\Omega$ and revolves at frequency Ω. The full solution of (C.1) is given by

$$\mathbf{v}(t) = \pm \begin{pmatrix} 1+\sin^2\theta[\cos(\Omega t)-1] \\ -\cos\theta\sin\theta[\cos(\Omega t)-1] \\ -\sin\theta\sin(\Omega t) \end{pmatrix}. \qquad \text{(C.2)}$$

Keeping terms up to first order in Ω_p/Ω_C gives $\mathrm{Im}[\rho_{ac}(t)] \approx -(\Omega_p/\Omega_C)\sin(\Omega t) \approx -(\Omega_p/\Omega_C)\sin(\Omega_C t/2)$ as found in (5.10).

C.2 "Fast" oscillations

The second case is when $\rho_{aa}^0 = \rho_{bb}^0 = 1/2$. In this case (5.10) shows that $\mathrm{Im}(\rho_{ac})$ oscillates only at the double frequency, i.e. Ω_C. Equation (5.10) was derived for zero ground state coherence, i.e. $\rho_{ab}^0 = 0$. This means that in the gas sample, half the atoms are in state $|a\rangle$ and the remainder are in $|b\rangle$. We model this by taking the average of the

values of $\mathrm{Im}(\rho_{ac})$ for both collections of atoms. For the atoms beginning in the $|b\rangle$ state, the vector is initially aligned along the $\pm b$ axis, $\mathbf{v}(0)=(0, \pm 1, 0)^{T}$, and traces out a cone of half angle $\pi/2\pm\theta$. The solution of (C.1) for this case is given by

$$\mathbf{v}(t)=\pm\begin{pmatrix}\cos\theta\sin\theta[\cos(\Omega t)-1]\\ 1+\cos^2\theta[\cos(\Omega t)-1]\\ -\cos\theta\sin(\Omega t)\end{pmatrix}. \tag{C.3}$$

Keeping terms up to first order in Ω_p/Ω_C gives $\mathrm{Im}[\rho_{ac}(t)]\approx -(\Omega_p/\Omega_C)[\frac{1}{2}\sin(2\Omega t)-\sin(\Omega t)]$. Taking the average of this value and the value in (C.2) yields $\mathrm{Im}[\overline{\rho_{ac}(t)}]\approx -\frac{1}{4}(\Omega_p/\Omega_C)\sin(2\Omega t)\approx -\frac{1}{4}(\Omega_p/\Omega_C)\sin(\Omega_C t)$ as found in (5.10).

In summary, we have traced the origin of the oscillations at twice the Rabi frequency Ω_C to the fact that for a pure state, ρ_{ac} is the product of the amplitude of finding the atom in state $|a\rangle$ and the complex conjugate of the amplitude in state $|c\rangle$. In the absence of decay, both amplitudes have terms that oscillate at the frequency $\Omega_C/2$, and so their product gives rise to a term oscillating at twice this frequency. So even though the populations oscillate at the Rabi frequency $\Omega_C/2$, the absorption and emission of light has a term that occurs at twice this frequency.

Bibliography

[1] A. Imamoğlu, H. Schmidt, G. Woods, and M. Deutsch, Phys. Rev. Lett. **79**, 1467 (1997).

[2] P. Grangier, D. F. Walls, and K. M. Gheri, Phys. Rev. Lett. **81**, 2833 (1998); A. Imamoğlu, H. Schmidt, G. Woods, and M. Deutsch, Phys. Rev. Lett. **81**, 2836 (1998); K. M. Gheri, W. Alge, and P. Grangier, Phys. Rev. A **60**, R2673 (1999).

[3] S. Rebić, S. M. Tan, A. S. Parkins, and D. F. Walls, J. Opt. B: Quantum Semiclass. Opt. **1**, 490 (1999); M. J. Werner and A. Imamoğlu, Phys. Rev. A **61**, 011801(R) (1999).

[4] A. D. Greentree, J. A. Vaccaro, S. R. de Echaniz, A. V. Durrant, and J. P. Marangos, J. Opt. B: Quantum Semiclass. Opt **2**, 252 (2000).

[5] L. V. Hau, S. E. Harris, Z. Dutton, and C. H. Behroozi, Nature **397**, 594 (1999).

[6] M. M. Kash, V. A. Sautenkov, A. S. Zibrov, L. Hollberg, G. R. Welch, M. D. Lukin, Y. Rostovtsev, E. S. Fry, and M. O. Scully, Phys. Rev. Lett. **82**, 5229 (1999); D. Budker, D. F. Kimball, S. M. Rochester, and V. V. Yashchuk, *ibid.* **83**, 1767 (1999).

[7] H. Chen, A. V. Durrant, J. P. Marangos, and J. A. Vaccaro, Phys. Rev. A **58**, 1545 (1998).

[8] H. Chen, Ph.D. thesis, The Open University, 1998.

[9] S. E. Harris and Y. Yamamoto, Phys. Rev. Lett. **81**, 3611 (1998).

[10] B. S. Ham and P. R. Hemmer, Phys. Rev. Lett. **84**, 4080 (2000); H. Schmidt and R. J. Ram, Appl. Phys. Lett. **76**, 3173 (2000); B. S. Ham, ETRI J. **23**, 106 (2001); B. S. Ham, Appl. Phys. Lett. **78**, 3382 (2001); J. Clarke, H. Chen, W. A. van Wijngaarden, Appl. Optics **40**, 2047 (2001).

[11] P. R. Berman and R. Salomaa, Phys. Rev. A **25**, 2667 (1982).

[12] N. Lu and P. R. Berman, Phys. Rev. A **36**, 3845 (1987).

[13] N. Lu, P. R. Berman, A. G. Yodh, Y. S. Bai, and T.W. Mossberg, Phys. Rev. A **33**, 3956 (1986).

[14] S. E. Harris and Z. F. Luo, Phys. Rev. A **52**, R928 (1995).

[15] Y. Li and M. Xiao, Opt. Lett. **20**, 1489 (1995).

[16] Y. Zhu, Phys. Rev. A **53**, 2742 (1996).

[17] Y. Zhu, Phys. Rev. A **55**, 4568 (1997).

[18] Y. S. Bai, A. G. Yodh, and T. W. Mossberg, Phys. Rev. Lett. **55**, 1277 (1985).

[19] Y. S. Bai, T. W. Mossberg, N. Lu, and P. R. Berman, Phys. Rev. Lett. **57**, 1692 (1986).

[20] H. W. H. Lee and J. E. Wessel, Phys. Rev. Lett. **59**, 1416 (1987).

[21] E. S. Fry, X. Li, D. Nikonov, G. G. Padmabandu, M. O. Scully, A. V. Smith, F. K. Tittel, C. Wang, S. R. Wilkinson, and S-Y. Zhu, Phys. Rev. Lett. **70**, 3235 (1993).

[22] C. Wei, A. D. Greentree, N. B. Manson, and J. P. D. Martin, J. Lumin. **66 & 67**, 61 (1996); C. Wei, S. A. Holmstrom, A. D. Greentree, and N. B. Manson, J. Opt. B: Quantum Semiclass. Opt. **1**, 289 (1999).

[23] A. D. Greentree, C. Wei, S. A. Holmstrom, J. P. D. Martin, N. B. Manson, K. R. Catchpole, and C. Savage, J. Opt. B: Quantum Semiclassical Opt. **1**, 240 (1999); A. D. Greentree, C. Wei, and N. B. Manson, Phys. Rev. A **59**, 1 (1999).

[24] S. N. Sandhya and K. K. Sharma, Phys. Rev. A **55**, 2155 (1997).

[25] S. M. Sadeghi, J. Meyer, and H. Rastegar, Phys. Rev. A **56**, 3097 (1997).

[26] C. Wei, D. Suter, A. S. M. Windsor, and N. B. Manson, Phys. Rev. A **58**, 2310 (1998).

[27] M. D. Lukin, S. F. Yelin, M. Fleischhauer, and M. O. Scully, Phys. Rev. A **60**, 3225 (1999).

[28] M. D. Lukin, P. R. Hemmer, M. Loffler, and M. O. Scully, Phys. Rev. Lett. **81**, 2675 (1998); M. D. Lukin, A. B. Matsko, M. Fleischhauer, and M. O. Scully, *ibid.* **82**, 1847 (1999); A. F. Huss, N. Peer, R. Lammegger, E. A. Korunsky, and L. Windholz, Phys. Rev. A **63**, 013802 (2000).

[29] S. R. de Echaniz, A. D. Greentree, A. V. Durrant, D. M. Segal, J. P. Marangos, and J. A. Vaccaro, Phys. Rev. A **64**, 013812 (2001).

[30] M. Yan, E. G. Rickey, and Y. Zhu, Opt. Lett. **26**, 548 (2001).

[31] M. Yan, E. G. Rickey, and Y. Zhu, Phys. Rev. A **64**, 013412 (2001).

[32] E. Arimondo and G. Orriols, Nuovo Cim. Lett. **17**, 333 (1976).

[33] G. Alzetta, A. Gozzini, L. Moi, and G. Orriols, Nuovo Cim. B **36**, 5 (1976).

[34] E. Arimondo, Prog. Optics **35**, 257 (1996).

[35] H. Y. Ling, Y-Q. Li, and M. Xiao, Phys. Rev. A **53**, 1014 (1996).

[36] O. Kocharovkaya, Phys. Rep. **219**, 175 (1992); M. O. Scully, Phys. Rep. **219**, 191(1992); S. E. Harris, Phys. Today **50**(7), 36 (1997); J. P. Marangos, J. Mod. Opt. **45**, 471 (1998).

[37] S. E. Harris, J. E. Field, and A. Imamoğlu, Phys. Rev. Lett. **64**, 1107 (1990).

[38] K. J. Boller, A. Imamoğlu, and S. E. Harris, Phys. Rev. Lett. **66**, 2593 (1991).

[39] D. J. Fulton, S. Shepherd, R. R. Moseley, B. D. Sinclair, and M. H. Dunn, Phys. Rev. A **52**, 2302 (1995).

[40] J. Gea-Banacloche, Y. Li, S. Jin, and M. Xiao, Phys. Rev. A **51**, 576 (1995); R. R. Moseley, S. Shepherd, D. J. Fulton, B. D. Sinclair, and M. H. Dunn, Phys. Rev. Lett. **74**, 670 (1995); R. R. Moseley, S. Shepherd, D. J. Fulton, B. D. Sinclair, and M. H. Dunn, Opt. Comm. **199**, 61 (1995).

[41] Y. Li and M. Xiao, Phys. Rev. A **51**, R2703 (1995).

[42] M. Xiao, Y. Li, S. Jin, and J. Gea-Banacloche, Phys. Rev. Lett. **74**, 666 (1995).

[43] G. G. Padmabandu, G. R. Welch, I. N. Shubin, E. S. Fry, D. E. Nikonov, M. D. Lukin, and M. O. Scully, Phys. Rev. Lett. **76**, 2053 (1996).

[44] T. van der Veldt, J. F. Roch, P. Grelu, and P. Grangier, Opt. Comm. **137**, 420 (1997).

[45] S. A. Hopkins, E. Usadi, H. Chen, and A. V. Durrant, Opt. Comm. **138**, 185 (1997); A. V. Durrant, H. Chen, S. A. Hopkins, and J. A. Vaccaro, Opt. Comm. **151**, 136 (1998).

[46] Z. Dutton, M. Budde, C. Slowe, and .L. V. Hau, Science **293**(5530), 663 (2001); O. E. Mustecaplioglu and L. You, Opt. Comm. **193**, 301 (2001).

[47] J. W. R. Tabosa, G. Chen, Z. Hu, R. B. Lee, and H. J. Kimble, Phys. Rev. Lett. **66**, 3245 (1991).

[48] Y. Li and M. Xiao, Opt. Lett. **21**, 1064 (1996); J. C. Petch, C. H. Keitel, P. L. Knight, and J. P. Marangos, Phys. Rev. A **53**,543 (1996).

[49] Y. F. Zhu and J. Lin, Phys. Rev. A **53**, 1767 (1996).

[50] A. Nottlemann, C. Peters, and W. Lange, Phys. Rev. Lett. **70**, 1783 (1993).

[51] S. R. de Echaniz, A. D. Greentree, A. V. Durrant, D. M. Segal, J. P. Marangos, and J. A. Vaccaro, Phys. Rev. A **64**, 055801 (2001).

[52] A. D. Greentree, T. B. Smith, S. R. de Echaniz, A. V. Durrant, D. M. Segal, J. P. Marangos, J. A. Vaccaro, Phys. Rev. A **65**, 053802 (2002).

[53] C. Liu, Z. Dutton, C. H. Behroozi, and L. V. Hau, Nature **409**, 490 (2001).

[54] D. F. Phillips, A. Fleischhauer, A. Mair, and R. L. Walsworth, Phys. Rev. Lett. **86**, 783 (2001).

[55] G. Morigi, J. Eschner, and C. H. Keitel, Phys. Rev. Lett. **85**, 4458 (2000).

[56] C. F. Roos, D. Leibfried, A. Mundt, F. Schmidt-Kaler, J. Eschner, and R. Blatt, Phys. Rev. Lett. **85**, 5547 (2000); F. Schmidt-Kaler, J. Eschner, G. Morigi, C. F. Roos, D. Leibfried, A. Mundt, and R. Blatt, Appl. Phys. B **73**, 807 (2001).

[57] C. F. Roos, T. Zeiger, H. Rohde, H. C. Nägerl, J. Eschner, D. Leibfried, F. Schmidt-Kaler, and R. Blatt, Phys. Rev. Lett. **83**, 4713 (1999).

[58] H. R. Gray, R. M. Whitley, and C. R. Stroud Jr., Opt. Lett. **3**, 218 (1978).

[59] C. Cohen-Tannoudji, J. Dupont-Roc, and G. Grynberg, *Atom-Photon Interactions: Basic Processes and Applications* (John Wiley & Sons, New York, 1992), Chap. VI.

[60] S. H. Autler and C. H. Townes, Phys. Rev. **100**, 703 (1955).

[61] Y. Li and M. Xiao, Phys. Rev. A **51**, 4959 (1995).

[62] C. Cohen-Tannoudji, J. Dupont-Roc, and G. Grynberg, *Atom-Photon Interactions: Basic Processes and Applications* (John Wiley & Sons, New York, 1992), Chap. IV.

[63] F. A. M. de Oliveira, B. J. Dalton, and P. L. Knight, J. Opt. Soc. Am. B **4**, 1558 (1987).

[64] R. W. Boyd, *Nonlinear Optics* (Academic Press, London, 1992), Chap. 3.

[65] J. Mompart, C. Peters, and R. Corbalán, J. Opt. B: Quantum Semiclass. Opt. **10**, 355 (1998).

[66] A. Kasapi, J. Opt. Soc. Am. B **13**, 1347 (1996).

[67] J. A. Vaccaro, A. V. Durrant, S. A. Hopkins, H. Chen, and K. E. Hill, J. Mod. Opt. **45**, 315 (1998).

[68] A. M. Steinberg and R. Y. Chiao, Phys. Rev. A **49**, 2071 (1994); M. W. Mitchell and R. Y. Chiao, Am. J. Phys. **66**, 14 (1998).

[69] L. J. Wang, A. Kuzmich, and A. Dogariu, Nature **406**, 277 (2000).

[70] A. Dogariu, A. Kuzmich, and L. J. Wang, Phys. Rev. A **63**, 053806 (2001).

[71] C. J. Hood, M. S. Chapman, T. W. Lynn, and H. J. Kimble, Phys. Rev. Lett. **80**, 4157 (1998).

[72] S. Stenholm, Rev. Mod. Phys. **58**, 699 (1986).

[73] C. Cohen-Tannoudji, Phys. Rep. **219**, 153 (1992).

[74] C. S. Adams and E. Riis, Prog. Quant. Electr. **21**, 1 (1997).

[75] W. D. Phillips and H. Metcalf, Phys. Rev. Lett. **48**, 596 (1982).

[76] S. Chu, L. Hollberg, J. E. Bjorkholm, A. Cable, and A. Ashkin, Phys. Rev. Lett. **55**, 48 (1985).

[77] E. L. Raab, M. Prentiss, A. Cable, S. Chu, and D. E. Pritchard, Phys. Rev. Lett. **59**, 2631 (1987).

[78] P. D. Lett, R. N. Watts, C. I. Westbrook, W. D. Phillips, P. L. Gould, and H. J. Metcalf, Phys. Rev. Lett. **61**, 169 (1988).

[79] J. Dalibard and C. N. Cohen-Tannoudji, J. Opt. Soc. Am. B **6**, 2023 (1989).

[80] P. J. Ungar, D. S. Weiss, E. Riis, and S. Chu, J. Opt. Soc. Am. B **6**, 2058 (1989).

[81] A. Aspect, E. Arimondo, R. Kasier, N. Vansteenkiste, and C. N. Cohen-Tannoudji, Phys. Rev. Lett. **61**, 826 (1988); M. Kasevich and S. Chu, *ibid.* **69**, 1741 (1992).

[82] J. Lawall, S. Kulin, F. Bardou, B. Saubamea, N. Bigelow, M. Leduc, and C. Cohen-Tannoudji, Phys. Rev. Lett. **75**, 4194 (1995); H. J. Lee, C. S. Adams, M. Kasevich, and S. Chu, *ibid.* **76**, 2658 (1996).

[83] S. Chu, Rev. Mod. Phys **70**, 685 (1998); C. N. Cohen-Tannoudji, *ibid.*, 707 (1998); W. D. Phillips, *ibid.*, 721 (1998).

[84] C. Monroe, H. Robinson, and C. Wieman, Opt. Lett. **16**, 50 (1991).

[85] M. H. Anderson, J. R. Ensher, M. R. Matthews, C. E. Wieman, and E. A. Cornell, Science **269**, 198 (1995).

[86] T. W. Hänsch and A. L. Schawlow, Opt. Comm. **13**, 68 (1974).

[87] S. A. Hopkins, Ph.D. thesis, The Open University, 1995.

[88] J. P. Gordon and A. Ashkin, Phys. Rev. A **21**, 1606 (1980); R. J. Cook, Phys. Rev. Lett. **44**, 976 (1980).

[89] C. N. Cohen-Tannoudji and W. D. Phillips, Phys. Today **43** (10), 33 (1990).

[90] Y. Castin and J. Dalibard, Europhys. Lett. **14**, 761 (1991); K. Berg-Sorensen, Y. Castin, K. Molmer, and J. Dalibard, Europhys. Lett. **22**, 663 (1993); H. Wallis, Phys. Rep. **255**, 203 (1995).

[91] A. Ashkin, Phys. Rev. Lett. **24**, 156 (1970); *ibid.* **25**, 1321 (1970); S. Chu, J. E. Bjorkholm, A. Ashkin, and A. Cable, *ibid.* **57**, 314 (1986).

[92] A. L. Migdall, J. V. Prodan, W. D. Phillips, T. H. Bergeman, and H. J. Metcalf, Phys. Rev. Lett. **54**, 2596 (1985); T. Bergeman, G. Erez, and H. J. Metcalf, Phys. Rev. A **35**, 1535 (1987).

[93] D. E. Pritchard, E. L. Raab, V. Bagnato, C. E. Wieman, and R. N. Watts, Phys. Rev. Lett. **57**, 310 (1986).

[94] A. Ashkin and J. P. Gordon, Opt. Lett. **8**, 511 (1983).

[95] A. M. Steane, M. Chowdhury, and C. J. Foot, J. Opt. Soc. Am. B **9**, 2142 (1992).

[96] C. Monroe, W. Swann, H. Robinson, and C. Wieman, Phys. Rev. Lett. **65**, 1571 (1990).

[97] D. Sesko, T. Walker, C. Monroe, A. Gallagher, and C. Wieman, Phys. Rev. Lett. **63**, 961 (1989); A. Gallagher and D. E. Pritchard, *ibid.* **63**, 957 (1989); P. S. Julienne, R. Heather, and J. Vigue, in *AIP Conference Proceedings 233: Atomic Physics 12, Ann Arbor, 1990*, edited by J. Zorn and R. Lewis (Am. Inst. Phys., New York, 1991), p. 116; M. Prentiss, A. Cable, J. E. Bjorkholm, S. Chu, E. L. Raab, and D. Pritchard, Opt. Lett. **13**, 452 (1988).

[98] S. A. Hopkins and A. V. Durrant, Phys. Rev. A **56**, 4012 (1997).

[99] A. M. Steane, and C. J. Foot, Europhys. Lett. **14**, 231 (1991).

[100] M. Walhout, J. Dalibard, S. L. Rolston, and W. D. Phillips, J. Opt. Soc. Am. B **9**, 1997 (1992); J. Werner, H. Wallis, and W. Ertmer, Opt. Comm. **94**, 525 (1992).

[101] D. W. Sesko, T. G. Walker, and C. E. Wieman, J. Opt. Soc. Am. B **8**, 946 (1991).

[102] A. Steane, Ph.D. thesis, Oxford University, 1991; E. Usadi, The Open University Physics Department Report PD 9406, 1994.

[103] A. Corney, *Atomic and Laser Spectroscopy* (Clarendon Press, Oxford, 1977), Chap. 13; N. Bloembergen, V. P. Chebotayev, J. L. Hall, S. Haroche, P. Jacquinot, V. S. Letokhov, M. D. Levenson, J. A. Magyar, and K. Shimoda, in *High-Resolution Laser Spectroscopy*, edited by K. Shimoda (Springer-Verlag, Berlin, 1976), Chap. 4.

[104] K. B. McAdam, A. Steinbach, and C. Weiman, Am. J. Phys. **60**, 1098 (1992).

[105] A. S. Arnold, J. S. Wilson, and M. G. Boshier, Rev. Sci. Instrum. **69**, 1236 (1998).

[106] W. Ketterle, K. B. Davis, M. A. Joffe, A. Martin, and D. E. Pritchard, Phys. Rev. Lett. **70**, 2253 (1993).

[107] M. J. Snadden, A. S. Bell, R. B. M. Clarke, and E. Riis, J. Opt. Soc. Am. B **14**, 544 (1997).

[108] C. G. Townsend, N. H. Edwards, K. P. Zetie, C. J. Cooper, J. Rink, and C. J. Foot, Phys. Rev. A **53**, 1702 (1996).

[109] J. H. McLeod, J. Opt. Soc. Am. **44**, 592 (1954); E. J. Sween, *ibid.* **47**, 344 (1957); J. H. McLeod, *ibid.* **50**, 166 (1960); I. Manek, Y. B. Ovchinnikov, and R. Grimm, Opt. Comm. **147**, 67 (1998); S. Kulin, S. Aubin, S. Christe, B. Peker,

S. L. Rolston, and L. A. Orozco, J. Opt. B: Quantum Semiclass. Opt. **3**, 353, (2001).

[110] D. Grison, B. Lounis, C. Salomon, J. Y. Courtois, and G. Grynberg, Europhys. Lett. **15**, 149 (1991); L. Hilico, C. Fabre, and E. Giacobino, *ibid.* **18**, 685 (1992); B. Gao, Phys. Rev. A **49**, 3391 (1994); J. Y. Courtois, Ann. Phys.-Paris **21**, 1 (1996); **21**, 93 (1996).

[111] C. Wieman, G. Flowers, and S. Gilbert, Am. J. Phys. **63**, 317 (1994).

[112] J. Fortagh, A. Grossman, T. W. Hänsch, and C. Zimmermann, J. Appl. Phys. **84**, 6499 (1998); U. D. Rapol, A. Wasan, and V. Natarajan, Phys. Rev. A **64**, 023402 (2001).

[113] D. J. Santeler, J. Vac. Sci. Tech. A, **10**, 1879 (1992).

[114] A. Schenzle and R. G. Brewer, Phys. Rev. A **14**, 1756 (1976).

[115] O. Kocharovskaya, Y. Rostovtsev, and M. O. Scully, Phys. Rev. Lett. **86**, 628 (2001); D. F. Phillips, A. Fleischhauer, A. Mair, R. L. Walsworth, and M. D. Lukin, *ibid.* **86**, 783 (2001).

[116] M. Yan, E. G. Rickey, and Y. Zhu, Phys. Rev. A **64**, 041801 (2001).

[117] N. V. Vitanov, T. Halfmann, B. W. Shore, and K. Bergmann, Annu. Rev. Phys. Chem. **52**, 763 (2001).

[118] O. D. Mücke, T. Tritschler, M. Wegener, U. Morgner, and F. X. Kärtner, Phys. Rev. Lett. **87**, 057401 (2001).

[119] S. A. Holmstrom, A. S. M. Windsor, C. Wei, J. P. D. Martin, and N. B. Manson, J. Lumin. **76 & 77**, 38 (1998).

[120] P. M. Morse and H. Feshbach, *Methods of theoretical physics*, (McGraw-Hill, New York 1953).

[121] A. M. Akulshin, S. Barreiro, and A. Lezama, Phys. Rev. A **57**, 2996 (1998); A. Lezama, S. Barreiro, and A. M. Akulshin, *ibid.* **59**, 4732 (1999); A. V. Taichenachev, A. M. Tumaikin, and V. I. Yudin, *ibid.* **61**, 011802 (2000); V. M. Entin, I. I. Ryabtsev, A. E. Boguslavskii, and I. M. Beterov, JETP Lett. **71**, 175 (2000).

[122] D. McGloin, M. H. Dunn, and D. J. Fulton, Phys. Rev. A, **62**, 053802 (2000).

[123] A. Schmidt and A. Imamoğlu, Opt. Lett. **21**, 1936 (1996).

[124] B. W. Shore, *The theory of coherent atomic excitation*, (John Wiley and Sons, New York, 1990), Vol. 2: Multilevel atoms and incoherence.

[125] J. A. Vaccaro, *Line strenghts, decay rates and Rabi frequencies for hyperfine systems* (private communication, 2001).

[126] B. W. Shore, *The Theory of Coherent Atomic Excitation* (John Wiley & Sons, New York, 1990).

[127] P. Stevenson, http://www.ph.surrey.ac.uk/~phs3ps/cleb.html.

[128] G. P. Barwood, P. Gill, and W. R. C. Rowley, Appl. Phys. B **53**, 142 (1991).